UNIVERSITY OF NOTTINGHAM

DOCTORAL THESIS

Synthesis and Characterisation of Multi-Substituted Hydroxyapatites

Author:
Ben MCCARTHY

Supervisors:
Prof. David GRANT
Dr. Philip JACKSON
Dr. Colin SCOTCHFORD

A thesis submitted in fulfillment of the requirements for the degree of Doctor of Philosophy

in the

Advanced Materials Research Group
Mechanical, Materials and Manufacturing Engineering

September 19, 2017

Declaration of Authorship

I, Ben McCarthy, declare that this thesis titled, "Synthesis and Characterisation of Multi-Substituted Hydroxyapatites" and the work presented in it are my own. I confirm that:

- This work was done wholly or mainly while in candidature for a research degree at this University.
- Where any part of this thesis has previously been submitted for a degree or any other qualification at this University or any other institution, this has been clearly stated.
- Where I have consulted the published work of others, this is always clearly attributed.
- Where I have quoted from the work of others, the source is always given. With the exception of such quotations, this thesis is entirely my own work.
- I have acknowledged all main sources of help.
- Where the thesis is based on work done by myself jointly with others, I have made clear exactly what was done by others and what I have contributed myself.

Signed:

Date:

"I'm sciencing as fast as I can."

Hubert Farnsworth (Futurama)

UNIVERSITY OF NOTTINGHAM

Abstract

Faculty of Engineering

Mechanical, Materials and Manufacturing Engineering

Doctor of Philosophy

Synthesis and Characterisation of Multi-Substituted Hydroxyapatites

by Ben McCarthy

This thesis presents a range of novel mono and di-substituted hydroxyapatite powders, characterised by a range of techniques to ascertain their chemical composition, crystallographic composition, physical properties, and *in vitro* bioactivity.

The novel compositions consist of substituting a range of Borate, Sulphate, Silicate, and Strontium in levels ranging from 1.5 mol.%, up to 5 mol.%. It was found that a 4 mol.% inclusion of 2 mol.% Sr^{2+} and 2 mol.% ${SO_4}^{2-}$ gave a significant increase in the amount of osteocalcin produced and may represent an improved biomaterial warranting further study.

Acknowledgements

This project has been an extremely long road for myself, and behind the scenes my friends and family have been there to help me keep slogging even when it felt too much. Without that support network I would have fallen many times - for which I am eternally grateful.

I would also like to take this opportunity to thank my supervisors, Prof. David Grant, Dr. Colin Scotchford, and Dr. Phil Jackson. Through their patience and experience I have been able to navigate both a tricky subject matter, and the logistical nightmare that is doing a PhD part time. Of particular note I would like to thank my industrial supervisor, Dr. Phil Jackson, who not only helped me wrangle with regular technical oddities during the doctorate, but also acted as a mentor for me in the beginnings of my professional career. I would also like to extend my thanks to the whole team at Lucideon who supported me on every step of the way.

Contents

Declaration of Authorship **i**

Abstract **iii**

Acknowledgements **iv**

Contents **v**

List of Figures **viii**

List of Tables **x**

1 Introduction **1**
1.1 General Overview 1
1.2 Market Drivers 1
1.3 Current Materials Solutions for Bone Defect Filling Implants 2

2 Project Aims and Objectives **4**

3 Literature Review **5**
3.1 Bone - Structure and Functionality 5
3.2 Bone Void Filler Materials 8
3.3 Ceramic Scaffolds and Pre-Clinical Testing 14
3.3.1 Assessment of Cellular Functions 25
3.3.2 Cytotoxicity 25
3.3.3 Functionality 27
3.3.4 Proliferation 27
3.3.5 Specific Activity 28
3.4 Advancements to HA via Substitution 28
3.4.1 Strontium 29
3.4.2 Magnesium 30
3.4.3 Silicon/Silicate 31
3.4.4 Boron/Borate 32
3.4.5 Sulphur/Sulphate 33
3.5 Foaming 33
3.5.1 Direct Foaming 34
3.5.2 Phase 1 - Wet Processing 34
Mechanical Bubble Formation 34
Bubble Stability 36
Surfactants and Pickering Emulsions 39
3.5.3 Phase 2 - Drying 40
Wall Density 40
3.5.4 Phase 3 - Firing 41

3.6 Background Theory . . . 42
3.6.1 Ca:P Ratio . . . 42
3.7 Hydroxyapatite Synthesis . . . 45
3.7.1 Wet Chemical Precipitation . . . 45
3.7.2 Hydro/Solvo Thermal . . . 46
3.7.3 Solid State . . . 47
3.7.4 Combustion Synthesis . . . 47
3.7.5 Comparative Chart . . . 48

4 Experimental **51**
4.1 Introduction . . . 51
4.2 Co-Worker Contributions . . . 51
4.3 Sample Preparation . . . 52
4.3.1 Materials Sourcing . . . 52
4.3.2 Powder Synthesis . . . 52
HA Synthesis . . . 52
Mx-HA Synthesis . . . 53
Ca-source Variation . . . 54
Di-Substituted HA . . . 54
^{11}B-HA . . . 55
pH Control . . . 55
4.3.3 Structure Consolidation . . . 55
4.3.4 Foaming . . . 61
Foaming Trials . . . 61
Foaming Di-Substituted HA Method . . . 61
4.4 Characterisation . . . 62
4.4.1 Chemical Analysis . . . 62
4.4.2 Physical Analysis . . . 63
4.4.3 Chemical Analysis by FTIR . . . 64
4.4.4 Morphology Analysis by SEM . . . 65
4.4.5 Structural Analysis by XRD . . . 65
4.5 *In Vitro* Analysis . . . 66
4.5.1 Metabolic Activity . . . 66
4.5.2 DNA Concentration . . . 67
4.5.3 Osteocalcin Assay . . . 67
4.5.4 Data Analysis . . . 68

5 Results **69**
5.1 Validation of Synthesis . . . 69
5.1.1 Firing Temperature . . . 69
5.1.2 Ca:P Ratio . . . 69
5.1.3 Ca Source . . . 71
5.1.4 Boron-Substituted Hydroxyapatite . . . 74
5.2 Foams . . . 89
5.2.1 Foam Trial Methods . . . 89
5.2.2 Mx-HA Powder Slurry . . . 89
5.2.3 Mx-HA Foam Physical Characterisation . . . 95
5.2.4 Mx-HA Chemical and Crystallographic Characterisation . . . 97
5.3 Cell Characterisation Data . . . 108
5.3.1 HA Foam Trial Characterisation . . . 108

5.3.2 Mx-HA Foam Characterisation 108

6 Discussion **114**
6.1 Introduction 114
6.2 Synthesis of Substituted Hydroxyapatites 114
6.2.1 Mono substitution of Hydroxyapatite with Strontium, Borate, and Sulphate by a wet-chemistry precipitation method 114
6.2.2 Effect of Ca^{2+} Source on Hydroxyapatite Formation . 121
6.2.3 Dual Substitution of Hydroxyapatite by a Combination of Silicate, Sulphate, Borate, and Strontium . . . 124
6.2.4 Effect of Firing Temperature on Crystal Structure and Phase Stability 128
6.2.5 Adaptation of the Hydroxyapatite Crystal to Accommodate Substitution 131
6.3 Production of Foams 135
6.3.1 Preparation and Characterisation of Foams 136
6.3.2 Multi-Substituted Hydroxyapatite Foams 138
6.4 Biological Assessment of Materials 146
6.4.1 Cell Viability on Various HA Foams 146
6.4.2 Mx-HA Foam Cell Analysis 147

7 Conclusion **151**

List of Figures

3.1 Bone Heirarchy 6
3.2 Bone : Cell Interaction 8
3.3 Foaming Stages 35
3.4 Force vs Distance 38
3.5 Surface tension vs surfactant concentration 39
3.6 Relationship of mol. % and phase composition 44

5.1 Phase composition after firing at 600 °C 70
5.2 Phase composition after firing at 1000 °C 70
5.3 Phase composition after firing at 1120 °C 71
5.4 pH vs H_3PO_4 addition resulting in an acidic system 72
5.5 pH vs H_3PO_4 addition resulting in an alkali system 72
5.6 Phase composition and Ca:P ratio of mono-substituted HA . 73
5.7 Phase composition and Ca:P ratio of various Ca source at pH 9 75
5.8 Phase composition and Ca:P ratio of various Ca source without pH modification 75
5.9 Example XRD traces for fired HA precipitated without pH control 76
5.10 Example XRD traces for fired HA precipitated without pH control (30-40 2θ) 77
5.11 Example XRD traces for fired HA precipitated with pH control to pH 9 78
5.12 Example XRD traces for fired HA precipitated with pH control to pH 9 (30-40 2θ) 79
5.13 FTIR Spectra of Hydroxyapatite 81
5.14 FTIR Spectra of 2.5%B-Hydroxyapatite 82
5.15 FTIR Spectra of 5%B-Hydroxyapatite 83
5.16 FTIR Spectra of 10%B-Hydroxyapatite 84
5.17 FTIR Spectra of all ^{11}B-HA samples and pure HA 85
5.18 NB traces from HRPB 86
5.19 NB traces from HRPB - Peak Spotlight (i) 87
5.20 NB traces from HRPB - Peak Spotlight (ii) 88
5.21 Surface Area of Different Foaming Methods 90
5.22 Example Zeta vs pH curve for Si-HA 92
5.23 Example Zeta vs pH curve for Sr,B-HA 92
5.24 Example Zeta vs pH curvef for the fired material 93
5.25 Example Zeta vs pH curve for the fired material 93
5.26 Example Mercury Intrusion Plot 98
5.27 Sr,Si-HA Foam SEMs 99
5.28 Si,S-HA Foam SEMs 99
5.29 Sr,B-HA Foam SEMs 100

5.30 Sr,S-HA Foam SEMs . . . 100
5.31 Si,B-HA Foam SEMs . . . 101
5.32 S,B-HA Foam SEMs . . . 101
5.33 Sr,Si-HA r.r. Foam SEMs . . . 102
5.34 Si-HA Foam SEMs . . . 102
5.35 HA Foam SEMs . . . 103
5.36 Phase composition and Ca:P ratio of multi-substituted hydroxyapatite . . . 103
5.37 XRD traces for fired Mx-HA (First 5 samples) . . . 104
5.38 Example XRD traces for fired HA precipitated with pH control to pH 9 (30-40 2θ) . . . 105
5.39 XRD traces for fired Mx-HA (First 5 samples) . . . 106
5.40 Example XRD traces for fired HA precipitated with pH control to pH 9 (30-40 2θ) . . . 107
5.41 Alamar Blue data for various foaming methods after 3 and 6 days . . . 109
5.42 Alamar Blue data for multi-substituted Hydroxyapatites after 7 and 21 days . . . 110
5.43 DNA concentration data for multi-substituted Hydroxyapatites after 7, 14, and 21 days . . . 111
5.44 Alamar Blue data normalised against DNA . . . 112
5.45 Osteocalcin data for multi-substituted Hydroxyapatites after 14 and 21 days . . . 113

6.1 Schematic of large scale HA synthesis . . . 116
6.2 Schematic for the thermal degradation of hydroxyapatite via tetracalcium phosphate . . . 120
6.3 Schematic for the thermal degradation of hydroxyapatite via monetite . . . 120
6.4 Diagram of different hydroxyl orientation in hexagonal and monoclinic hydroxyapatite . . . 123
6.5 Firing Schedules . . . 129
6.6 Zeta Potential of the Slurry Versus the Pore Volume . . . 139
6.7 Surface Area Versus Porosity . . . 140
6.8 Zeta Potential Versus Surface Area . . . 140
6.9 SEM Comparison of Surface Features on Mx-HA Foams . . . 142
6.10 SEM Comparison of Surface Features on Mx-HA Foams . . . 142
6.11 SEM Inspection of Strut Porosity in Foams . . . 144
6.12 SEM Comparison of Different Foaming Methods . . . 144
6.13 Literature Example of Fired HA Foam Surface . . . 145
6.14 Comparison of Cell Activity Versus Surface Area . . . 147
6.15 Osteocalcin levels at day 14 and day 21 . . . 149

List of Tables

3.1 HA crystal size in bone 7
3.2 BVF composition overview 10
3.3 Comparison of recent cell testing in the literature 17
3.4 HA synthesis comparison 49

4.1 Substitution precursors 54
4.2 Calcium sources 54
4.3 Reagent mixes of all experiments 56
4.4 Foam trial samples 62

5.1 Mono-substituted HA Chemical Compositions 73
5.2 Mono-substituted HA Phase Compositions 74
5.3 FTIR Stretching Frequencies for B-HA 80
5.4 Multi-Substituted HA precipitate zeta-potential values . . . 91
5.5 Multi-Substituted HA fired powder zeta-potential values . . 94
5.6 Surface Area and Porosity of Mx-HA Foams 96
5.7 Multi-substituted HA Chemical Compositions 97
5.8 Multi-substituted HA Phase Compositions 98

6.1 Multi-substituted HA Chemical Compositions 118

1 Introduction

1.1 General Overview

The orthopaedic market, whilst currently valued at approximately $35 billion [1, 2, 3], is relatively young in comparison to other healthcare markets. Whilst the first hip replacement occurred in 1891 utilising ivory to form a new femoral head, it wasn't until 1940 that the first metallic hip replacement was implanted by Dr. Moore [4]. As time has progressed, the range of implants utilizing a developing materials science has subsequently grown, with hard tissue replacements now utilizing materials ranging from plastics, to metals to glass/ceramics.

1.2 Market Drivers

The orthopaedic market is currently heavily driven by the aging population, both as a combination of improved care for the elderly extending lifespans, and the aging 'baby-boomer' generation. Additionally changes in lifestyle and a wider knowledge of orthopaedic surgery (accompanied by higher expectations of said surgery) is resulting in the average age of patients to receive their first implant to drop, for example recent studies suggest that by 2016 over 50% of all total knee replacements will occur on patients aged under 65 [5].

These factors combine together to give an environment where existing implants are no longer suitable. Implants are needing to last significantly longer with an expectation amongst patients to maintain the quality of life they had previously.

The orthopaedic market may be based upon the type and style of surgery performed. In general, orthopaedic devices are either:

- Tissue Replacement of specific bone structures (i.e. Hip Implants, Knee Implants, Spinal Cages, Cranial Plates)
- Tissue Fixation (i.e. Plates, Screws)
- Tissue Scaffolds (i.e. Bone Void Fillers (BVF))

This last area is a rapidly growing field with significant financial backing from large orthopaedic companies aiming to position themselves as the 'best on market' – for example, Baxter's acquisition of Apatech (2011) in order to secure the leading next-gen ceramic BVF.

1.3 Current Materials Solutions for Bone Defect Filling Implants

The most successful material used for orthopaedic implantation, and regularly hailed as the 'gold standard' is the patients own bone [6], harvested from another location within the body (typically the iliac crest). This material is referred to as an autograft. Autograph material has some drawbacks that severely limit its application – most importantly the requirement to perform a secondary surgery to harvest the bone. This trauma acts as an additional stress on the body, as well as another potential source of infection. These risks are very significant when considering the scale of the surgery being performed to need the material being harvested.

Similar in nature to an autograft are allografts, where the material comes from a donor, and xenografts, where the donor is of a different species. Allografts are used, however bone banks are in short supply and the cost of allografts is therefore prohibitively high for many procedures. There also exist concerns relating to disease transmission from allographs with reports putting the risk of bacterial infection as high as 12% for 'massive bone allograph' and 0.7% for 'non-massive allographs' (i.e. bone chips) [7]. The risk of viral transmission is significantly lower, but still not negated. Equally the risks with xenograph are that there will be inter-species disease transmission with a notable example being Creutzfeldt–Jakob disease (CJD).

Outside of auto/allo/xeno-grafts, materials science provides highly specialized devices that offer a lot of the benefits of allografts, but without the significant costs and dangers associated with them.

Several different materials exist both in wide market circulation, and in research laboratories across the planet for use as a void filler. Considerations range from biologically enhanced fillers (i.e. Bone Morphogenic Protein (BMP) infused replacements – INFUSE® from Medtronic) [8], to composite materials (i.e. Polymer/Calcium Phosphate composite – chronOS from Synthes) [9], to resorbable metallic implants [10], and finally – fully ceramic implants (i.e. Actifuse from Apatech/Baxter).

By far, the most commonly used materials for void fillers are ceramic based, with most implants favouring a calcium phosphate phase (such as TriCalcium Phosphate (TCP), Hydroxyapatite (HA), OctaCalcium Phosphate (OCP)) due to its inherent chemical similarity to naturally occurring bone. Within the sphere of ceramic void fillers, there still exist large variations across product and research ranges with various porosities (ranging from macro-, to micro-, to nano- porosity), granulate forms (size and shape), and physical form (injectable pastes, solid granulates, mouldable putties, sculptable blocks) [11]. In addition there is a growing interest in various substitutions and chemical alterations to the base ceramic material, with interests around how surface charge and chemical signaling can affect the biological response – an example of this is Actifuse developed at Queen Mary University (QMU) and spun out in 2001 which due to the inclusion of silicate into the HA lattice has been able to grow a large market share due to their impressive data regarding bone regrowth and repair. This success has heralded a widespread interest in investigating the inclusion of different ions into biomaterials to enhance performance.

By developing synthetic implants with controllable physical, chemical and crystalline characteristics there is a hope that a synthetic implant may be developed that can surpass the repair potential of autograft materials with result of lower cost and less invasive treatment with no secondary operation for the patient.

2 Project Aims and Objectives

The aim of this project is to produce a porous inorganic scaffold that is an effective alternative to autologous bone and can provide a suitable alternative. The scaffold would find applications as a void filler for replacement of large bone defects and would be remodeled and resorbed by the body over time. The material is not intended to be load-bearing

In order to make progress towards the aim of the project, the following objectives for the project were as follows:

1. Devise a suitable method for the consistent synthesis of novel multi-substituted hydroxyapatites
2. Develop a suitable method for forming a 3D structure with the novel ceramic
3. Characterise the material chemically, physically, and biologically *in vitro*

3 Literature Review

3.1 Bone - Structure and Functionality

As this project looks to develop a material that is used for as a void filler, it is important to consider how skeletal bone is structured, and how it is interacted with by cells.

In maintained bone (i.e. trabecular, and cortical) HA is typically found as a series of thin plates that are produced in a tightly overlapping array and crystallised around a collagen fibre. These fibres are interwoven to produce a fibril array that then forms a larger pattern with other fibril arrays. These patterns can take on a variety of features depending on the role of the bone which they make up. These patterns form into cylindrical structures called osteons, which ultimately make up bone, with differing porosities giving trabecular or cancellous bone. These 7 levels of hierarchy are described in the model from Weiner and Wagner [12] figure 3.1.

Further variation between the characteristics of HA in the body can be seen in crystallite size, shape, total crystallinity and how it is produced. Skeletal bone exhibits a cell-based support structure via fibroblasts, osteocytes, osteoblasts, and osteoclasts. These cells control the shape and structure of the bone through a complex inter-play between the different cells. The process by which bone is deposited is covered later on. In cancellous bone, crystallites have been determined to have a size ranging from 30 nm x 20 nm x 1.5-2 nm (SAXS and TEM determination) to 200-30 nm x 200-30 nm x 3-10 nm (AFM determination) – further examples are presented in table 3.1. [13, 14, 15, 16, 17]

It is speculated that the size and shape of these bone crystals is to provide a two-fold benefit. One the one hand, the small particle size (and therefore the high surface area) allows for a higher level of solubility, thereby allowing osteoclasts to resorp them, whilst the small thickness allows key mechanical benefits, such as preventing crack propagation [18]. Of additional interest is the level of crystallinity to be found in these structures. In naturally occurring HA, the level of crystallinity is often low [19], with new HA crystals having a larger amorphous content that is reduced by aging. This

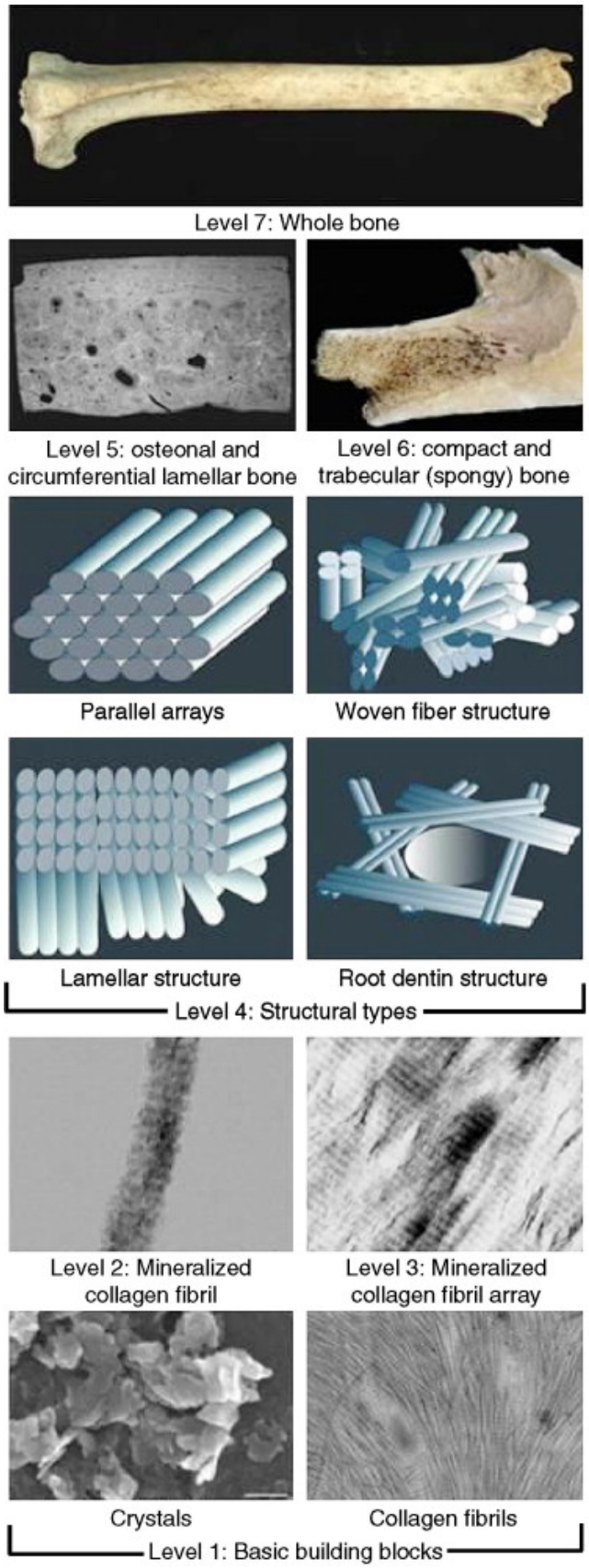


FIGURE 3.1: Weiner and Wagner Model of Bone Hierarchy demonstrating the architecture of bone from individual crystals through to the functional macro-structure (Image from 'Whole Bone Mechanics and Mechanical Testing', A. Sharir et al., The Vet. Journal, July 2008, p8-17)

TABLE 3.1: Comparison of Different Measurement Techniques and HA Crystal Size detected in bone. This variation demonstrates that whilst the crystallites are all nano scale, and typically needle or plate like in their dimensions, that the total size is still open to interpretation (Table from, 'Progress in Crystal Growth and Characterisation of Materials', (2010), J. Gomez-Morales et al.)

Analytical Method	**Crystal Dimensions**
TEM	20 nm long x 3-6 nm wide
XRD	10-35 nm long
μXRD	17 nm x 3-5 nm
SAXS	50 nm x 25 nm x 1.5-2 nm
SAXS and TEM	30 nm x 20 nm x 1.5-2 nm
AFM	200-30 nm x 200-30 nm x 3-10 nm

amorphous content is again speculated to serve several purposes. Most obviously, it allows osteoclasts to rapidly remove the newly formed HA, thus allowing remodeling to occur. The low level of crystallinity also allows for various ions to be more readily substituted into the lattice, thereby allowing the mineral's characteristics to be tweaked to suit the current environment and to act as an adaptable ion reservoir.

These properties are important when considering replacement materials that are designed to resorp as it is well understood that surface characteristics [20] such as roughness [21] and particle size can play a major role in cellular activity [22].

In skeletal bone, synthesis and formation of new bone is started by the formation of a layered structure of collagen where each layer lies parallel to the fibres in that layer, but perpendicular to the layers above and below it. These fibres resist pulling forces exerted on the bony matrix. The collagen fibrils are secreted by osteoblasts to form an uncalcinated bone matrix (referred to as an osteoid). As the fibrils are secreted and calcified, some osteoblasts are enclosed within the hard matrix, where their cell function and morphology changes to that of an osteocyte [23]. This process of bone growth is continuous, and when tied to the erosive actions of osteoclasts, leads to the adaptive nature of hard tissue and its ability to be remodeled

Osteoblasts and osteoclasts work in a synergistic manner due to a hormone regulated feedback system whereby osteoblasts release signaling hormones that recruit and activate osteoclasts to the area where fresh bone is being deposited (namely MCSF and TNF11). However as progress continues osteoblasts also secrete *osteoprotegerin* which blocks the action of TNF11, thereby lowering the osteoclast activity. This level of synergism leads to a

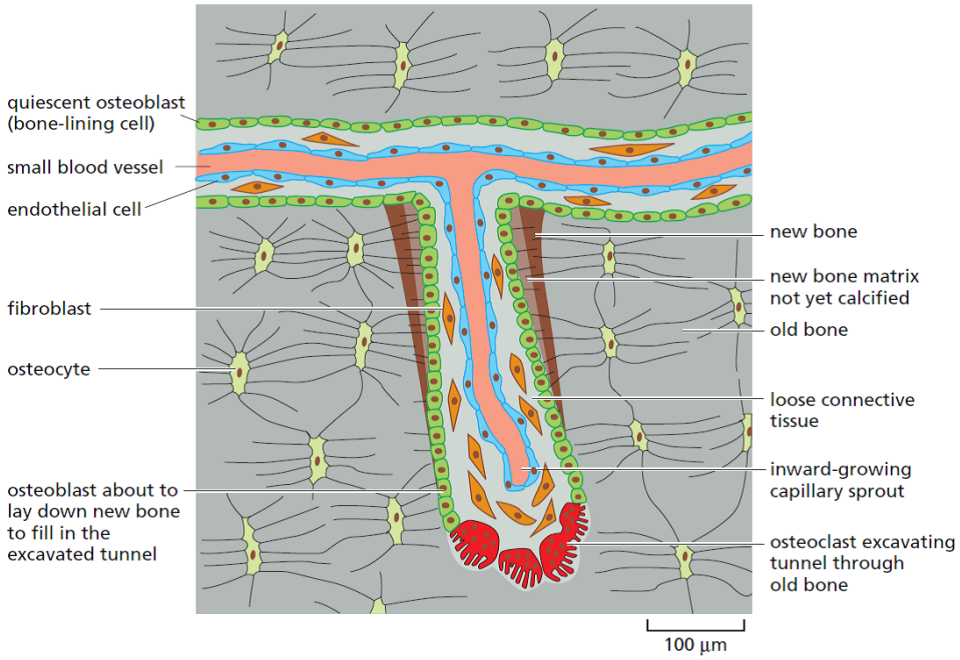


FIGURE 3.2: Schematic of Osteoclasts tunnelling followed by supporting cells (taken from 'Molecular Biology of the Cell', 5th Ed., p1473)

system whereby osteoclasts excavate tunnels through bone, followed by a workforce of osteoblasts, fibroblasts, and endothelial cells that develop new bone and supply blood flow to the newly imprisoned osteocytes [23]. This system of tunneling and rebuilding the shaft as its excavated gives rise to the formation of osteons [12]. This system is described visually in figure 3.2

3.2 Bone Void Filler Materials

When bone is damaged extensively, there exists a possibility for a void to be formed that is of either such a volume, or formed under such conditions, that the body cannot re-fill it naturally. In addition to the risk of extensive damage occurring, many surgical techniques involve the formation of large voids – for example wide excision for treatment of osteosarcoma, or preparation of a joint replacement site. Due to the variety of ways in which these voids can be formed, the potential working environment can vary wildly in terms of local tissue health, total volume and void dimensions. Additionally the need to repair aesthetic tissue (such as cranial and maxillofacial) or load bearing adds another degree of complexity to the implant.

Traditionally, voids were filled with bone, either harvested from the patient, or from a donor source. Whilst this still happens extensively (with a 1/3

share of a $2.5 billion industry in 2008) [24], an industry review published by the American Academy of Orthopaedic Surgeons in 2010 showed that there were significant benefits to using a synthetic BVF in certain situations thereby demonstrating that synthetics are of a level of efficacy to compete with allografted materials. This increase in efficacy mixed with the obvious advantages of reduced surgical procedures (as is the problem with autograft material), and consistent material (an issue with allograft material) marks synthetic BVF as a regular alternative to biologically derived BVF.

As can be imagined, with this huge disparity in clinical uses for bone void fillers (BVF), there is similarly a wide range of products available targeted at specific procedures. A small sample of current BVF products is presented in table 3.2. This list is not exhaustive, but provides an overview of the leading products along with market trends.

TABLE 3.2: Overview of some current BVF and a comparison of their compositions and application methods.

Product	Company	Material(s)	Application Method	Supporting Data	Comments
Endobon	Biomet	Biological Hydroxyapatite	Blocks, Granules	5 year follow up [25]	Post-operative follow up and radionuclide imaging showed healthy regrowth
Calcibon	Biomet	Ca-Deficient Hydroxyapatite	Paste, Powder	*in vivo* [26]	Histology slides up to 24 weeks
Pro Osteon 500R	Biomet	HA. Calcium Carbonate	Granules	*in vivo* [27, 28]	Histological slides
CONDUIT TCP Granules	DePuy Spine	TCP	Granules	*in vivo* [29]	Histological slides
HEALOS Bone Graft Replace-ment	DePuy Spine	Mineralized Collagen	Flexible Strips	Clinical Studies [30, 31]	Both studies are 2 year post-op follow ups
OpteMx	Exatech	HA/TCP Hybrid (60/40)	Granules, Blocks	*in vivo* [32]	Histological slides

Product	Company	Material(s)	Application Method	Supporting Data	Comments
INFUSE Bone Graft	Medtronic Spinal & Biologics	rhBMP-2 on Collagen Sponge	Many various forms	Extensive historical data [33, 34]	Controversy surrounds the off-label use of INFUSE, and a Yale commission found no significant benefit over autograft in terms of healing, but benefits over pain
MasterGraft	Medtronic Spinal & Biologics	HA/TCP Hybrid (15/85)	Granules, putty	Extensive historical data, *in vivo* [35]	
PerioGlas	NovaBone	Ca, PO_4, SiO_4 bioglass	Granules, powder, putty	Clinicals, *in vivo*, *in vitro* [36, 37]	Extensive background with clinicals dating back to 1997, and *in vitro* dating back as far as 1993
Vitoss	Stryker	TCP/Bioglass/(collagen)	Granulate, foams available with collagen	Extensive historical data, clinical trials [38]	Number 1 selling synthetic bone graft worldwide [39]
chronOS	Synthes	TCP/ Poly (lactide-co-ϵ-caprolactone)	Granulate, shaped foams	Clinical and *in vivo* data [40]	Synthes lauds its ability to be resorbed quickly, claiming a benefit to patient healing as a result.

Product	Company	Material(s)	Application Method	Supporting Data	Comments
CopiOS Bone Void Filler	Zimmer Spine	Dibasic CaP/collagen (67/33)	Sponge, paste	Clinical data and *in vivo* [41]	Zimmer suggest that having a moderately acidic environment promotes osteo-activity due to the higher availability of BMP, compared to the more basic environment found in TCP, HA, and Bioglass
Stimulan	Biocomposites	Calcium Sulphate	Pellet, paste	Clinical data, *in vivo* [42, 43]	Biocomposites report consistent clinical results, supported by consistent, high purity raw material. High level of bone re-growth attributed to comparatively rapid dissolution of $CaSO_4$
Actifuse	Apatech	Silicon substituted HA	Sponge, block, granulates	Clinical data, *in vivo*, *in vitro* [44, 45, 46]	Silicate inclusion is touted as the reasoning for the improved bioactivity.

As can be seen from the selection of BVF in table 3.2, excepting products that include biologically sourced material (which does make up a larger section of the market offering than represented above), most products utilize a ceramic system (11 of the 15), typically consisting of Calcium and Phosphorus (10 of the 15). Also of note is the fairly even split in the form of granulate/blocks and putties/pastes (9 vs 6), with each having their own benefits regarding ease of use for various sites. Granulates are useful for the larger voids, where their higher surface area and comparative strength can be useful, whilst putties are much more useful for filling into cracks and unusually shaped voids. For the purpose of this comparison, blocks and granulates are considered essentially interchangeable as a typical process to producing granules is to produce blocks which are then broken down.

The preference for ceramics is significant as the existence of Bioglass is not novel, and yet it doesn't receive as much commercial interest within the BVF field – notably bioactive glasses do find a lot of use in consumer health (e.g. Novamin in Sensodyne), dental restorations and in other more specialized fields such as cochlear implants [47] and RFID transponder implants [48] to name two. The author speculates that the lack of adoption of Bioglasses in orthopaedic fields is due to its relative difference from natural bone mineral, as opposed to Hydroxyapatite (HA). This difference may have been significant when attempting to get initial products through regulatory systems and then convincing surgeons to adopt the new technologies as the HA implants could claim similarities to the autograft and allograft materials in use at the time. Additionally the lack of patent protection on the structure of HA when first developed allowed an open field to drive innovation, which may have hampered Bioglass due to its patented nature. Since the start of this project (2012), bioglasses have become more prevalent in the BVF field due to the lapsing of patents surrounding their use. 3 examples of these new products are BonAlive® putty (S53P4 bioglass [49]), BioSphere® putty (45S5 bioglass [50]), and Unigraft® (simply referred to as 'bioactive glass', no composition given [51])

Unfortunately, due to the nature of the data typically supplied by medical device companies for the sale of their products, it is very difficult to draw any significant comparisons between various implants as the most relevant data is in the form of in vivo histology or post-operative clinical studies. Typically these studies include either autograph or allograph as the positive control, but due to a variation in animal models used, implant location, operative conditions, time points, and method of quantification it is a significant challenge to compare across products. This isn't always the case, and occasionally a company will commission a series of experiments to compare between their new product and a competitors [27]. As

an additional challenge, it is well known that *in vitro* is not easily comparable to *in vivo* results. Ultimately the best indicator of a successful implant is at what speed the patient is back at full recovery, and whether there is any degradation of the implants performance over time. As it stands, the current materials on the market show no major drop in performance over time as may be expected for a hip implant, for instance, and typical patient recuperation times are in the region of weeks to months depending on the scale of the surgery.

Due to the difficulty in comparing across various materials the next section will focus on Calcium containing ceramic materials, looking at the newer developments in their use as scaffolds and comparing their *in vitro* evaluations. Although *in vitro* cannot be used as a substitute for *in vivo* when considering ultimate implantation, it is a suitable screening method for establishing a general trend.

3.3 Ceramic Scaffolds and Pre-Clinical Testing

Whilst the materials in use in the market have been relatively static in terms of chemical composition, a large amount of research has been directed at developing superior implants by changing the pore structure or physical parameters of the implant. These changes have led to more biphasic materials, composites, and novel production methods in order to try and minimise the weaknesses and enhance the benefits of various available materials. These materials are typically tested through a variety of gating techniques to determine their potential clinical viability. Some of the tests to demonstrate bioactivity are now set as international standards (such as Simulated Body Fluid (SBF) tests, popularised by Kokubo, which is effectively ISO 23317). The adherence to more standardised testing protocols allows a much better comparison between materials (as the data can be better quantified and normalized), but this ease of comparison comes at the expense of clinical relation and so a compromise must be drawn.

Broadly speaking there are 3 main categories of pre-clinical testing that a biomaterial can undergo, with these being possibly further subdivided.

At the simplest level, there are a series of tests that can be performed in the absence of biological entities (either cells or full tissues), and merely utilise a buffered solution containing mostly inorganic salts, and possibly some level of organic compounds (for example the addition of TRIS as a buffer in SBF). There is currently a dispute within the academic community as to the suitability of SBF as a testing method. In 2006 Kokubo published a paper

that correlated time for apatite formation in SBF with speed of boney ingrowth into a defect in a rabbit model [52]. Bohner then went on to present a review of data demonstrating that SBF testing does not portray a complete picture as several key factors are omitted. This is exemplified in its inconsistent results (for example the poor result of β-TCP) and the variability of SBF compared to human blood serum [53]. Bocciccini lent further weight to the belief that SBF could give erroneous results with an investigation into the effect of TRIS on Bioglass solubility in 2011 [54]. In his 2009 paper, Bohner does suggest some modifications to SBF to bring it further into line with physiological values, however in all iterations of SBF, there is a noticeable lack of proteins or other biologics which are key in the actual event of bone remodeling. Whilst Bocciccini and his group are still exploring other possible buffered solutions [55] as a screening mechanism for bioactivity, although he does dismiss Dulbecco's Modified Eagle Medium (DMEM – a common cell media) as a suitable alternative. The use of SBF has been further reviewed elsewhere, with the authors openly dismissing SBF as having potential mislead other researchers due to uncritical application [56]. A recent collaborative effort between several high profile researchers has been published which focuses on how to improve the current ISO method based off the Kokubo SBF test (ISO 23317) [57]. The paper is a concise and effective series of recommendations for improvements to the method outlined in ISO 23317, supported with a round robin test at the end to validate the improved method. This paper further acts to highlight the additional testing required to get useful data out of the supposedly simple screening test. Beyond which, the tests used (i.e. XRD and FTIR) to check for a successful growth won't work with CaP ceramics (including HA) which are still the largest part of the market. Ultimately the paper shows value for comparison of glasses, but with the known issues of using SBF (i.e. different compositions acting differently, use of HA being difficult, difficulty and effort in running and retrieving data) it seems to reinforce the argument that simple in vitro tests would be easier and more representative. The authors themselves state; 'the aim is not to develop a method for predicting whether a material will form a bond with bone' - but rather that the aim is 'to develop a facile test that can be used in most research laboratories around the world and allow comparison of dissolution rates and apatite nucleation.'. Considering it can't be used with a range of different materials, and doesn't act as a predictor of bioactivity then the questions must be asked - what is the value? Potentially dissolution into a simulated biofluid (such as PBS, SBF, or even cell culture media) may be interesting for release of target ions (i.e. the inclusion of Sr into Stronbone).

The author sees merit in the offering of a solution to provide a convenient and relatively low-labour and cost screening of biomaterials so that

resource can be better directed, however from personal experience with SBF, would rather submit samples for a relatively simple *in vitro* cell assay looking at metabolic activity and cell count as an initial screening due to the extremely awkward nature of SBF preparation (namely its tendency to auto precipitate), and the questionable value of its data.

Table 3.3 lists a few recent papers looking at various *in vitro* and *in vivo* tests run on ceramic based scaffolds. The papers presented were chosen to give a broad overview of different tests used on a range of materials. The listing is not intended to be exhaustive. Whilst it is far from a complete overview of the recently published works on in vitro assessments of ceramic scaffolds (a simple search on Web of Science shows 719 results for papers published from 2010 to 2016 for 'in vitro ceramic scaffold'), it does cover the general assessments seen in the literature. A condensed list of tests often reported are:

- Apatite formation from SBF (running from 2 d – 28 d)
- Weight Loss in PBS (running 1 w – 12 w)
- Cell assays (running 1 d – 28 d)
- In vivo histology and microCT (running 1 m – 6 m)

Cell testing is required by regulatory bodies across the globe (such as the FDA and the EMA) for submission of a medical device. The cell testing carried out is often done to an ISO standard, of which ISO 10993-5 is a usual starting point. It's use is often as a first screen of a device, although for a full submission of a medical device seeking approval further, more detailed, *in vivo* tests are common. To screen samples in accordance with ISO 10993-5 samples can either be tested by direct contact of cells to the material, or by testing the extracted material (also known as conditioned media). As such it is a common technique to see reported, however due to the loose requirements of the ISO many papers do not report data normalised to specific characteristics (such as DNA count) making comparisons difficult.

TABLE 3.3: A comparison of recent literature regarding the methods of testing bioactivity of a cell scaffold. Whilst not comprehensive it allows a general overview of the prevalence of weight loss and SBF testing in favour of normalized cell results. In vivo are relatively common too with histology typically being the main method of data generation. Even in studies where there is both in vitro and in vivo data little effort is made to correlate the two – either because of how disparate they are (e.g. SBF and histology and the huge variation in method of action – albeit effectively the same measured result of HA formation), or because how specific the relative tests are (e.g. cell assays and histology where cell assays are looking at a very specific part of the picture, and the histology is considering the total scenario with its various inter-cellular effects).

Material	Structure	Test	Method Used	Results	Comments
Biphasic HA/TCP [58]	Robocast Scaffold	Weight Loss over 1 month	SBF	<1% weight loss	Whilst TCP is considered to be more soluble than HA, it still has a relatively low solubility. This in conjunction with SBF's super-saturation with regards to HA could conceivably cause a scenario where the scaffold was encased in a low solubility layer of HA, thereby effecting the results. Additionally the lack of biological action from osteoclasts, or even the regular changing of solution, will have greatly impacted the speed at which a steady state was reached

Material	Structure	Test	Method Used	Results	Comments
$CaSiO_3$ [59]	3D Printed Scaffold	Apatite Formation (2d and 4d)	SBF Apatite growth	Quick formation of apatite is shown with small amounts evident at 2d, and large formations present by 4d.	The lack of quantification is disappointing, especially as with a CaSiO base material, XRD could have been used to quantify apatite growth
$CaSiO_3$	3D Printed Scaffold	Weight loss over 21 d	Tris-HCl (pH 7.4)	25 wt% loss over 21 days	Compared to β-TCP (which showed 5% loss). This high level of loss could be useful for biological interaction, but it may also be too fast causing a loss of integrity at the implant site. The solvent was refreshed everyday meaning that a steady state wasn't reached for any extended period. How this compares to an implant site is debatable.
$CaSiO_3$	3D Printed Scaffold	*in vivo* histology	rat model	Slight increase in % bone formation	The group followed the dissolution study with *in vivo* trials reported in the same paper. The higher level of bone formation they attribute to the increased dissolution of the $CaSiO_3$ scaffold as opposed to β-TCP

Material	Structure	Test	Method Used	Results	Comments
HA / Wollastonite(WA [60])	Polymeric sponge replica	Apatite formation (7d)	SBF	Apatite formation	This research team points to the formation of SBF on the surface of the scaffold as a sign of bioactivity. This growth is not quantified. The lack of quantification, as well as reservations about the efficacy of SBF testing leaves a lot missing from this work.
HA / Wollastonite(WA)	Polymeric sponge replica	Weight Loss	Tris-HCl (pH 7.4)	33 wt.% loss	The inclusion of wollastonite causes a large increase in the solubility of the construct. This is likely due to the more soluble wollastonite dissolving out.
HA/TCP powder + PCL/Silk coating [61]	polymeric sponge replica	apatite formation (1-28 days)	SBF	Formation on the biphasic control after 21 days, precipitate covered the PCL/Silk layer after days, before re-dissolving	

Material	Structure	Test	Method Used	Results	Comments
HA/TCP powder + PCL/Silk coating	polymeric sponge replica	MTS assay (metabolic assay)	Human Osteoblastic Cells (HOB)	Similar values at day 1, 50-75% increase by day 7 for the PLA/Silk covered sample. PLA/Silk coated material showed a higher gene expression in all cases.	The lack of any DNA data to support these cell results means that it is impossible to attribute the improved response to cell activity. It is possible that the increased values demonstrate a higher rate of proliferation, or they could be indicative of a higher rate of individual cell activity. This difference can be partially attributed to variations in surface area and ability of the cells to bind to the surface, therefore possibly skewing the data.
HA/Silica [62]	Laser Sintered Scaffold	MTT assay	MG63 Cells	The sintered scaffold demonstrated much higher response than the green-state scaffold	With no control or DNA data available it is impossible to describe this data. The only piece of information that can be drawn from this is that the sintering of the scaffolds at 1200 °C showed a marked improvement in total metabolic activity
HA/Multi-amino acid [63]	Injection moulded foam	Weight Loss (12w)	PBS	between 35%-60% corresponding to porosity of 58% - 81%	A clear trend is seen between porosity and solubility. Some detail regarding the chemical state of the final scaffold would have provided insight as to whether it was the ceramic or polymer section that was dissolving

Material	Structure	Test	Method Used	Results	Comments
HA/Multi-amino acid	Injection moulded foam	MTT assay, Alkaline Phosphatase Assay (1, 4, 7 d)	MG63 Cells with Tissue Culture Plastic as a control	No significant difference at days 1 and 4, but day 7 showed an increase in both metabolic activity and ALP.	A lack of DNA data makes it hard to attribute the increased responses in either case to the material. The higher levels for the MTT and ALP results could be attributed to an increase in surface area from the 3-D scaffold over the flat culture plastic
HA/$CaSO_4$ [64]	Paste	MTT assay, Live/Dead assay (cell stain) (1, 3, 7 d) Gene Expression (Osteopontin, Osteocalcin, GAPDH)	MG63 Cells with Tissue Culture Plastic as a control	No significant difference between the two samples with regards to metabolic activity. Cerament Spine Support showed a slight increase in cell number	With the assays only being run over a 7 day period, it is hard to draw any significant trends relating to the materials bioactivity - a longer testing period would have allowed differences to be amplified. Additionally inclusion of an osteo-activity specific assay (such as ALP or Osteocalcin) would have allowed better distinction before picking Cerament Spine Support for rMSC trials.

Material	Structure	Test	Method Used	Results	Comments
HA/$CaSO_4$	Paste	Gene Expression (Osteopontin, Osteocalcin, GAPDH)	Rabbit Mesenchymal Stromal Cells (rMSC)	rMSC showed positive differentiation for OC, and negative expression for Osteopontin - indicative of osteoblastic differentiation	
HA/PLA [65]	Electrospun membrane	Apatite formation (7d)	SBF	HA deposits were seen on the HA composite and confirmed by FTIR	

Material	Structure	Test	Method Used	Results	Comments
HA/PLA [65]	Electrospun membrane	Mineralization (Fluorescent staining of deposited HA) (7, 14, 21 d), ToxiLight (Cytotoxicity assay - Adenylte Kinase assay) (3, 7 d)	Normal Human Osteoblasts (NHOst)	HA/PLA showed high levels of HA mineralisation after 7 days and plateaued shortly thereafter. The control sample showed minimal levels of HA formation, the PLA control reached levels equivalent to HA/PLA's day 7 result after 21 days. Pure PLA showed a 85% die off at day 3, compared to 50% die off in the HA/PLA composite. The control only showed a 20% die off.	As this study looked at mineralisation with both SBF and cellular activity it would have been interesting to see how they compared by quantifying the amount of HA formed by SBF. Failing that, running the SBF test to 21 days would have offered a nice comparison to the cell mineralisation, especially as the PLA membrane showed significant HA mineralisation between day 14 and day 21. The reduction in die off from the HA/PLA composite can be theorised to be due to the presence of the HA material. Some die off is to be expected when seeding, but the cause for a >80% die off could do with explaining. As the polymer being used is PLA, it is likely that there is an acidic environment generated which may have contributed to this.

Material	Structure	Test	Method Used	Results	Comments
HA/PLA [65]	Electrospun membrane	ViaLight (ATP Assay) (3, 7 d), ALP Assay (7, 14 d)	Normal Human Osteoblasts (NHOst)	PLA and HA/PLA both showed a significantly lower metabolic activity that the control. No ALP was detected at 7d, with PLA showing 5 mg/mg total protein and HA/PLA showing 8.5 mg/mg total protein after 14d	The units for the ALP assay are nonsensical; it is assumed to be a typo and meant to be expressed as μg/mg total protein. Ignoring the units and focusing on the trend it is clear that the PLA fibres are accountable for some level of osteo-activity, perhaps explaining the mineralisation seen after day 14, however the HA/PLA sample also shows no ALP at day 7, and yet there is a large amount of mineralised content. There is a potential that the mineralisation assay has bound to the existing HA present in the samples, as it isn't clear if a baseline run was carried out with the samples to check.

Conditioned media is a broad technique; with the FDA supplying 4 suggested methods and 2 suggested media, although both with the caveat that a different media or conditioning protocol can be followed so long as a suitable reason is provided. An example preparation would be to immerse a powder in a volume of culture media, for example Dulbecco's Modified Eagle's medium (DMEM). This would then be left unstirred for 24 hours, at 37 °C. This media is then used for culturing cells on tissue culture plastic as a neutral surface. At the end of the experiment, a suitable assay is run to determine cytotoxic effects. By following this protocol, assays can be run to determine whether the local environment generated by the biomaterials is conducive to cell health and growth. It also has the added benefit of being easy to run when handling fine powders which are difficult to manipulate within well plates.

Direct contact on the other hand, involves placing cells in contact with the material itself. This can be achieved in a variety of ways, but typically it is either a case of pre-culturing a layer of cells in a well, before placing the material on top to allow migration (useful for heavier powders and the like); or to place the material in the well prior to cell addition, and thereby directly seed the cells onto the material. This is then cultured as standard and a suitable assay is run to determine cytotoxic effects. Both manners of inducing direct contact are recommended by the ISO. This experimental constraint makes testing primary powders difficult, and so materials will often be processed to some extent prior to cell testing. An additional benefit of running tests on processed samples is the relatability of the results to a potential product; hence a benefit can be seen to working with foams and granules over a pressed disc.

3.3.1 Assessment of Cellular Functions

There is a wide range of possible assays available. Each assay deals with a specific cell function which may be affected by culture conditions, and as mentioned, some are required for FDA submission whilst others provide data which can be commercially of scientifically more relevant.

3.3.2 Cytotoxicity

Cytotoxicity is an assay area which is required for FDA submission of a biomedical device. Whilst the various testing methods are described above, the choice of assay is still an involved process.

The general process for cytotoxicity testing is to demonstrate that the cells are still viable by virtue of a assay measuring either the metabolic activity

of a cell (i.e. MTT), or by a measure of the integrity of the cell (i.e. LDH, neutral Red – two assays that indirectly check the cell's integrity by measuring a protein that is released during tissue damage and active dye uptake respectively). There are many different assays with differing positives and negatives [66], but they all work by providing a dye which is reduced by the cell, thereby either adding or moving a UV-Vis absorbance or fluorescence peak, where the difference can be quantified. Alternatively, counting assays can be used to determine cytotoxicity. Counting assays typically use a stain which either stains living cells, and thereby living cells can be counted. It is possible to add a stain which will only stain dead cells, which can allow a comparative test.

ISO 10993-5 describes four different assays, two metabolic and two stains. The two metabolic assays described are MTT and XTT. Both MTT and XTT use similar tetrazolium compounds which are reduced by mitochondrial dehydrogenase to an insoluble formazan compound which can be detected by absorbance to give a measure of cell metabolic activity. Another similar assay within the tetrazolium family is MTS. The significant drawback to MTT and related assays is the requirement to sacrifice the cells due to the toxic nature of the assay, thereby not allowing continuous monitoring of a sample of cells. An alternative metabolic assay which is gaining traction is Alamar Blue. Alamar Blue is a one-step metabolic assay that is highly stable and non-toxic, allowing continuous monitoring of the same sample [67]. Alamar Blue works by the reduction of a blue dye (Resazurin) to a yellow dye (Resorufin) which fluoresces and is therefore a measure of metabolic activity.

The two staining methods described in ISO 10993-5 are Neutral Red and Giemsa. Giemsa staining of DNA in a cell, is followed by a simple count to see how many cells are present across the sample. This number is compared to a control sample to determine cytotoxicity. In comparison, Neutral Red (NR) allows two methods of determining cell viability. The NR dye is taken up by lysosomes and so can either be observed under a microscope, giving a similar count to Giemsa, or the remaining dye can be detected, and used to measure cell viability. Effectively, the less dye remaining, the more viable cells and/or the more capable the surviving cells are – of note is the fact that the measuring the dye concentration does not give a number of cells [68]. This marks NR as a superior assay to simple Giemsa staining, however it does allow for a significant margin of error based on operator skill and ISO 10993-5 recommends that stain counting should be backed up by alternative checks – either a secondary stain, or a metabolic assay (MTT/Alamar Blue). A further staining method that can provide a very beneficial visualisation of the material surface is a di-dye system that utilizes Calcein-AM to

stain live cells green, whilst the addition of Propidium Iodide stains dead cells red. This can provide in one image a comparison of live cells vs dead cells so that particular areas can be visualised – i.e. if there is a stain/defect that is cytotoxic, the cells seeded there will be red, as opposed to the rest of the sample.

3.3.3 Functionality

Beyond cytotoxicity, there are no requirements for cell testing from a regulatory viewpoint, however cell testing does allow the investigation of other parameters which can be of scientific interest (by helping to understand the mechanism of action for a material), or of commercial interest (by providing data to entice customers into buying into a technology/material/device). Relevant tests beyond cytotoxicity are reviewed in the following sections

3.3.4 Proliferation

In order to measure proliferation across a sample, cell staining can provide a clear visual cue as to the response, however this method is really only semi-quantitative at best, and shows significant failings when dealing with a porous material where there are surfaces not in line of sight. A superior method is to look at indicators such as DNA count and total protein levels of the sample. These assays are relatively simple.

For DNA counting, it is a simple matter of lysing the cells so that the DNA can be reached by the appropriate dye. A typical assay used in this scenario is PicoGreen. PicoGreen works by binding to DNA which causes a 1000 fold increase in its fluorescence. It is also possible to use Propidium Iodide in the same way as using it to dye a sample for counting, but having first lysed the cells.

When attempting to quantify protein in a sample, but when specificity is not required (i.e. for a total protein count) the most common method is the Lowry method [69]. The Lowry mechanism utilizes the reductive properties of the peptide bond to reduce Cu^{2+} to Cu^{+} which is then bound by a chelating agent which fluoresces. There are many variations on the original 1951 method such as the Smith assay [70] and the Hartree-Lowry assay [71]. Alternatively, the Bradford assay is also suitable. The Bradford assay has its own problems in that it is protein dependent, so it is useful for comparing across samples, but not across different cells.

3.3.5 Specific Activity

The previous assays are all related to proliferation and do not assess phenotypic responses. When looking at a biomaterial which is intended to improve cell response in a hard tissue environment (typically bone formation/turnover), there are further assays which can provide useful data.

- Alkaline Phosphatase (ALP) – Alkaline phosphatase is the enzyme responsible for removing phosphate from ATP to produce ADP. In bone it is used in highly elevated amounts for the interaction with the Calcium Phosphate component of bone. Care has to be taken with this assay as the enzyme being measured (ALPL – tissue non-specific) is found in other tissues not related to bone-modeling (kidney, liver). The assay typically used to measure ALP concentration is a substrate which is reduced by the enzyme to a dye whose concentration can be tracked colourimetrically. As such data generated from this assay is a measure of ALP activity. This number can be normalised against the DNA count of the sample to give an indication of whether the difference in activity is to be attributed to increased cell count, or increased cell activity.
- Osteocalcin – Osteocalcin is a protein involved in the production of new bone and is secreted by osteoblasts [72]. Osteocalcin, like ALP, can be used as a direct measure of bone-turnover and cell activity. Due to its important nature in bone-biology, there exists many commercially available assays [73] with them falling into two general methods – enzyme labeled assays, or radiolabeled.
- Collagen type 1 (Col1) – Col1 is the most abundant form of collagen in the body and is utilized in bone reconstruction as an initial matrix former prior to remineralisation, at which point it is incorporated as the organic component of bone and aids structurally.

A suitable initial screen would include general cell health and some osteo-activity indicative assay, as such the author recommends a DNA assay to allow normalising, Alamar Blue to perform a check on cell metabolism (chosen over the similar MTT assay due to ease of use and the non-destructive nature of the assay), with ALP and Osteocalcin as a screen for osteo-activity.

3.4 Advancements to HA via Substitution

With the advent of Actifuse (Trade name for Si-HA), it was shown that biomaterials incorporating secondary ions as a modification could deliver a large benefit to the finished device. In Actifuse the inclusion of silicate has

been shown on multiple occasions to deliver a significant benefit (as measured by rate of mineral apposition, and rate of total fusion) to the speed of wound healing [46, 45]. More recently, ionic Strontium (Sr^{2+}) has been shown to combat osteoporosis when delivered as strontium ranelate [74]. This development has led to a range of groups looking at the inclusion of Strontium into glasses [75] and ceramics [76]. Substitution levels within HA have been reported up to 15% [77]. The incorporation of Sr has been shown to alter the bioactivity of HA, although the method of action is still under investigation as co-run studies using $SrCl_2$ did not show the same increases to cell activity, there ruling out a simple Sr^{2+} dissolution as the main mechanism for action [76].

The inclusion of secondary ions has been heavily researched in glass and glass-ceramic materials, likely due to the ease of substitution/inclusion. A comprehensive review of the topic was produced by Hoppe et al. in 2011 [78]. In this review, several ions were mentioned (Si, Zn, Mg, Sr, Cu, and B) independently, with combinatorial effects described for others (F, Ag, Ti, Na). Beyond the scope of Hoppe's review, sulphate is also found in biomaterials and its incorporation into HA is of interest to the author. The inclusion of Fe is also being investigated in a variety of materials (i.e. glass [79], HA [80])

Whilst the ultimate aim of all this research is to produce a superior implant material, the target application has an impact on what is classed as a criterion for 'superior'. For instance, the paper introducing Fe into the HA lattice is doing so in order to address toxicity concerns around iron-oxide superparamagnetic nano particles used for a range of applications.

With this in mind, the scope of which substitutions we are interested in can be narrowed. Considering osteoactivity as a freestanding metric of efficacy, substitutions looking at providing anti-microbial activity (Ag, Cu), anti-inflammatory (Zn) activity, or decreased solubility (F) can be ignored, along with other substitutions that have vague benefits (such as Ti and Na). This leaves a list of substitutions such as Sr, Mg, Si, B, and S to review as potentially adding to the osteoactivity of a ceramic material.

3.4.1 Strontium

Due to its prevalence in bone mineral Sr was until recently utilised in osteoporosis treatments as Strontium Ranelate where it has demonstrated a significant benefit to bone healing [81, 82]. It's inclusion in biomaterials – specifically glasses [83, 84, 85] and calcium phosphate ceramics [86, 87], is well documented as providing a beneficial effect from surface modification and ion release.

The method of strontium action in preserving bone mass is understood to be attained through modulation of the Calcium Sensing Receptor (CaSR), ERK1/2-MAPK and NFATc/Wnt signaling pathways [88]. Modulation of these pathways promotes fibroblastic differentiation towards osteoblasts (which are derived from mesenchymal stem cells) whilst simultaneously inducing apoptosis in osteoclasts (which are derived from hematopoietic stem cells).

Of particular note regarding Sr, it's inclusion into HA has been well documented, with recent work by Gibson investigating co-substitution of Sr with Mg [89].

3.4.2 Magnesium

Magnesium release has been demonstrated to stimulate new bone formation, both as a substitution in alumina [90], and as a substitution in HA [91]. It is theorised that this increase in bioactivity is due to Mg^2+ interacting with integrins (trans-membrane receptors).

Inclusion of Mg^2+ into the HA lattice does not strain the calcium sites excessively, although the low solubility of $Mg(OH)_2$ can cause issues when choosing precursors. This limitation rules out using $Ca(OH)_2$ as the calcium source, or to run the synthesis by precipitation due to the high pH used.

Mg Doping of HA composites has shown benefits, although there are limitations to the assay used. In a paper by Bodhak *et al.* [92] it was shown that pre-treating a composite with either Ca-ions, Mg-ions or a mixture of both lead to maximum viable bone density being reached by all scenarios.

The presence of magnesium is reported to both positively and negatively effect the precipitation of HA. The presence of Mg was shown to decrease the rate of growth of HA crystals on enamel seeds [93]. This has been linked to the precipitation of an amorphous phase that crystallises to TCP on heating. A surprising paper on HA formation in differing soil chemistries has demonstrated that at higher pH levels, Mg does not cause inhibition of HA formation [94]. Alongside the inhibition of HA crystal growth from precipitate mixtures, Mg also stabilises β-TCP at higher temperatures, making the phase more resilient to the firing regime[95]. This can be of benefit when attempting to produce a highly crystalline bi-phasic material.

3.4.3 Silicon/Silicate

The benefits of Silicate inclusion into HA have been discussed in detail above when describing the data utilized by Apatech in marketing the product Actifuse (Si-HA). Silicate inclusion is known to be of benefit to the bone growing process [96] - both as a dietary supplement and as a constituent of a bone replacement material (such as Actifuse or Bioglass). $Si(OH)_4$ has also been shown to stimulate Col1 formation, as well as osteoblastic differentiation in MG63 and HCC1 [97].

Whilst it is often assumed that it is the release of silicate that stimulates the improved biological response, Bohner elegantly dismantles the premise in his 2009 paper on the subject [98]. Bohner shows that there is no evidence to demonstrate that silicate is dissolved out of the Calcium Phosphate lattice at a meaningful concentration, and that the changes to bioactivity of silicate inclusion into hydroxyapatite may be down to a number of effects; such as Si-release, enhanced Ca-release, change of surface charge, or change in surface topography. With this in mind, the author believes that when attributing the effect of silicate inclusion it is important to support *in vitro* and *in vivo* observations with detailed chemical analysis. It is clear that the role silicate plays is complex as benefits are seen from materials that are effectively inert (i.e. substituted hydroxyapatite which displays such low solubilities that ionic release of silicate is not approaching therapeutic levels). It is also shown that the inclusion of silicate leads to the loss of a hydroxyl group to balance the charge. This re-balancing of charge leads to a reduction in surface charge (-50 $\pm$5 mV to -71 $\pm$5 mV [99]), which in turns benefits Ca^{2+} absorption, which is the first step in protein and cellular attachment. Whilst dissolution or ion exchange as a mechanism for the release of therapeutic levels of silicate are not possible, there does exist the potential for local concentration spikes as a result of cellular activity - such as osteoclastic erosion of the material surface. Such an event may allow the effects seen from straight ion concentration studies to manifest without the bulk concentration being at the levels required for such a response.

The literature is full of papers discussing the possible modes of action for silicate enhanced bone repair. Wu and Chang produced a comprehensive review on silicate activity when released from silicate ceramics [100] (such as Calcium Silicate, as opposed to substituted HA), whilst Hing has a raft of papers exploring the effects of silicate substitution into HA, with an informative piece on the effect of loading level on *in vivo* response [46].

3.4.4 Boron/Borate

Boron is recognised as an ultra-trace mineral and is thought to play a regulatory role on other elements such as Calcium and hence a role in bone metabolism [101]. Boron has in fact been linked with preventing calcium loss and bone demineralisation in post-menopausal women [102] and boron supplementation has been shown to reduce the effects of vitamin D deficiency in chicks [103]. Boron also clearly effects bone regulating hormones involved in bone growth and bone turnover [104].

Boron inclusion in bioglass has been shown to improve the proliferation and expression of Col1 and Runx2 of osteoblasts [105]. Boron is shown to inhibit the proliferation of cells at high local concentrations in the short term (24 h [106]); however this effect is seen to be reversed over a longer time period (72+ h [107]). Significant increases in number of mineralisation nodules, expression of Col 1, OCN, BMP-4, -6 and -7 were reported with B concentrations ranging from 1 ng/mL – 100 ng/mL [107].

The majority of work with B containing biomaterials has focused on bioglass adaptation [108] with an inclusion of 2 wt% boron oxide demonstrating a significant increase in neoformed bone tissue surrounding the modified bioglass than the 45S5 control. Boron substitution into HA has been reported as early as 2002 [109]. Incorporating Borate into the HA lattice can be achieved by several methods. Common routes in the literature are via solid state synthesis with the borate supplied as B_2O_3 [110] or as a wet chemistry precipitation with the borate supplied either as Boric Acid (H_3BO_3) [109] or as Tributyl Borate (Bu_3B) [105]. All of the mentioned methods deliver acceptable yields.

Borate substitution into hydroxyapatite is relatively easy due, in no small part, to the different species of borate ion that are possible. Within the hydroxyapatite crystal, it is theoretically possible for borate to be present as either BO_4^{5-}, BO_3^{3-}, or BO_2^{-} [109] [111] [112]. These different species of borate can occupy either a phosphate or hydroxyl site, depending on their size and charge. BO_4^{5-} can only substitute for PO_4^{3-} due to its tetrahedral shape meaning the phosphate site is the only location large enough to fit it, however this substitution carries a mis-balance of charge with the borate contributing an additional 2 electrons to the lattice. Additionally the tetrahedral form of borate is rarely reported in the literature, and is typically associated with borate glasses where it has two bridging oxygens which helps to reduce the total charge of the ion (from 5- to 3-) [111] [112]. Such a charge imbalance must be accounted for either by the loss of hydroxyl or by the co-substitution of another species (see charge balancing of silicate substitution above in section 3.4.3). BO_2^{-} forms a linear species that replaces the

hydroxyl group, leading to steric stresses on the lattice due to the much increased volume occupancy of the borate group over the hydroxyl, although there is no charge balancing required. The most complex species of borate for substitution is the $BO_3{}^{3-}$ form. $BO_3{}^{3-}$ is a trigonal planar species, with the same charge as the phosphate group. Due to its equivalent charge, it can readily substitute into the phosphate site without upsetting the electronic balance within the unit cell, however due to it lacking an additional oxygen and a tetrahedral shape it contributes to an instability in the Ca-ion channel. It is also isoelectronic with carbonate ($CO_3{}^{2-}$), and as such can also substitute for the hydroxyl group in the same way as carbonate does. It is this duality of substitution that makes for determination of its location difficult. All told, there are 4 possible substituted forms of borate, two of which are the same species, but in two different sites making discrimination between them challenging.

3.4.5 Sulphur/Sulphate

Sulphate is already a widely employed in biomaterials in the form of Calcium Sulphate ($CaSO_4$) which presents as a fast setting, rapidly resorbed Calcium cement. Historically Calcium Sulphate has been employed for nearly a century [113]. Even with its extensive history and regular clinical use, the method of activity for $CaSO_4$ is incompletely understood [114]. Sulphate substituted hydroxyapatite (S-HA) has recently been reported [115], however the paper does not detail any biological testing.

The synthesis method is a microwave assisted solvo-thermal process that produces relatively crystalline material without the need for firing, however this is still low crystallinity compared to wet chemical precipitation and firing under correct conditions. The paper is useful for showing that materials produced in this thesis are possible to synthesis by another method, but there is no added information on thermal stability of bioactivity.

3.5 Foaming

There are a wide range of possible routes for producing ceramic foams. Traditional methods such as gel casting, starch consolidation, sacrificial foam casting, and direct foaming are common [116]. More recently, freezing techniques for the generation of porous structures have been developed with freeze-casting and freeze drying being widely used [117]. A comprehensive review of different foaming methods has been carried out by Studert

et al. [118]. The subject of foaming is incredibly broad, and as such the following literature review focuses on the direct foaming method, and what controls the features seen there as direct foaming is the method used in this thesis.

3.5.1 Direct Foaming

Direct foaming of a HA powder into a porous, fully-inorganic scaffold involves processing the primary powder through 3 distinct phases as outlined in figure 3.3

Phase one consists of mixing the slurry and generating a foam – typically through the mechanical inclusion of air. At this point, solid-liquid, solid-gas, and liquid-gas interactions dictate the formation of a foam, and the stability of that foam.

After the wet forming of the foam a green body needs to be formed by the drying of the foamed slurry – this is phase 2. At this point the act of driving off the majority of the solvent causes necking and interconnections between the larger bubbles – thereby forming strut pores. Additionally the level of flocculation at foaming can be seen in the density of the struts as solvent channels are dried out and open up. When well dried the foam is in its 'green' form.

The final phase is to fire the green foam to burn out any organic surfactant that remains and to consolidate the ceramic structure into a single fused inorganic piece.

3.5.2 Phase 1 - Wet Processing

Mechanical Bubble Formation

When considering the process of mechanically foaming a slurry the most obvious point to start is the mechanical process of introducing bubbles.

Bubble formation via shear mixing is a common process that is well understood in the literature. It is possible to calculate the shear stress required to rupture a deformed bubble into a series of smaller bubbles by using Taylor's model. Taylor's model states that when a spherical droplet of radius R_0 with a viscosity of η_d is dispersed in a fluid with a viscosity of η_c, the droplets will deform into an elongated cylinder. Typically rupture of these cylinders takes place due to Rayleigh's instability in order to reduce the higher surface energy caused by the elongation of the sphere. Deformation only takes place when the shear stress ($\eta_c\gamma$) surpasses the interfacial stress,

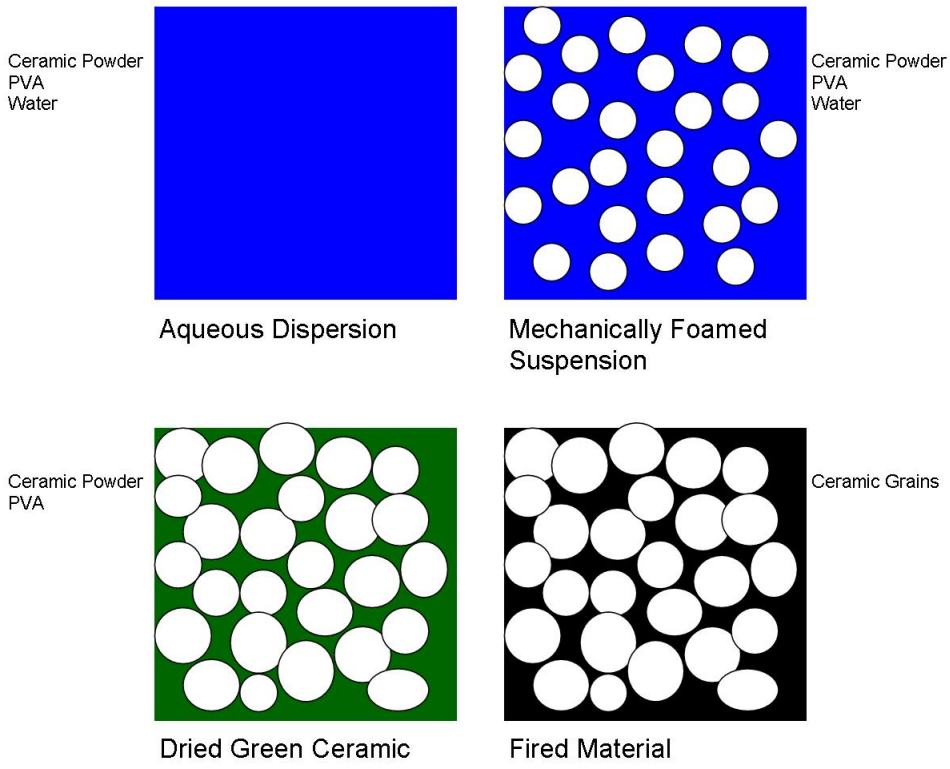


FIGURE 3.3: Schematic showing the various stages in foam formation and consolidation. The initial suspension (top left) is mechanically foamed to produce a porous wet form (top right). This is then dried to remove water and leave a 'green' form (note – colours are not representative). During the process of drying, volume is lost from the slurry as water evaporates causing bubble growth and if the struts are thin enough – interconnections. Finally the green body is fired to sinter the ceramic powder and burn out the organic (PVA).

where γ is the shear rate and σ is the interfacial tension. The ratio of these two values is the capillary number (Ca), which when exceeding a critical value (Ca_{crit}) the elongated droplet will split into smaller droplets with an average radius of R, as calculated from the below equation (equation 3.1).

$$R \propto Ca_{crit}\frac{\sigma}{\eta_e \gamma} \tag{3.1}$$

The implications of this are complex in the process being investigated, but the key point to consider from this is that the viscosity of the suspension is key in determining the size of the bubbles that go onto form the primary macro pores – and as such any surfactant, thickening agent, or particle effects will directly affect the pore size. It is reasonable to expect that, at 40 wt.% loading, the particle properties will greatly affect the viscosity encountered during shear mixing. As can be seen from the above equations, the bubble size decreases as viscosity increases, hence there should be a difference between main pore sizes associated with difference in viscosities. If the systems being run all maintain the same solid loading level, then the viscosity changes can be influenced from particle size and zeta potential.

Bubble Stability

Once the bubbles have been formed through the above mechanical process, there are 3 distinct modes of possible failure that need to be accounted for. Depending on measures taken to resist these mechanisms, foam lifetimes can be measured in seconds up to days whilst wet. A foam stability of hours is ideal so that drying can occur to set the foam into a green form.

The underlying cause for foam destabilisation is the high liquid-gas interface area which is inherently thermodynamically unstable. The 3 physical manifestations of this instability are drainage (also referred to as 'creaming'), coalescence ('film rupture'), and Ostwald ripening.

The process of drainage is the physical separation of the two phases in the foam due to gravity/density. During drainage the lower density bubbles rise to the top to form a segregated mixture of bubbles sitting on top of a continuous liquid phase. This dense foam layer is characterised by polyhedral cells separated by thin films (lamellar) of the liquid of the continuous phase, with Plateau borders at the intersection of 3 bubbles. The process of bubbles rising to the top of the foam is governed by Stoke's Law (equation 3.2):

$$\upsilon = \frac{2}{9}\frac{(\rho_p - \rho_f)}{\mu} g R^2 \tag{3.2}$$

Where:

v = Terminal velocity

ρ_p = Density of the particle (or gas bubble)

ρ_f = Density of the fluid/suspension

μ = Viscosity

g = Acceleration due to gravity

R = Radius of particle/bubble

As can be deduced from this equation, the primary factors that retard drainage are a higher viscosity of the fluid phase, a smaller bubble diameter (which is also reduced by a higher viscosity as discussed earlier), and a lower density of the fluid phase. In a PVA/HA slurry, the viscosity is kept high, hence slowing drainage significantly and reducing the bubble size, however this also increases the density. With the increased density being fixed, obviously the best practice is to increase the viscosity of the slurry – a process that can be done by decreasing the zeta potential.

Coalescence is when the thin lamellar between the bubbles as a result of drainage are not stable enough to keep the adjacent cells apart, resulting in film collapsing and the two bubbles joining into one single bubble. The physical process effecting coalescence is the attraction and repulsion of the bubbles – primarily a result of van der Waals attraction and electrostatic repulsion as detailed in figure 3.4. Van der Walls is a consistent force that cannot be readily modified, and so the only way to combat coalescence is by increasing the repulsive forces between the bubbles – typically done by utilizing a surfactant at the liquid-gas interface. This surfactant layer causes a repulsive force between the two interfaces that allows the stabilisation of the fluid between. As will be covered later – this surfactant layer does not have to necessarily be a polar surfactant molecular but can also be a particulate layer via a Pickering emulsion.

The final process is Ostwald ripening. This is the diffusion of gas and subsequent disproportionation of bubbles. The physical process is a result of the Laplace pressure inside each bubble – a pressure caused by the curvature of the liquid-air interface. For spherical bubbles of radius R and interfacial energy γ, the Laplace pressure (ΔP) is given by $2\gamma/R$ [119]. The different radii in separate bubbles lead to a difference in pressure, and therefore a flow of molecules from high pressure to low pressure systems. Using the above equation, it is clear that the pressure is inversely proportional to the radius, and thus small bubbles tend to become smaller, whilst large bubbles tend to become larger. This process can be slowed by the adsorption of

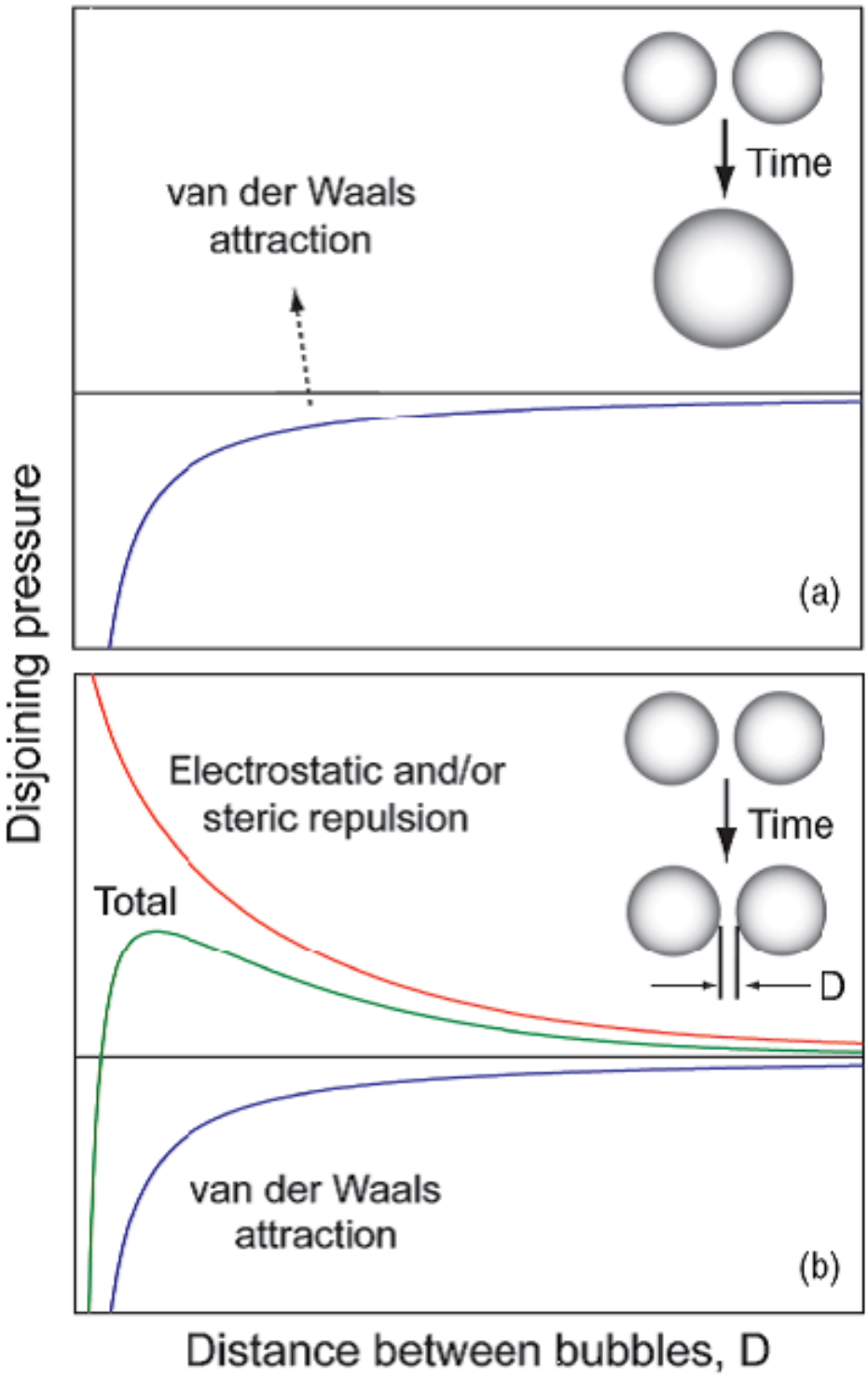


FIGURE 3.4: Force versus distance graphs demonstrating how van der Waals (vdw) attraction can be overcome by electrostatic repulsion [118]. Vdw is a typically short range, relatively weak force, hence ionic surfactants can provide sufficient electrostatic repulsion.

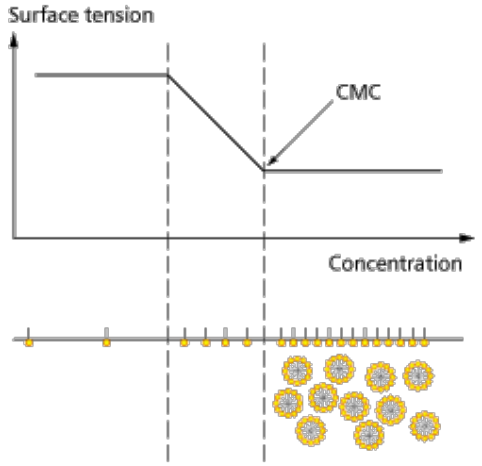


FIGURE 3.5: Graphic demonstrating the build up of surfactant prior to formation of micelles in a water/air/surfactant mix. Graphic taken from RSC article: 'Ink Chemistry' [121]

surfactant molecules which lower the interfacial energy, and therefore the pressure differences. Also, as the rate of diffusion is related to the difference in radii between bubbles, creating a monodisperse size of bubbles is beneficial. Shear mixing, as detailed previously, creates a tight dispersion of bubble sizes related to the shear rate and suspension viscosity.

Surfactants and Pickering Emulsions

As described above, the key to stopping 2 of the 3 modes of failure for a foam is to stabilise and secure the liquid-gas interface to ensure that coalescence and gas diffusion is limited. The liquid-gas interface is typically stabilised by the use of surfactants. Surfactants are chemical species that consist of 2 halves where one half has an affinity for the liquid phase, and the other end has an affinity for the gaseous phase (or a repulsion from the liquid). These species are thermodynamically stable when they can form along a surface interface, thereby allowing the hydrophobic (or lyophobic in an organic/oil liquid) end to be excluded from the water. Once the concentration passes a critical value – namely where the surface is completely covered – the surfactant molecules will form micelles, or along the interfaces with bubbles [120].

Typical surfactants (such as Dispex, Sodium Stearate, Sodium Lauryl Sulphate) are single molecules that can be added easily, however it is also possible for a solid powder to act as a surfactant and form Pickering emulsions – a process that has been used for decades in floatation technology and similar [122]. Pickering emulsions are caused when it is energetically favourable to replace the liquid-gas interface with a solid-gas interface. The

degree of immersion of the particle within the liquid phase is determined by the balance of liquid-gas, solid-liquid, and solid-gas energetics. A simple description of the particle position is related to the contact angle of the solid-liquid interface. The particle will sit immersed to a point where the surface will experience a contact angle with the liquid that is the same as would be seen by placing a droplet of the liquid onto a flat surface of the solid.

As the solids stabilise the system by replacing part of the liquid-gas interface with a solid-gas interface, it is possible to calculate the energy gained (G) using 1 of 2 simple equations (shown in equation 3.3). The following equations use the contact angle (Θ), particle radius (r), and the liquid-gas interfacial tension (γ_{LG}). The first equation is for hydrophilic particles that have a contact angle of <90° (and therefore sit mainly within the liquid), whilst the second is for hydrophobic particles which have a contact angle of >90° (and therefore sit mainly within the gas). Obviously the terminology can be changed for lyophilic and lyophobic particles when considering a non-polar liquid.

$$\begin{aligned} G &= \pi r^2 \gamma_{LG}(1 - \cos\Theta)^2 \\ G &= \pi r^2 \gamma_{LG}(1 + \cos\Theta)^2 \end{aligned} \tag{3.3}$$

3.5.3 Phase 2 - Drying

After the foam is produced in the wet state, the ceramic slurry needs drying out to lock in the structure. Drying also produces a range of features that may be important in the final product. When considering a PVA and ceramic slurry, the main features that are generated whilst drying are wall density and strut porosity.

Wall Density

As the water is driven off from the foam, the slurry that made up the walls densifies into powder particles held together by dried PVA. The process of drying causes a contraction of the films (thin sections of wet walls between bubbles) and so the struts have variable density dependent on the level of moisture content. During the foaming phase the particle electrokinetic (zeta) potential determine the level of flocculation of the system. Initially this is important as a more flocculated system (as caused by a low zeta potential) has a higher viscosity which will affect the shear bubble formation and the draining of the foam, additionally flocculation leads to poor packing of particles during drying which causes the pore walls to be less dense

in the green state leading to greater shrinkage on firing. This initial lower density will be evidenced in the level of strut porosity formed as well as channels left by moisture retreat.

Strut porosity is the pores formed between the primary pores that were created in the wet processing stage. These pores tend to be in the $10 - 50\,\mu m$ range and are typically round. As the wall dries and densify, it thins before osmotic pressure pulls the centre too thin and causes a pore to form that is opened until the water has been fully removed.

3.5.4 Phase 3 - Firing

Once the green foam has been fully dried, the sample needs firing to attain its final structure. When firing two main processes occur – firstly any organic content (PVA in this case) is burnt out, which leaves a residual porosity, and secondly the ceramic particles sinter and densify. Organic burnout occurs <600 °C whilst solid state sintering in HA occurs >1000 °C. The level of burn-out porosity is dependent on the PVA loading during the foaming process and its association to the particulate – for example if the PVA bound the powder efficiently it could be found spread evenly throughout the green body, whereas if the PVA did not efficiently associate to the powder, it may be concentrated on the surfaces which would dramatically change the burn-out porosity structure. In this scenario, the powders are all similar, and the PVA loading was fixed, hence it is reasonable to assume a consistent porosity structure from PVA burn out across samples, rather than varied burn out features across samples.

After the burn out, the individual ceramic grains will begin to see solid state diffusion and crystal re-arrangement. During sintering a process of mass transport (solid-state diffusion) can lead to large shrinkage – up to 30% based on sample observations. This shrinkage occurs on a small scale, and can be responsible for porosity forming between grains as re-arrangement occurs. Ultimately when fully sintered the ceramic should present a fully dense surface, but until that point it is plausible for the surface to demonstrate a sub-micron scale porosity. The materials in question potentially have variable shrinkages due to sintering as well as differing temperatures required to see sintering occur – for example Bianco et al. demonstrated that Silicate substitution lead to greater total shrinkage at 1100 °C than pure HA [123]. As such, this variation could be significant when comparing the final products.

3.6 Background Theory

3.6.1 Ca:P Ratio

HA is formed when the Calcium:Phosphate (Ca:P) ration is equal to 1.667. There is a small level of give in this ratio due to the incorporation of carbonate ($CO_3{}^{2-}$) from atmospheric carbon as a substitution for phosphate ($PO_4{}^{3-}$). Information on typical levels encountered is sparse but, from internal work at Lucideon, values of 0.5 wt.% (determined by weight loss on ignition for XRF) are fairly standard. This substitution can occur at precipitation, or during firing and whilst it is avoidable, the process steps required to do so are prohibitive as it would involve having to perform the entire precipitation under a none carbonate containing atmosphere (either vacuum or nitrogen for example, and then fire without carbon dioxide being present). The technical requirements to remove the chance of carbonate inclusion are extreme, especially when considering the low level typically encountered. It is not considered a problem, indeed certain groups are working to increase the level and specificity of carbonate substitution [124, 125, 126, 127], typical human bone will contain between 1 wt.% - 3.2 wt.% carbonate [128]. Values of up to 7.5 wt.% CO_3 inclusion have been reported [129].

In the scenario where Ca:P >1.667 there are two outcomes:

a) The HA phase could still form, whilst maintaining a slight phosphate deficiency. Depending on how structured and regular the deficiency is, this can be found on its XRD trace as either a change in d-spacings, or contain an 'amorphous' content – even though the material is still fully a HA crystal. Whether it is presented as crystalline variation (and therefore a d-spacing shift) or amorphous content is dependent on whether the deficiency shows long range order as a regular defect, or lacks long range order as an irregular defect. It is important here to define what amorphous material constitutes in the term used here. Amorphous material refers to any solid structure that lacks long range order. This is typically seen in glasses and glassy materials, with the crystalline materials featuring long range order (a unit cell), such as a ceramic or crystalline polymer. These rather crude definitions work for the wide range of theory required in interpreting materials, but begin to fall down when faced with real world scenarios. In many crystals, defects can be found – either a substitution or void, along with growth defects (such as grain boundaries and line defects). These defects introduce an element of disorder into the long range structure of an otherwise crystalline material in a fashion which is clearly distinct to glassy secondary phase. As such it is important to remember the difference between an amorphous and crystalline material are not limited to a complete segregation of two distinct phases, but rather a continuum between a perfect crystal form, and a perfectly amorphous form.

b) Past the range that is possible to remain a single phase HA structure, secondary phases occur. Two examples are OctaCalcium Phosphate (OCP) and Lime (CaO). Within the regular experimental bounds operated at Lucideon (weighing accurate to 4 significant figures to aim for a Ca:P of 1.67), Lime is the common contaminant. When lime is present, it is still very possible to generate highly crystalline HA as the excess Ca is readily incorporated into CaO. This can cause the material to show signs of cytotoxicity, due to its high pH and ease of dissolution, if not removed, but is easy to extract with a simple chemical wash (Such as NH_4Cl).

When the Ca:P ratio is <1.667 the options remain similar. The HA can still form crystalline, but Ca-deficient, HA. As with a phosphate deficiency this can expose itself in an XRD trace as either crystalline material with altered d-spacings (i.e. when the defect is regular and repeated), or the defect can lack long range order, thereby presenting as amorphous content. The next possibility, is the generation of a secondary phase. With a Ca:P ratio between 1.5-1.667, the secondary phase most likely to form is TriCalcium

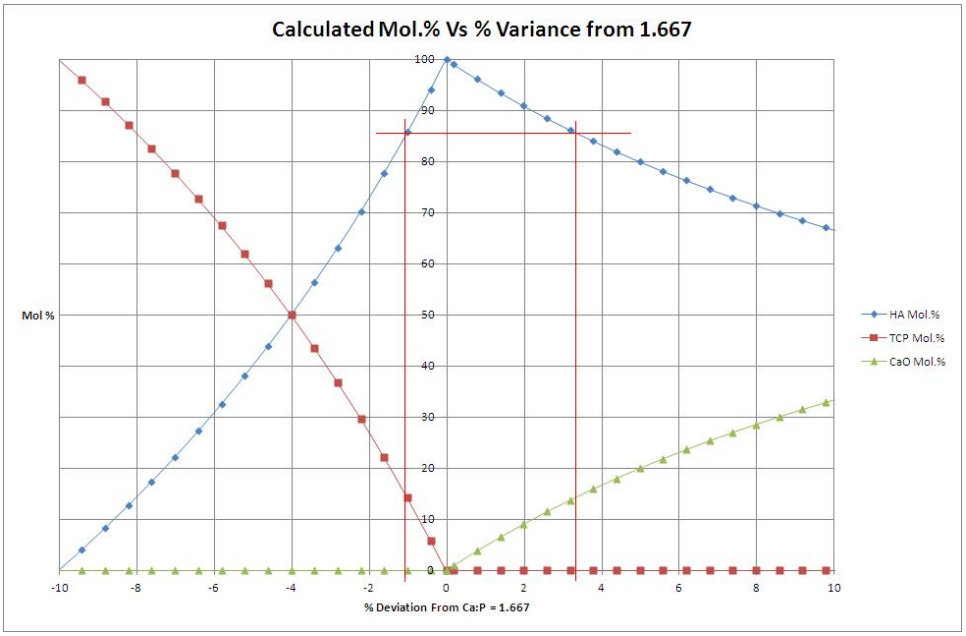


FIGURE 3.6: Theoretical Mol % of HA, TCP and CaO as a product of variation from Ca:P = 1.667. Horizontal red line is aprx 85% yield, with the vertical lines demonstrating the variation required. Notably, to fall below 85% yield a difference between 1% and -3.25% is required.

Phosphate (TCP),and more often the beta form as it is the low temperature (<1400 °C) stable phase. Unlike with the evolution of CaO, the formation of a biphasic system such as HA/TCP, there can be a significant amount of defect from both phases, as well as interface boundaries. These defects and interfaces present themselves as amorphous content. These various phases and their theoretical ratios relative to Ca:P ratio are shown in figure 3.6.

The amorphous content, as described from an XRD trace can be considered in a number of ways. In its truest form, amorphous content is material which is non-crystalline – meaning it lacks long range order. The most typical form of amorphous material encountered is glassy materials which have a short range order (i.e. are solid), but no repeating pattern. However, there are three other causes of amorphous content that are important to consider when viewing HA data. Firstly, any defect which is not repeated in a regular fashion (i.e. every 3rd atom is missing being a crystalline defect, but 1 in three atoms missing without any pattern being an amorphous defect) will cause peak widening, and hence be reported as amorphous content. Related to this, any crystal growth defect which is not repeated in a regular fashion (i.e. a screw-turn or an offset step growth) will also cause peak broadening. The final cause of amorphous content is from material which intrinsically lacks long range order. The edge of a crystal by definition lacks long range order. This can be a significant cause of peak broadening and

amorphous content in samples with nano-features, but also samples with secondary phases propagating throughout [130].

Beyond the ideal scenarios of a precipitation reaction which is fired to define the crystalline phases, there is also the risk of material degrading at high temperatures. In pure HA this can occur from 1200 – 1400 °C. At these temperatures, it is possible for the HA crystal ($Ca_5(PO)_3OH$) to degrade to TeTra Calcium Phosphate (TTCP) and α-TriCalcium Phosphate (α-TCP) [131]. On cooling this converts to Lime and β-TCP This is also often accompanied by a large amount of amorphous content generation.

To add to the complexity of a system which exists as a continuum, substituting materials can change the energetics dramatically, effecting the stability of the alpha form of TCP, changing the thermal stability of HA, adding amorphous content by not consistently substituting into the same site.

3.7 Hydroxyapatite Synthesis

Due to HA being the inorganic phase in hard tissues, significant research has been put into utilising HA in medical implants in order to recruit the body into the repair or fixation process. Originally, biologically sourced HA was used (i.e. calcined bovine HA) – partly because it was already in wide use for the preparation of bone china and therefore was a well studied material source. As methods and markets developed however, a controlled source of HA with little to no batch-to-batch variation became increasingly valuable in order to meet both demand and regulatory controls. One of the first papers to apply synthetic HA for forming into useful shapes was Levitt *et al.* (1969) with coated devices following shortly [132].

Since 1969, literally thousands of papers have been published regarding the preparation of HA in different shapes, sizes, chemistries, and crystallinity. Out of these papers and research several generic methods for the production of HA have come through and this section will look at some of the more widely adopted methods and compare them.

The basic equation being completed by all of these reactions is:

$$5Ca^{2+} + 3PO_4^{3-} + OH^- \rightarrow Ca_5(PO_4)_3OH$$

3.7.1 Wet Chemical Precipitation

Wet chemical precipitation methods are one of the most widely used approaches due to the relatively mild and simple reaction conditions. In this

method, as a generalisation, a suspended/soluble Ca source is intimately mixed with a soluble/suspended PO_4 source under the correct stoichiometry. This produces (based on the authors observations) a precipitate that shows a relatively low crystallinity (40-60% at point of precipitation), a small particle size (generally $5 - 200\,\mathrm{nm}$), and typically a rod or needle type structure. Due to the nature of the chemistry that is occurring when this process is carried out and possible side reactions, this synthesis method should not be considered trivial.

In the most generalised bench reaction, H_3PO_4 is titrated into a stirring mixture of $Ca(OH)_2$, optionally with pH control in the form of titrating NH_4OH alongside. This addition leads to formation of a solution that is supersaturated with respect to HA, leading to the nucleation and crystallisation of HA particles. Due to the rapid precipitation, the order of crystallinity is relatively low, and two main options for consolidation exist – either by aging the suspension at a higher temperature (70-80 °C often, although higher is possible) leading to larger, more crystalline particles (up to 85% crystalline). The other option that is most often used, common at an industrial level, is to put the powder through a high temperature calcination phase that is run between 1100 – 1400 °C [133].

Beyond this level of simple precipitation, various other steps can be included to alter the process and deliver a different material. For instance, changing the Ca or PO_4 source will result in a differing HA morphology, the addition of surfactant can cause the particles produced to take on shapes not possible at that scale by any other method [134], pH and temperature both have significant effects on the particle size and morphology [135, 136, 137]. This level of adaptability is one of the reasons for the popularity of wet chemistry precipitation preparation methods as it opens up a large amount of novel avenues for exploration with the potential to offer significant biological benefits due to topographical alterations rather than chemical.

3.7.2 Hydro/Solvo Thermal

Solvo-thermal (hydro-thermal is the same process, but with water as the solvent) is a method whereby the solvent is heated in a sealed/pressurised vessel. The benefit of using a pressurised vessel is that the temperature of the solvent can be taken above its boiling point. The change in reactant and solvent properties at these elevated temperatures allow greater control of some experimental variables.

Solvo-thermal methods offer some 'green' benefits that are of interest to larger commercial entities, in addition to some unique processing capabilities. Comparable to solid state synthesis, or the calcination step in wet

chemistry precipitation, this process typically requires lower temperatures and still can deliver highly crystalline HA particles via a one-step process [138, 139]. This is also of interest as there is no grain or particle growth from a calcination step allowing highly crystalline, yet still relatively fine powders to be produced opening up novel processing techniques that can take advantage of the smaller primary particle size. One significant downside to this process is that it's typically a batch process rather than continuous that can limit commercialisation, thermal lag being one of the biggest issues [140].

3.7.3 Solid State

This method involves the mixing of raw materials in a powder form, before a high temperature step that allows solid state diffusion of ions leading to particle nucleation and subsequent grain growth. The standard reaction schematic is that the raw materials are milled together in a slurry for an extensive period of time to ensure homogeneity, before they are then pressed and heated. The heating step often requires temperatures >1200 °C, and may be performed by way of Hot Isostatic Pressing to ensure a high pressure. It is often recommended that after this process has completed, milling and refiring of the sample be conducted to ensure completion [141].

This process requires a significant amount of energy and is open to secondary phases forming where the local concentration of Ca:P is imbalanced. Once a secondary phase forms (often β-TriCalcium Phosphate) [142], it is rarely possible to heat treat and remove the contaminant. The incorporation of secondary phases, when not targeted and controlled, opens up the finished material to unpredictable performance characteristics.

3.7.4 Combustion Synthesis

Several groups are working on the production of powdered HA from combustion reactions. The reaction often takes place at the nozzle of a burner where the Ca source meets the PO_4 source with one containing a fuel source (i.e. citric acid, sucrose, urea etc) and the other containing an oxidising agent (i.e. nitric acid [143], hydrogen peroxide [144]). When the two streams are mixed and ignited, it rapidly creates a large amount of small particulates that are accelerated downstream. This process has obvious applications for on site preparation and coating of HA to a target from a modified High Velocity Oxy-Fuel (HVOF) coating system [145]. The system is very easily adapted to incorporated substitutions into the produced material; however

a lack of control over reaction times and pH does limit how easily a reaction can be controlled outside of the reactants present and in what ratio. Typically the HA produced by this route is very crystalline but with a comparatively large particle size compared to other processes.

3.7.5 Comparative Chart

Below is table 3.4 comparing the different routes with some of their key properties.

TABLE 3.4: Comparison of HA Synthesis Routes.

HA Synthesis Method	Method Description	Reaction Temperature (°C)	Particle Size (μm)	Scalability	Comments
Wet-chemical Precipitation	Calcium and phosphate solutions combined under controlled reaction parameters resulting in nucleation and crystal growth	Room temperature – 85	> 0.1 (significantly lower if using emulsion technology)	High	Most common method. Three step procedure; requires calcinations and sintering after processing. Potential difficulties with reproducibility due to lack of precise control.
Hydro- and Solvo-thermal	Reaction takes place in aqueous solution in a closed system under conditions of high temperature and pressure	150 – 400	> 0.05	Low	Homogeneous crystal shapes and sizes [146, 147]. Single step process to form crystallised HA [148, 149]. Particle morphology can be controlled, but process parameters may be costly [150, 151].

HA Synthesis Method	Method Description	Reaction Temperature (°C)	Particle Size (μm)	Scalability	Comments
Solid State Reactions	HA formed via solid-state diffusion of ions from solid reactants. Requires thermal treatment to initiate reaction	1050 - 1250	> 2.0	Medium	Most traditional method. Involves long ball milling, drying, compression, and sintering steps. May need to repeat process steps to improve quality and reduce particle size. Slow and difficult to achieve a complete reaction; mixed phase product [152, 153].
Combustion Synthesis	Particles formed from solution via spontaneous combustion of a fuel and oxidiser at elevated temperatures	170 – 500	> 0.45	Expected to be low	Reaction time <20mins. Uncontrolled high temperature reaction front may lead to mixed phases. Particle morphology dependent on fuel used.

4 Experimental

4.1 Introduction

In this chapter; the materials and their synthesis are detailed in section 4.3, characterisation techniques in section section 4.4 while the *in vitro* biological testing methodology is covered in the final section, section 4.5

4.2 Co-Worker Contributions

This thesis is the culmination of several years effort within a commercial organisation, and remote from the physical location of the University labs. As such, generation of all the data contained within has only been possible with the much appreciated assistance of several colleagues. This section is specifically to highlight all those who have helped with each technique.

Several techniques were run at Lucideon under the request of the author, but were operated by key staff. The author has run each technique independantly, but for various reasons has had to rely on colleagues during his time there. the following techniques were run by colleagues and the data presented here is a mix of data generated by other researchers, and the author. All interpretation is the authors own.

- X-Ray Diffraction by Dr. Giles Blundred
- X-Ray Fluorescence by Sharon Mansfield
- Ion Coupled Plasma - Optical Emission Spectroscopy by George Jones
- Fourier Transformed Infra Red spectroscopy by Malcom Rose
- Mercury Intrusion and Nitrogen Adsorption by Lee Bullock
- Scanning Electron Microscopy by Alan Neale
- Particular credit goes to Matthew Cantelo for his assistance in the synthesis especially, and on the Malvern Mastersizer
- Additional thanks go to the whole technical support team at Lucideon who keep the labs and equipment running

Due to the distance and part-time nature of the PhD, although all cell culture techniques and assays were run by the author initially key repeat assays of the Mx-HA material were repeated by two Master's candidates. The author would like to thank Katherine Bostock and Zheng Zhiqiang for their contribution to help wrap up the project.

4.3 Sample Preparation

Below is detailed all the experimental methods and materials sourcing for producing all samples discussed in this thesis.

4.3.1 Materials Sourcing

All materials were ordered from Sigma Aldrich, and used as received. The two exceptions are the 6M Phosphoric acid which is received as a 85 wt.% solution, and subsequently diluted to 6M with the exact concentration determined by titration with 1M NaOH (Fixanal), also the PVA is sourced from Nippon Gohsei, Osaka, and is grade EG-05.

4.3.2 Powder Synthesis

The reagent values for the synthesis of all experiments covered in this thesis is presented as a single table with associated labeling nomenclature in table 4.3

HA Synthesis

Calcium Hydroxide was suspended in Water (700 mL) in a 1L jacketed reactor. The reactor consists of a jacketed vessel hooked up to a circulator to regulate temperature. Reagents are added in through a port in the top, and the final product collected via the bottom outlet valve. Titration is carried out by an automated syringe pump as a rate of 4 mL/min discharge, and 20 mL/min fill. The entire kit used is marketed under the 'Atlas' brand (Sirrus, UK). The resulting mixture was stirred thoroughly (250 rpm) whist being heated until a stable temperature of 50 °C was maintained ($\pm$0.1 °C). Once the temperature was stabilised, 6M Phosphoric Acid was automatically titrated. As Phosphoric Acid addition began, the stirrer was ramped up to 350 rpm over 10 min.

The reagents were maintained in a theoretical ratio of cation:anion of 1.667. Typical $Ca(OH)_2$ mol values ranged from 1.3935 - 1.9983 depending on the mass of HA desired from the precipitation.

An example synthesis for the production of stoichiometric HA is thus; Calcium Hydroxide (103.25 g, 1.3935 mol), is suspended in Water (700 mL). The mixture is heated to 50 °C. At temperature, 6M Phosphoric Acid (139.35 mL, 0.8361 mol) is added from a syringe pump at 4 mL/min discharge, and 20 mL/min fill. This reaction produces ∼140 g HA in ∼1L water.

Mx-HA Synthesis

The above synthesis can be easily adapted to allow substitution to occur. The mol. % substitution is calculated by adding the moles of Ca and moles of phosphate to give a 100% value. This is then used to calculate the amount of substitution to add at a 1:1 replacement for the ion being replaced.

Ca^{2+} replacements are added at the same time as the Ca source, whilst ${PO_4}^{3-}$ replacements are added in full at the beginning of the H_3PO_4 titration. Table 4.1 shows which precursors are used for each substitution, and what each substitution replaces.

An example of a substituted HA synthesis (Si-HA), and how to calculate the percentage substitution is included here. Calcium Hydroxide (103.25 g, 1.3935 mol), is suspended in Water (700 mL). The mixture is heated to 50 °C. At temperature, TetraEthylOrthoSilicate (TEOS, 8.96 mL, 0.0382 mol) is added manually via syringe and 6M Phosphoric Acid (133 mL, 0.7980 mol) is added from a syringe pump at 4 mL/min discharge, and 20 mL/min fill. This reaction produces ∼140 g Si-HA in ∼1L water. The total substitution level is calculated as:

$$\frac{\text{moles of substitution}(0.0382)}{\text{moles of all reactants}(1.3935 + 0.7980 + 0.0382)} = \frac{0.0382}{2.2297} = 1.71\% \quad (4.1)$$

In the above example, the substitution level of Si is calculated as 1.71 mol.% or 2.5 wt.%. Another common format for detailing substitutions is to write them in the form of:

$$Ca_{10}(PO_4)_{6-x}(SiO_4)_x(OH)_2 \text{ , where x = 0.274} \quad (4.2)$$

TABLE 4.1: Table detailing which ions are substituted and the precursors used for synthesis

Substitution	Replaces	Source
Sr^{2+}	Ca^{2+}	$Sr(OH)_2.8H_2O$
${BO_3}^{3-}$	${PO_4}^{3-}$	H_3BO_3 - powder
${SO_4}^{2-}$	${PO_4}^{3-}$	3M H_2SO_4
${SiO_4}^{4-}$	${PO_4}^{3-}$	TetraEthylOrthoSilicate (TEOS)

TABLE 4.2: List of alternative Ca-precursors for investigating the Ca source and its effect on the synthesis of HA

Name	Formula
Calcium Hydroxide	$Ca(OH)_2$
Calcium Nitrate	$Ca(NO_3)_2$
Calcium Chloride	$CaCl_2$
Calcium Carbonate	$Ca(CO_3)_2$
Calcium Citrate	$Ca_3(C_6H_5O_7)_2$

Ca-source Variation

To vary the Ca-source, the reaction preparation is the same, but $Ca(OH)_2$ is replaced for the appropriate alternative source. Table 4.2 shows which various calcium precursors were used, and their chemical formula.

Di-Substituted HA

The substitutions under investigation were Si, S, B, and Sr using the method outlined above. Additionally, baselines of pure (undoped) HA, and 1.8 mol. % (0.8 wt. %) Si-HA (to act as an Actifuse analogue) were prepared. All substitution levels were fixed at 2 mol. % of each substitution (thereby generating a 4 mol. % total substitution). Two substitutions were carried out by a technician under instruction (Matthew Cantelo prepared Si,B-HA and Si,S-HA). Sr,Si-HA was repeated by the author due to some concerns over reagent purity leading to sample Sr,Si-HA r.r. (r.r. standing for re-run in this instance).

The specific substitutions under investigation were as follows:

- Sr,Si-HA
- Sr,S-HA
- Sr,B-HA
- Si,S-HA

- Si,B-HA
- Sr,Si-HA r.r.
- S,B-HA

^{11}B-HA

Three ^{11}B doped samples were prepared along with a baseline HA material for Neutron Beam Diffraction analysis at ISIS. $H_3{}^{11}BO_3$ was used as the boron source to produce samples with 2.5, 5, and 10 mol.% substitution. Phosphate was substituted for borate by a 1:1 replacement of H_3PO_4 with $H_3{}^{11}BO_3$.

pH Control

Where pH control was used, the reaction is adjusted by the addition of $NH_4OH_{(aq)}$ whilst the H_3PO_4 was titrated.

4.3.3 Structure Consolidation

After precipitation, samples were dried overnight at 98 °C in an air oven. They were then milled in a TEMA mill and either fired as a powder or as a foam, see section 4.3.4 below, to consolidate the crystal structure. The conditions for firing as a powder were with a firing schedule thus: a ramp time of 6 h to 1120 °C with a 20 h soak. Variations to this schedule involve changing the max temperature to 600, 1000, 1100, and 1200 °C as detailed in the associated experimental sections.

TABLE 4.3: Full experimental values for synthesis of hydroxyapatites throughout the project.

Experiment	Calcium ($Ca(OH)_2$ unless stated)	Phosphorous (6M H_3PO_4)	Strontium ($Sr(OH)_2.8H_2O$)	Silicon (TEOS)	Sulphur (3M H_2SO_4)	Boron (H_3BO_3)	pH Control
Base-HA	148.06 g, 1.9983 mol	199.8 mL, 1.1988 mol					No
5%Sr-HA	136.197 g, 1.8382 mol	199.77 mL, 1.1986 mol	42.481 g, 0.1598 mol				No
2.5%Sr-HA	142.178 g, 1.9190 mol	199.83 mL, 1.1990 mol	21.1977 g, 0.0798 mol				No
3%B-HA	148.1024 g, 1.9989 mol	183.75 mL, 1.1025 mol				5.9712 g, 0.0966 mol	No
1.5%B-HA	148.0638 g, 1.9984 mol	191.77 mL, 1.1506 mol				2.9785 g, 0.0482 mol	No
3%S-HA	148.0883 g, 1.9987 mol	183.84 mL, 1.1031 mol			31.97 mL, 0.0959 mol		No

Experiment	Calcium ($Ca(OH)_2$ unless stated)	Phosphorous (6M H_3PO_4)	Strontium ($Sr(OH)_2.8H_2O$)	Silicon (TEOS)	Sulphur (3M H_2SO_4)	Boron (H_3BO_3)	pH Control
1.5%S-HA	148.2379 g, 2.0007 mol	192.04 mL, 1.1522 mol			15.99 mL, 0.0480 mol		No
$Ca(OH)_2$, natural pH	103.51 g, 1.3988 mol $Ca(OH)_2$	139.86 mL, 0.8392 mol					No
$Ca(NO_3)_2$ natural pH	229.53 g, 1.3988 mol $Ca(NO_3)_2$	139.86 mL, 0.8392 mol					No
$CaCO_3$ natural pH	140.01 g, 1.3988 mol $CaCO_3$	139.86 mL, 0.8392 mol					No
$CaCl_2$ natural pH	155.20 g, 1.3988 mol $CaCl_2$	139.86 mL, 0.8392 mol					No

Experiment	Calcium ($Ca(OH)_2$ unless stated)	Phosphorous (6M H_3PO_4)	Strontium ($Sr(OH)_2.8H_2O$)	Silicon (TEOS)	Sulphur (3M H_2SO_4)	Boron (H_3BO_3)	pH Control
Calcium Citrate natural pH	232.42 g, 1.3988 mol $Ca_3(C_6H_5O_7)_2$	139.86 mL, 0.8392 mol					No
$Ca(NO_3)_2$ pH 9	229.53 g, 1.3988 mol $Ca(NO_3)_2$	139.86 mL, 0.8392 mol					Yes
$CaCO_3$ pH 9	140.01 g, 1.3988 mol $CaCO_3$	139.86 mL, 0.8392 mol					Yes
$CaCl_2$ pH 9	155.20 g, 1.3988 mol $CaCl_2$	139.86 mL, 0.8392 mol					Yes
Calcium Citrate pH 9	232.42 g, 1.3988 mol $Ca_3(C_6H_5O_7)_2$	139.86 mL, 0.8392 mol					Yes

Experiment	Calcium ($Ca(OH)_2$ unless stated)	Phosphorous (6M H_3PO_4)	Strontium ($Sr(OH)_2.8H_2O$)	Silicon (TEOS)	Sulphur (3M H_2SO_4)	Boron (H_3BO_3)	pH Control
HA	103.25 g, 1.3935 mol	139.35 mL, 0.8361 mol					No
Si-HA	103.25 g, 1.3935 mol	133 mL, 0.7980 mol		8.964 mL, 0.03815 mol			No
Sr,Si-HA	99.95 g, 1.3511 mol	131.92 mL, 0.7937 mol	11.85 g, 0.04239 mol	9.96 mL, 0.04239 mol			No
Sr,S-HA	99.95 g, 1.3511 mol	131.92 mL, 0.7937 mol	11.85 g, 0.04239 mol		14.87 mL, 0.04239 mol		No
Sr,B-HA	99.95 g, 1.3511 mol	131.92 mL, 0.7937 mol	11.85 g, 0.04239 mol			2.7572 g, 0.04239 mol	No
Si,S-HA	103.25 g, 1.3935 mol	124.49 mL, 0.7513 mol		9.96 mL, 0.04239 mol	14.87 mL, 0.04239 mol		No
Si,B-HA	103.25 g, 1.3935 mol	124.49 mL, 0.7513 mol		9.96 mL, 0.04239 mol		2.7572 g, 0.04239 mol	No
Sr,Si-HA r.r.	99.95 g, 1.3511 mol	131.92 mL, 0.7937 mol	11.85 g, 0.04239 mol	9.96 mL, 0.04239 mol			No

Experiment	Calcium ($Ca(OH)_2$ unless stated)	Phosphorous (6M H_3PO_4)	Strontium ($Sr(OH)_2.8H_2O$)	Silicon (TEOS)	Sulphur (3M H_2SO_4)	Boron (H_3BO_3)	pH Control
S,B-HA	103.25 g, 1.3935 mol	124.49 mL, 0.7513 mol			14.87 mL, 0.04239 mol	2.7572 g, 0.04239 mol	No
2.5%^{11}B-HA	148.06 g, 1.9983 mol	186.38 mL, 1.1183 mol				4.9932 g (due to ^{11}B), 0.0805 mol	No
5%^{11}B-HA	148.06 g, 1.9983 mol	172.97 mL, 1.0378 mol				9.9868 g (due to ^{11}B), 0.1610 mol	No
10%^{11}B-HA	148.06 g, 1.9983 mol	146.13 mL, 0.8768 mol				19.9737 g (due to ^{11}B), 0.3220 mol	No

4.3.4 Foaming

Foaming Trials

Initially 6 foams were produced by varying, (i) PVA level and (ii) HA Powder.

Each powder was processed into one of 3 states:

a) As Precipitated – the powder was precipitated, dried and milled in a TEMA mill.

b) Calcined – the precipitated powder was taken and fired in a kiln at 600 °C for 20 h. The resultant material was milled in a TEMA mill.

c) Fired – the precipitated powder was taken and fired in a kiln at 1120 °C for 20 h. The resultant material was milled in a TEMA mill.

PVA was either kept at 5 wt.%, or 10 wt.%. The two variables (3 different states of the powder – fired, calcined, and as precipitated, and 2 different PVA loadings) produced 6 foams.

The specifics of the preparation method are as follows. Hydroxyapatite powder (60 g) was added to 90 mL of PVA solution (either 90 mL of 16.67 wt.% PVA solution, or 45 mL 16.67 wt.% PVA solution and 45 mL De-Ionised Water) to produce a mixture of 40 wt.% HA powder and either 10 wt.% or 5 wt.% PVA. The mixture was first mixed by spatula to ensure full wetting of HA powder, then mechanically whisked for 90 s before being poured into silicone trays for oven drying. The materials were then dried at 50 °C for 48 h before being further processed.

The next stage was to fire the samples at 1100 °C and 1200 °C with a 10 h dwell time. This finally gave a total of 12 possible samples as detailed in Table 8.

The fired foams were then lightly ground by hand and sieved to provide a sample fraction of between 0.5 mm and 3.25 mm for cell testing. A small amount of fines was generated (<5 wt.%).

Foaming Di-Substituted HA Method

Once the optimum foaming and firing conditions were found the following protocol was used for the di-substituted HA and the baseline HA materials. Each sample was dry milled prior to foaming, and the protocol used was as follows. Hydroxyapatite precipitate powder (60 g) was added to 90 mL of PVA solution (45 mL 16.67 wt.% PVA solution and 45 mL De-Ionised Water)

TABLE 4.4: Table demonstrating the 12 foamed samples generated by 3 variables; (i) HA Powder State, (ii) PVA loading during foaming of the powder, (iii) temperature at which the foam is fired.

HA Powder	PVA Loading	Firing Temperature
Precipitate	5 wt.%	1100
		1200
	10 wt.%	1100
		1200
Calcined	5 wt.%	1100
		1200
	10 wt.%	1100
		1200
Fired	5 wt.%	1100
		1200
	10 wt.%	1100
		1200

to produce a mixture of 40 wt.% HA powder and 5 wt.% PVA. The mixture was first mixed by spatula to ensure full wetting of HA powder, and then mechanically whisked for 90 s before being poured into silicone trays for oven drying. The materials were then dried at 50 °C for 48 h before being further processed. After drying, the green foams were broken apart into coarse fragments for firing at 1100 °C.

The fired foams were lightly ground and sieved to provide a sample fraction of between 0.5 mm and 3.25 mm for cell testing. A small amount of fines was generated <5 wt.%.

4.4 Characterisation

4.4.1 Chemical Analysis

The bulk elemental composition of the Mx-HA was determined by a combination of X-Ray Fluorescence (XRF) and Inductively Coupled Plasma Optical Emission Spectroscopy (ICP-OES).

For the ICP method (Boron and Silicon quantification) approximately 1 g of the HA material was dissolved in a 5% HNO_3 solution, and warmed gently to ensure complete dissolution. The solution was made-up to 50 mL volumetrically, and was analysed by ICP-OES (IRIS Advantage, Thermo Jarrell Ash) against a calibration traceable under ISO:17025 guidance note 34 for both boron and silicon. The results were corrected for the mass of

sample originally used and reported as a mg/Kg (ppm) figure for these elements in the original material.

For the XRF data a portion of the dried sample (approximately 1 g) was ignited for 1 h at 1200 °C to determine the loss on ignition. 1.5 g of the dried sample (corrected for loss on ignition) was then mixed with 7.5 g of Lithium Tetraborate in a platinum crucible and fused in a furnace at 1025 ° C for approximately 20 min or until dissolution is visibly complete. The resulting melt was then further heated for 5 minutes at 1200 °C and cast into a glass disc. The bead was analysed on an 'Axios' Panalytical X-Ray Fluorescence (XRF) spectrometer, calibrated internally and results reported in accordance to the methodologies set out in ISO 12677 - Chemical analysis of refractory products by X-ray fluorescence (XRF) – Fused cast-bead method. Errors for XRF are calculated to be either 1% relative or 0.05 wt.%, whichever is larger.

4.4.2 Physical Analysis

Particle size distribution analysis was performed on the HA material in accordance with ASTM E2651-10 Standard Guide for Powder Particle Size Analysis using a laser diffraction technique. The HA was sampled by cone and quartering in order to obtain a representative sample and the required amount as determined by the obscuration value. The HA was then added to water in the measuring cell of a Malvern Mastersizer 3000. The cycle of operation began which consisted of a 10 s pause to allow the system to stabilise followed by 1 min of particle size measurement. This measurement cycle is repeated another 4 times so that a representative result can be determined.

During the process of sample addition and measurement no dispersion by ultrasonication was used due to potential break down of the granules leading to an erroneous result. The technique automatically generated five (5) determinations per sample where an average was taken and reported.

Equipment and method validation data was obtained using the National Institute of Standards and Technology (NIST) standard reference materials 1003c and 1004b – glass beads for particle size distribution. The standard reference materials were run ten times with the d10, d50 and d90 percentiles measured with associated single standard deviations determined; the means of these values were compared against the published data and associated single standard deviations as provided by NIST.

Zeta charge of the HA materials was measured using a Colloidal Dynamics Zeta Probe. The HA material was milled and sieved to $< 37\,\mu\mathrm{m}$ to ensure that the powder could behave in a colloidal fashion. 3 g of powder was

then added to ∼297 mL water to give ∼1 wt.% suspension. The suspension is agitated by a paddle stirrer at the bottom of the vessel. Typical operation consists of measured addition of KOH and HCl to set pH values to perform a sweep of Zeta vs pH values. Typically this sweep starts at the pH of the suspension after powder addition, and is then increased in integer amounts to pH 11, and then back down in integer amounts to pH 4. Measurements are carried out after the reading has stabilised. Errors are calculated based on a series of multiple readings of standard materials at 1, 2.5, and 5 wt.% values performed by Nathan Atkinson and Dr. Philip Jackson. The error on the kit is calculated to be $\pm$ 0.12 mV.

Surface area of the samples was measured by Brunauer, Emmet, Teller (BET) method. BET refers to the mathematical model used to adapt Languir's model for monolayer adsorption and desorption. Measurements were taken by a Gemini 6 surface area and pore size analyser, and using a FlowPrep 060 purging system. Approximately 0.5 g ($\pm$ 0.2 g) of sample is placed within a sample tube with the exact mass weighed by difference. The sample is then purged under nitrogen at 110 °C for 15-18 h in the FlowPrep 060. After sealing and allowing to cool the sample is placed into the Gemini 6. The sample is run in accordance with BS ISO 9277:2010 – Determination of the specific surface area of solids by gas adsorption – BET method.

Foam porosity was calculated by mercury intrusion porosimetry. The measurement was carried out on a Micrometrics Poresizer 9320 by placing 0.5 g into the penetrometer. The penetrometer is then flooded with mercury liquid at increasing pressures. At each pressure value the volume of mercury within the penetrometer is recorded. The technique uses mercuries non-wetting nature to like pressure to pore size by an inverse relationship. As the pressure goes up, the pore diameter available for mercury intrusion is reduced. The kit used is viable down to $0.003\,\mu\mathrm{m}$.

4.4.3 Chemical Analysis by FTIR

A portion of the sample was taken and gently ground in an agate mortar and pestle. A small aliquot ($\sim 5\,\mathrm{mg}$) of the ground sample was the placed directly onto the diamond crystal of a PIKE Technologies GladiATR attenuated total reflectance accessory that was installed in the sample compartment of an Agilent 660-IR FTIR spectrometer. A press was used to secure the sample in place and to ensure that a good contact was achieved between the sample and ATR crystal. The samples were measured in the region $4000 - 400\,\mathrm{cm}^{-1}$ wavenumbers, 64 scans were collected at a resolution of $4\,\mathrm{cm}^{-1}$

4.4.4 Morphology Analysis by SEM

The powder samples for the scanning electron microscope (SEM) were mounted onto a 10 mm adhesive carbon tab so as to present a monolayer of particles.

The mounted particles were sputter coated with ca. 50 nm of gold by plasma sputtering so as to render the surfaces electrically conductive in the electron beam.

The coated particulate was examined using a Jeol JSM6490LV Scanning Electron Microscope. Imaging was carried out using the secondary electron detector at low accelerating voltage (5 kV) so as to give maximal resolution of the morphology and surface texture of the particles. 'Spot size' is classed on the instrument as a nominal value between 1-100. As spot size relates to current, this 0-100 can be roughly translated to a value of 10 pA to 1 nA. A typical spot size used for imagining work is a setting of 0-20.

4.4.5 Structural Analysis by XRD

XRD was conducted on a Bruker D8 Advance using Bragg-Brentano parafocussing geometry. Data were collected from 5 to 62° 2Θ with a step size of 0.02° 2Θ and a count time of 0.5 s per step. A Lynxeye^{TM}solid state detector was employed with a fixed window of 3° 2Θ with all 192 channels collecting data simultaneously. Collected data were qualitatively examined using the Bruker diffract+ and EVA search-match software (search matched against the ICDD database). Quantification was conducted in accordance with in house methods M9 and M30 where the phase composition was determined by Rietveld refinement (performed by the previously mentioned software) of the whole diffraction trace (Internal method M30) and the amorphous content was determined by comparison of 10 HAP peaks against a pure HAP standard in accordance to ISO 13779-3 (2008).

Error analysis of quantitative phase analysis by XRD is a huge topic beyond the scope of this thesis. NIST has conducted a series of round robins to advise on best practice, and it is from the round robin published in 2001 that the errors are taken [154]. The results of the round robin produced a table with errors for the 25/75 section of participants at 6 different wt.% levels for a standard. The levels were 1, 5, 15, 30, 50, and 95 wt.%, with errors ranging from 0.2 - 15 relative percent, these numbers correspond to an absolute error of between 0.05 - 5.70 wt.%. This thesis uses a relative error of 5% as a compromise between the ranges of values seen. This number is considered acceptable as per a comment by Andre Guinier [155] that was

highlighted and thoroughly re-considered by Nicola Scarlett in a 2013 presentation [156]. As the amorphous content is calculated as the remainder of the sample, all amorphous values are assumed to be ± 5 wt.%.

XRD traces in this thesis have been compiled for display using ReX [157].

4.5 *In Vitro* Analysis

MG63 cells (human osteosarcoma), obtained from the European Collection of Cell Cultures (ECACC), with passage numbers ranging from 7-38, were cultured in complete Dulbecco's modified Eagle's media (CDMEM) consisting of Dulbecco's modified Eagle's media (DMEM) supplemented with 10% foetal calf serum (FCS), 2% penicillin/streptomycin, 2% HEPES buffer, 1% glutamine, 1% non-essential amino acids (Gibco Invitrogen, UK), and 0.85mM of ascorbic acid (Sigma Aldrich, UK). Cells were cultured in 75 cm^2 flasks (Falcon, Becton, Dickinson and Company, UK) at 37 °C in a humidified atmosphere with 5% CO_2. Cells were utilised once confluent by dissociating from the flask with trypsin-EDTA solution (a sterile, phosphate based saline solution (1x) containing 0.025% trypsin and 0.01% EDTA) and centrifuged at 1200 rpm for 4 min to produce a pellet which is resuspended in fresh media. Cell concentrations were calculated using a haemocytometer with viable cells identified using trypan blue exclusion.

HA powders and foams were washed with ammonium chloride to remove soluble alkali oxides (such as CaO and MgO), and then sterilised in an autoclave at 121 °C. Tissue culture plastic was used as a positive control for cell growth. Samples were measured out by a scoop ($\sim 0.78\,\mathrm{mL}$) method. Cells were seeded onto samples at a density of 40,000 cells/cm^2 and were incubated at 37 °C in a humidified atmosphere with 5% CO_2.

To assess biological activity; metabolic activity, DNA concentration, and Osteocalcin activity were measured at designated time points. An Alamar Blue assay was run on the cells before washing samples three (3) times with warm PBS prior to the addition of $0.5\,\mu\mathrm{L}$ of sterile deionised water to each well. Cells were then lysed by freezing the well plates before thawing at room temperature and transferring the contents into eppendorfs as per the established in house protocol. To ensure sufficient lysing had occurred, samples were subjected to a further two (2) freeze/thaw cycles.

4.5.1 Metabolic Activity

To measure metabolic activity, an Alamar Blue assay was run. The sample was washed with PBS three times before a solution of Alamar Blue (1:10

Alamar Blue) warm Hanks balanced salt solution (HBSS)) (0.5 mL) was added. The sample was then incubated for 90 min. After incubation 100 µl of the dye was transferred in triplicate into a 96 well plate from each well. Fluorescence was read at 530 nm excitation and 570 nm emission using a FLx800 microplate reader (BioTek Instruments Inc). The level of fluorescence is directly related to the amount of Alamar Blue dye that had been reduced over 90 min, and so the level of cell metabolic activity.

Alamar Blue utilizes resazurin as a blue dye which is reduced to resorufin which is pink. Resazurin does not fluoresce under green light (530 nm), whilst resorufin does and emits photons at 570 nm. The resazurin is reduced by all steps of the electron transport chain as its oxidation potential is greater than any of the cytochromes, meaning it can be reduced by FMNH2, FADH2, NADH, NADPH, and cytochromes. This reduction typically occurs in the cell mitochondria and is therefore indicative of total cell metabolism rather than of a specific process activity.

4.5.2 DNA Concentration

DNA standards were prepared using calf thymus (Sigma, UK) and TNE buffer (10 mM Tris, 2M NaCl, and 1 mM EDTA in deionised water, adjusted to pH 7.4) as a diluent Cell lysate (100 µl) from each sample was put into a 96 well plate along with 100 µl of each standardisation point. 100 µl of Hoechst stain 33258 was then added to each well (bis-benzimide 33258 (1 mg) in deionised water, diluted 1:50 in TNE buffer) and the plate agitated by placing on a plate shaker at 150 rpm. Fluorescence was measured at 360 nm excitation and 460 nm emission using a FLx800 microplate fluorimeter (BioTek Instruments Inc). DNA concentrations were calculated from a standard curve generated using the standards prepared in the first step.

Hoechst stains (be that 33258 or another stain) work by binding to the minor groove of DNA, preferentially at AT-rich double strands although with an excess of dye and sufficient time, the whole strand can be bound. The bound form of the dye has an emission maximum around 461 nm following excitation at 350 nm. The unbound dyes has a fluorescence maximum around 510-540 nm, and this shift allows for the differentiation between bound and unbound dyes.

4.5.3 Osteocalcin Assay

Samples were then run as specified by the ELISA Osteocalcin kit, purchased from Invitrogen. Briefly; 25 µl of sample was added to an antibody coated well plate in triplicate. Then 100 µl of working Anti-OST-HRP was added

and incubated for 2 h at room temperature. The Osteocalcin bound to the antibody-coated well plate. The HRP then binds to the Osteocalcin. Remaining HRP is washed off by rinsing with the specified wash solution three times. Stabilised Chromogen (100 µl) is then added and incubated for 30 min. The Chromogen reacts with the remaining HRP, causing a colour change. This reaction is stopped by addition of 100 µl of stop solution. Samples are then read at 450 nm. Absorbance is converted to mg/ml of protein by use of a calibration curve run at the same time.

4.5.4 Data Analysis

All data is presented with error bars where appropriate, with the error bar being calculated as the standard error of the mean ($\sigma/\sqrt{n}$), statistical method used was a single factor ANOVA, followed by a Scheffé test. Experiments were run two times. The two runs were split between Zhiqiang Zheng and Katherine Bostock (both students of Colin Scotchford). Both data sets contained both a positive control (Pure HA), and a negative control (Tissue Culture Plastic)

5 Results

In this chapter the analysed results are displayed along with examples of raw data where appropriate. Trends and comparisons are discussed in a later chapter (section 6)

5.1 Validation of Synthesis

This section covers the synthesis and validation of a synthesis route for the synthesis of substituted hydroxyapatites (HA).

5.1.1 Firing Temperature

To consolidate the crystal structure of ceramics, especially those precipitated and therefore containing a large amount of amorphous material, a high temperature firing stage is typically used to increase the crystallinity. To assess different firing temperatures, a sample was fired at 3 different temperatures (600, 1000, or 1120 °C). This data is shown in figures 5.1, 5.2, and 5.3. Raw XRD traces are omitted from this section due to their commercially sensitive nature. As the graphs demonstrate, 600 °C is not hot enough as a peak firing temperature to cause full crystallisation. There are a few differences between firing at 1120 °C and 1000 °C, but notably the higher firing temperature results in reduced amorphous content. This decrease in amorphous content is the main driver for using 1120 °C as the firing temperature for powders in this thesis, although 1000 °C would still be serviceable.

5.1.2 Ca:P Ratio

As part of the initial assessment of producing substituted HA samples, a series of experiments were carried out with substitutions consisting of Sr^{2+}, ${BO_3}^{3-}$, or ${SO_4}^{2-}$. In these experiments, due to poor calibration of the H_3PO_4 to 6M a low Ca:P ratio caused the formation of secondary phases. This can be seen in figure 5.6 where the formation of β-TCP is clearly identified. Usefully, the data also shows low levels of amorphous content which

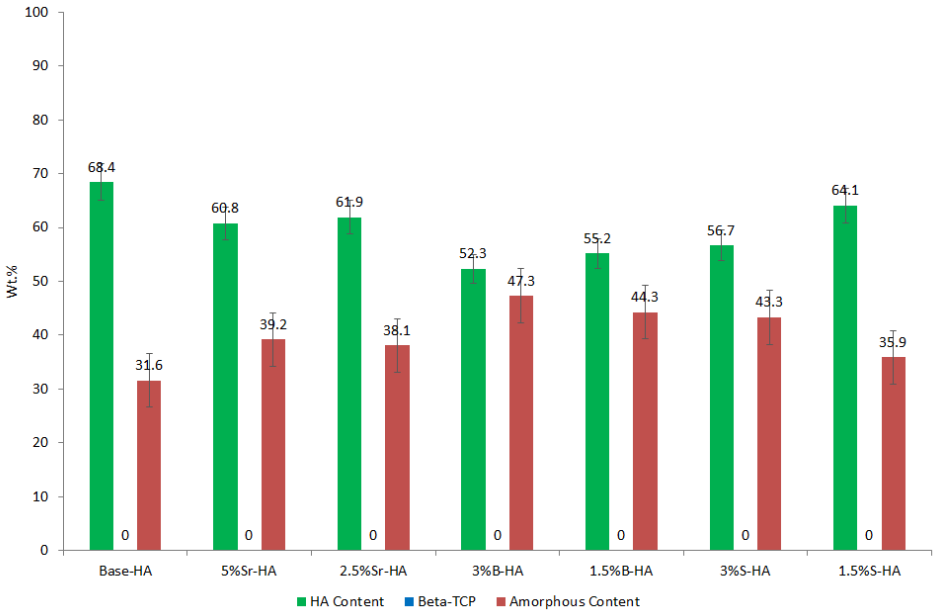


FIGURE 5.1: Phase composition after firing at 600 °C. Wt.% HA and total crystallinity were measured. The secondary phase was β-TCP (TriCalcium Phosphate) which crystallised out at temperature. Errors on phase compositions are 5% relative for each phase, and 5% actual for amorphous as described in section 4.4.5.

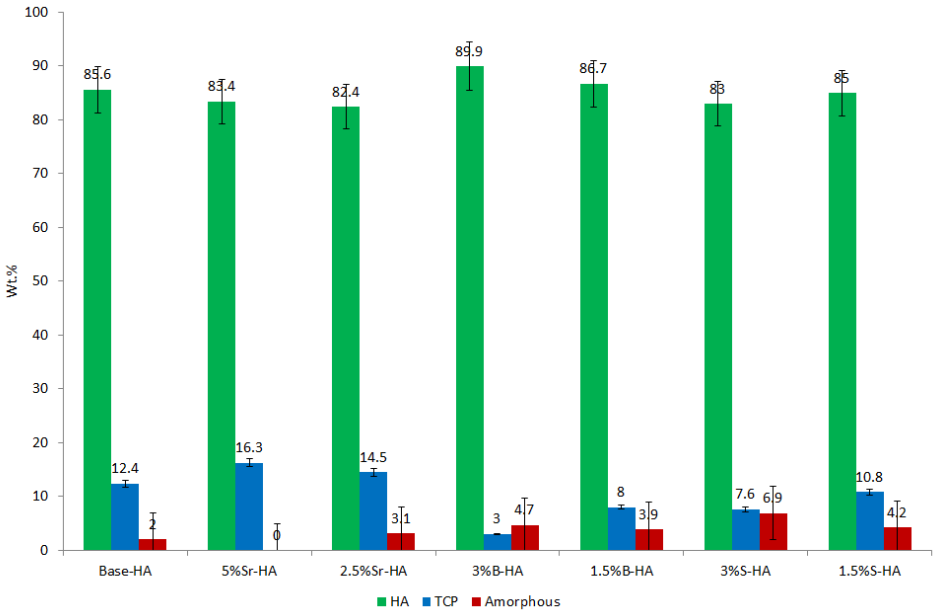


FIGURE 5.2: Phase composition after firing at 1000 °C. Wt.% HA and total crystallinity were measured. The secondary phase was β-TCP (TriCalcium Phosphate) which crystallised out at temperature. Errors on phase compositions are 5% relative for each phase, and 5% actual for amorphous as described in section 4.4.5.

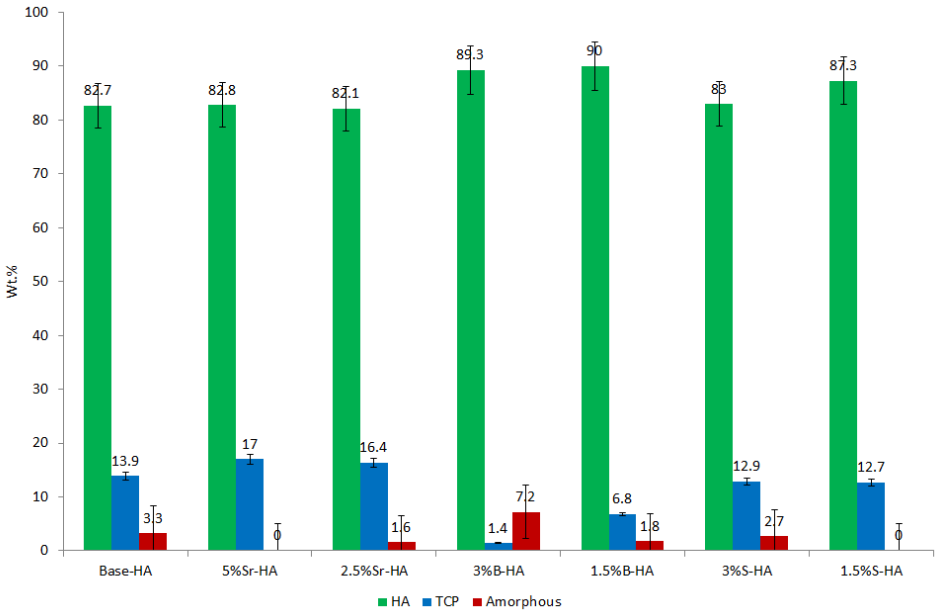


FIGURE 5.3: Phase composition after firing at 1120 °C. Wt.% HA and total crystallinity were measured. The secondary phase was β-TCP (TriCalcium Phosphate) which crystallised out at temperature. Errors on phase compositions are 5% relative for each phase, and 5% actual for amorphous as described in section 4.4.5.

demonstrates that the firing was successful. A complete overview of data for the chemical composition (table 5.1) and the crystallographic composition (table 5.2) are available below.

A key indicator of the synthesis success is the pH vs time plot that is generated by the reactor used. Figures 5.4 and 5.5 demonstrate where a pH crash has and hasn't occurred respectively. The crashing of pH can be due to either an over addition of acid, or due to the use of weak bases as the cation sources (i.e. $Ca(NO_3)_2$). Over addition of acid is often caused by poor control of the molarity of the phosphoric acid, especially when using high concentrations. The result of this work was to demonstrate the requirement for a greater clarity of the batch-to-batch variations of the H_3PO_4 concentration by way of titration so as to remove it as a potential source of secondary phase generation.

5.1.3 Ca Source

A scoping exercise was carried out to assess the various calcium sources to ensure that the most suitable choice was used. Experiments were carried out both with (figure 5.7) and without (figure 5.8) pH control. The hydroxide did not require pH adjustment to keep it above pH 9 hence its lack of

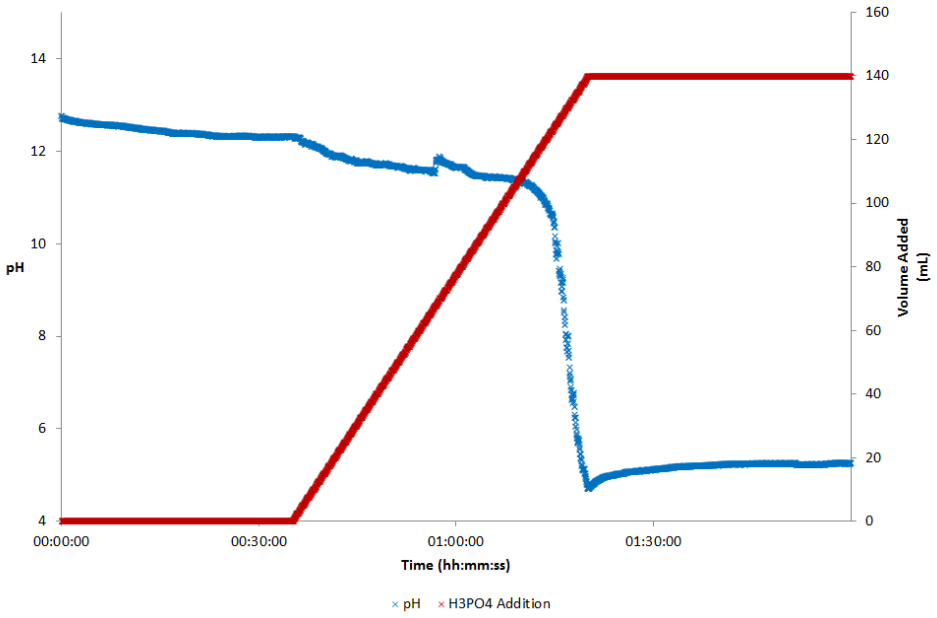


FIGURE 5.4: pH and volume addition vs time clearly demonstrating the sudden drop associated with over addition of acid.

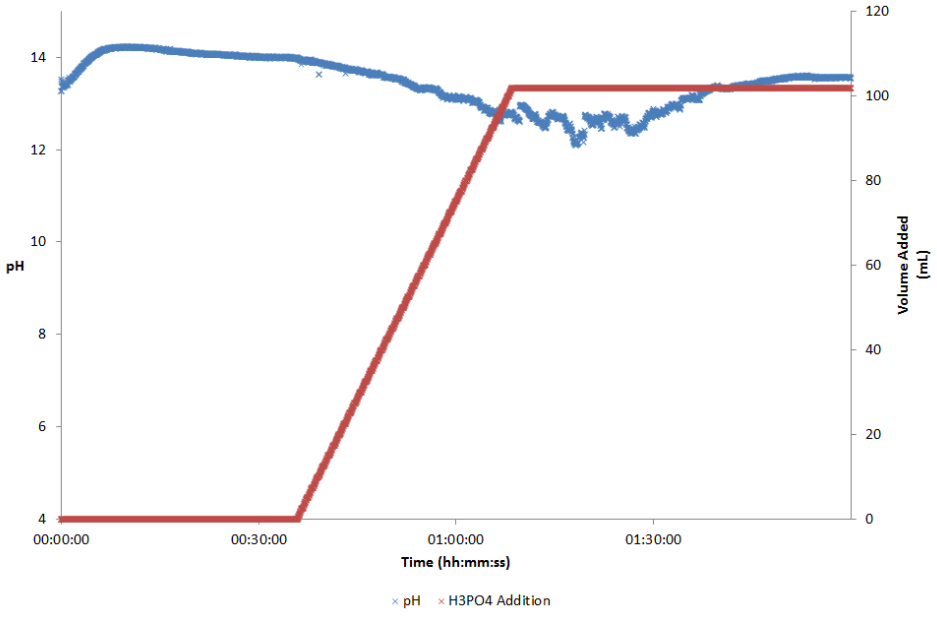


FIGURE 5.5: Graph demonstrating correct addition of phosphoric acid. As the Ca:P ratio does not pass below 1.5, there is insufficient acid to fully neutralise the Ca(OH)2, which ensures an alkali system.

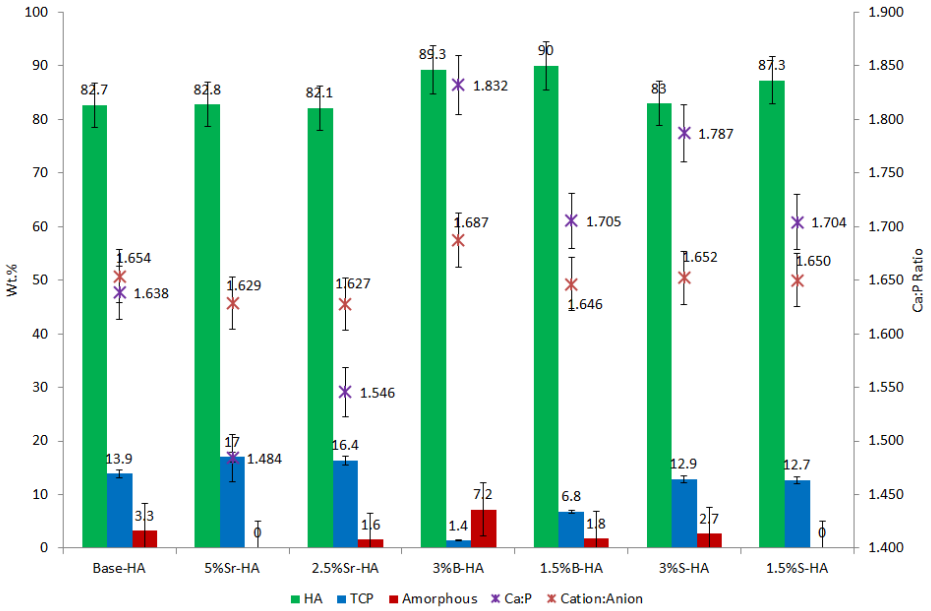


FIGURE 5.6: Comparison of Crystallinity and Ca:P Ratio in Samples Fired at 1120 °C. Errors on phase compositions are 5% relative for each phase, and 5% actual for amorphous as described in section 4.4.5

TABLE 5.1: Chemical composition (in wt.%) of experiments Base-HA, 5%Sr-HA, 2.5%Sr-HA, 3%B-HA, 1.5%B-HA, 3%S-HA, and 1.5%S-HA fired at 1120 °C as determined by XRF, ICP-OES, and LECO. XRF was used to determine CaO, P_2O_5, SrO, MgO, and SiO_2 content. ICP-OES was used in Boron containing samples to determine B_2O_3 content. LECO was used in Sulphur containing compounds to determine S content. Errors are calculated to be 1% relative, or 0.05 wt.%, whichever is larger

Experiment	**CaO**	**P_2O_5**	**SrO**	**MgO**	**SiO_2**	**B_2O_3**	**S**
Base-HA	55.8	43.1	0.02	0.43	0.06	N/A	N/A
5%Sr-HA	48.9	41.7	8.04	0.38	0.08	N/A	N/A
2.5%Sr-HA	52.1	42.7	4.20	0.40	0.05	N/A	N/A
3%B-HA	57.0	39.4	0.02	0.43	0.20	1.77	N/A
1.5%B-HA	56.0	41.6	0.02	0.43	0.09	0.91	N/A
3%S-HA	55.3	39.2	0.02	0.42	0.09	N/A	1.60
1.5%S-HA	55.0	41.2	0.02	0.43	0.08	N/A	0.78

TABLE 5.2: Crystalline composition (in wt.%) of experiments Base-HA, 5%Sr-HA, 2.5%Sr-HA, 3%B-HA, 1.5%B-HA, 3%S-HA, and 1.5%S-HA fired at 1120 °C as determined by XRD. Errors on phase compositions are 5% relative for each phase, and 5% actual for amorphous as described in section 4.4.5

Experiment	**HA**	**β-TCP**	**α-TCP**	**Amorphous**	**Other**	**Phase**
Base-HA	82.7	13.9	0.0	3.3	0.0	
5%Sr-HA	82.8	17.0	0.0	0.0	0.2	$Ca_2P_2O_7$
2.5%Sr-HA	82.1	16.4	0.0	1.6	0.0	
3%B-HA	89.3	1.4	0.0	7.2	0.9	CaO
					0.3	MgO
					0.5	B_2O_3
					0.5	$Ca_3B_2O_6$
1.5%B-HA	90.0	6.8	0.0	0.0	1.0	B_2O_3
					0.4	$Ca_3B_2O_6$
3%S-HA	83.0	12.9	0.4	2.7	0.3	MgO
					0.6	$CaSO_4$
1.5%S-HA	87.3	12.7	0.0	0.0	0.0	

inclusion in the pH adjusted data set, whilst both the nitrate and calcium salts showed a greater amount of HA formed when adjusted to pH 9. The citrate salt showed poor consistency between samples, and an unsatisfactory level of HA formation (12.8 wt.%) both with and without pH control. Phases were identified by XRD. The XRD traces are presented below and split into those run without pH control (figure 5.9), and those run with pH control (figure 5.11). The sample using $Ca(OH)_2$ as the precursor has been left on all traces as a reference. Enlargements of the traces in the range 30 - 40 2θ are presented for without pH control (figure 5.10) and with pH control (figure 5.12).

5.1.4 Boron-Substituted Hydroxyapatite

A range of ^{11}B containing substituted HA powders were made in order to probe substitution locations by neutron beam diffraction. These powders were also characterised by FTIR in order to provide information on which form the borate substitutions had taken to aid in refining the diffraction data. It can be seen from the comparison of FTIR spectra (figure 5.17) that there is an increase in a range of borate species at different loadings, along with a reduction in the amount of phosphate and hydroxyl groups. A table of the stretching frequencies used to assign species to the data can be found in table 5.3. All FTIR traces are presented below in figures 5.13, 5.14, 5.15, 5.16, and 5.17.

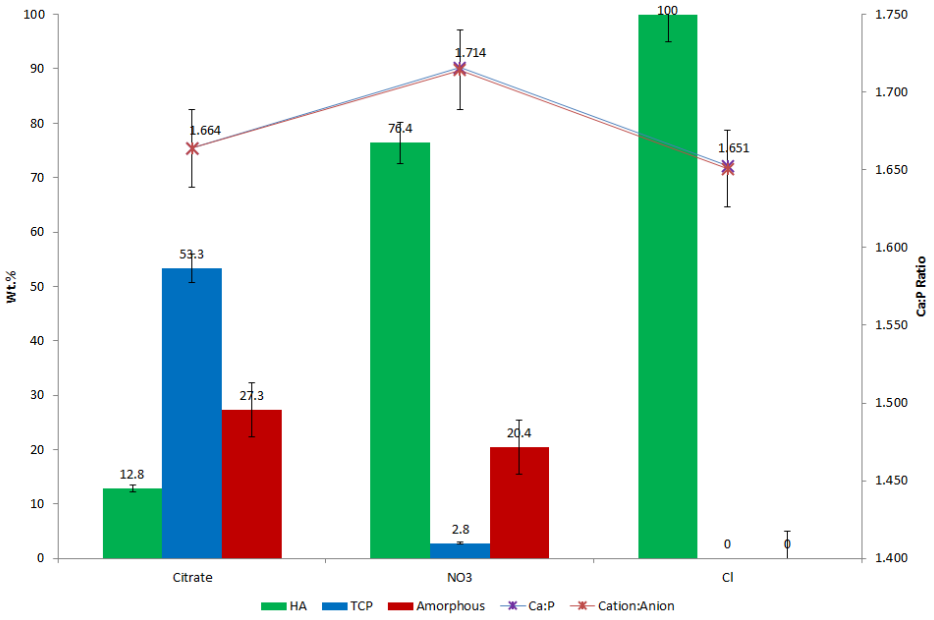


FIGURE 5.7: Comparison of crystal phases from calcium phosphate samples precipitated with varied Ca-sources controlled to pH 9, after firing at 1120 °C. The hydroxide salt is not presented as the pH remained above pH 9 throughout the addition and so pH control was not needed to adjust to a pH >9. Errors on phase compositions are 5% relative for each phase, and 5% actual for amorphous as described in section 4.4.5

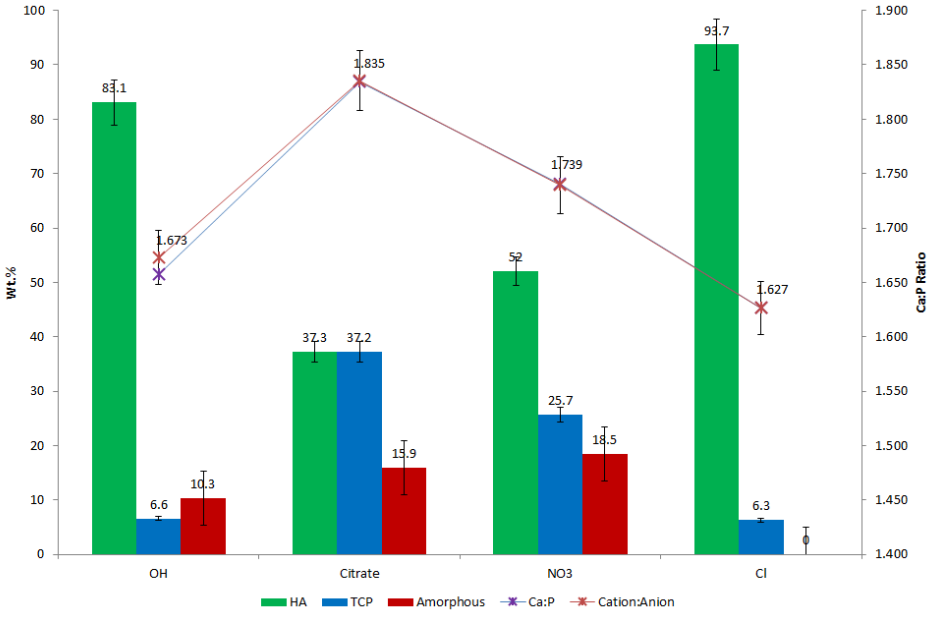


FIGURE 5.8: Comparison of crystal phases from calcium phosphate samples precipitated with varied Ca-sources without pH control, after firing at 1120 °C. Errors on phase compositions are 5% relative for each phase, and 5% actual for amorphous as described in section 4.4.5

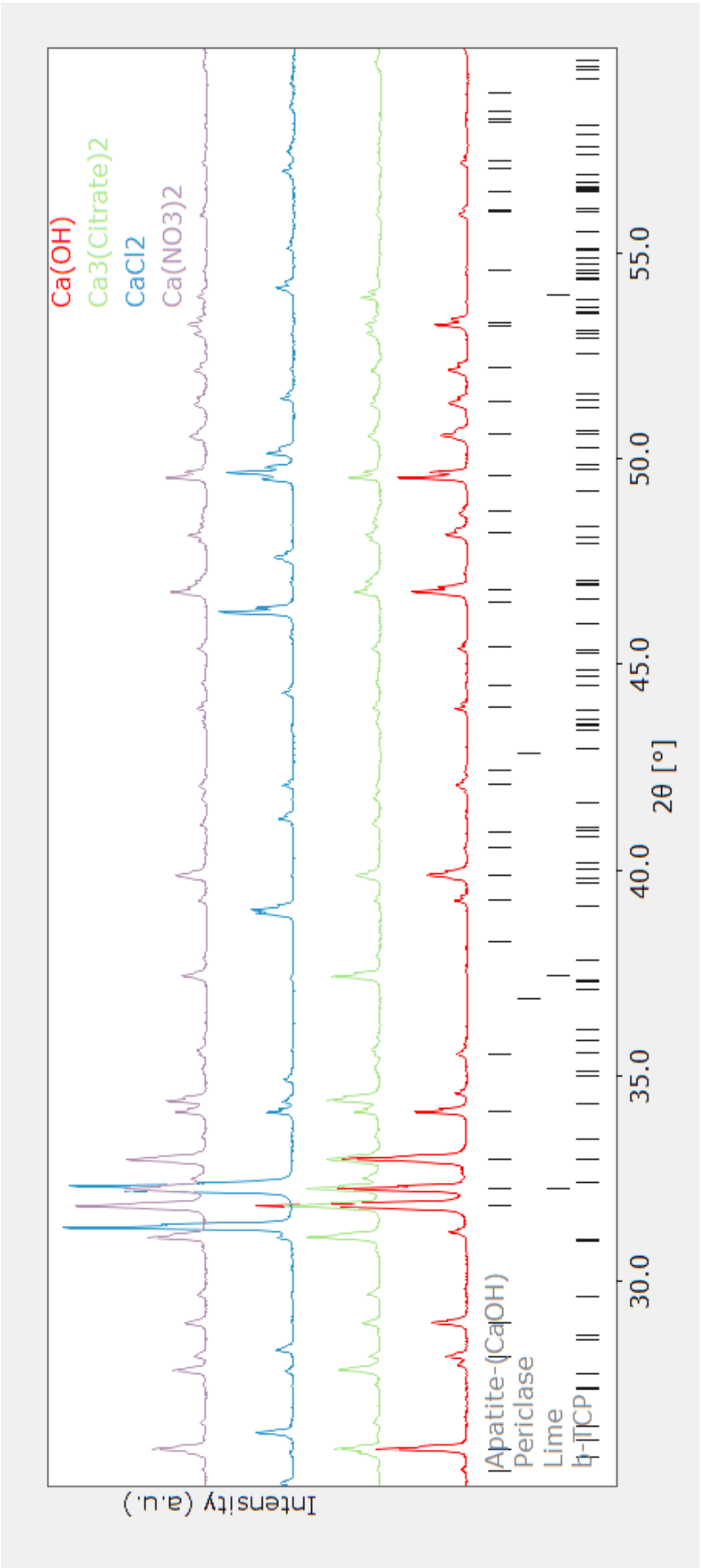


FIGURE 5.9: XRD Trace showing differences between samples prepared with various Calcium precursors precipitated without pH control. Although the range 25-60 2Θ is very crowded, this area gives the most quantifiable detail and is interpreted by software.

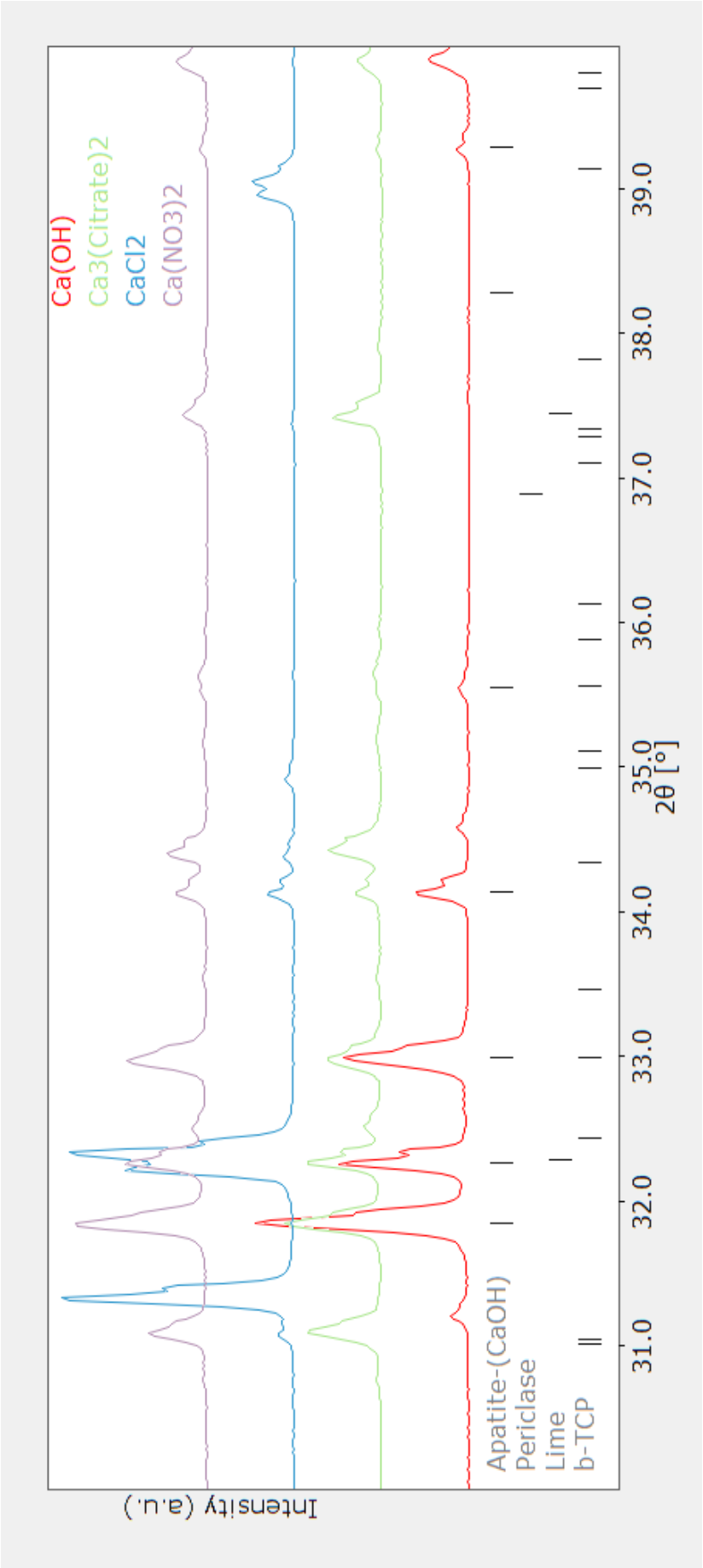


FIGURE 5.10: XRD Trace showing differences between samples prepared with various Calcium precursors precipitated without pH control. Traces enlarged to show the range of 30 - 40 2θ.

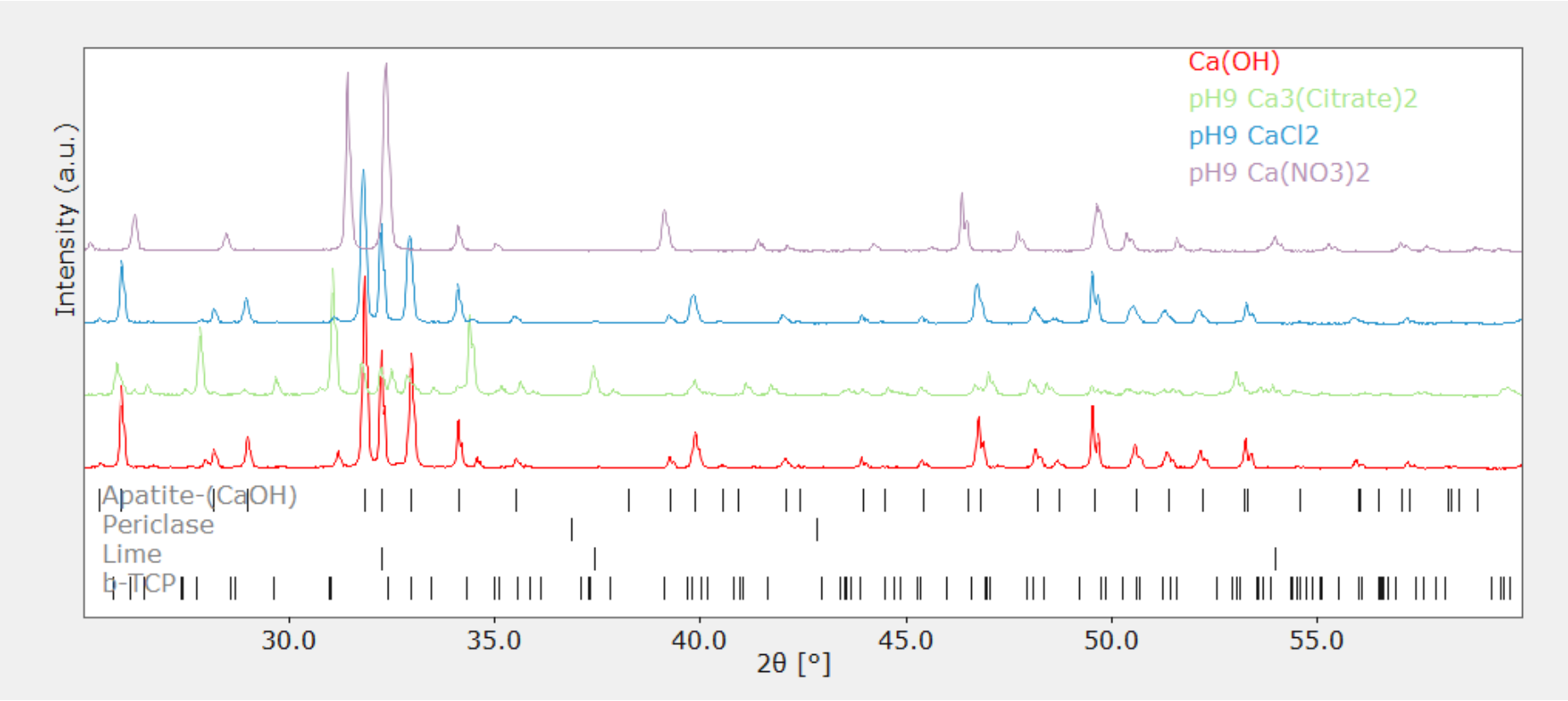


FIGURE 5.11: XRD Trace showing differences between samples prepared with various Calcium precursors precipitated with pH control to pH 9. Although the range 25-60 2Θ is very crowded, this area gives the most quantifiable detail and is interpreted by software.

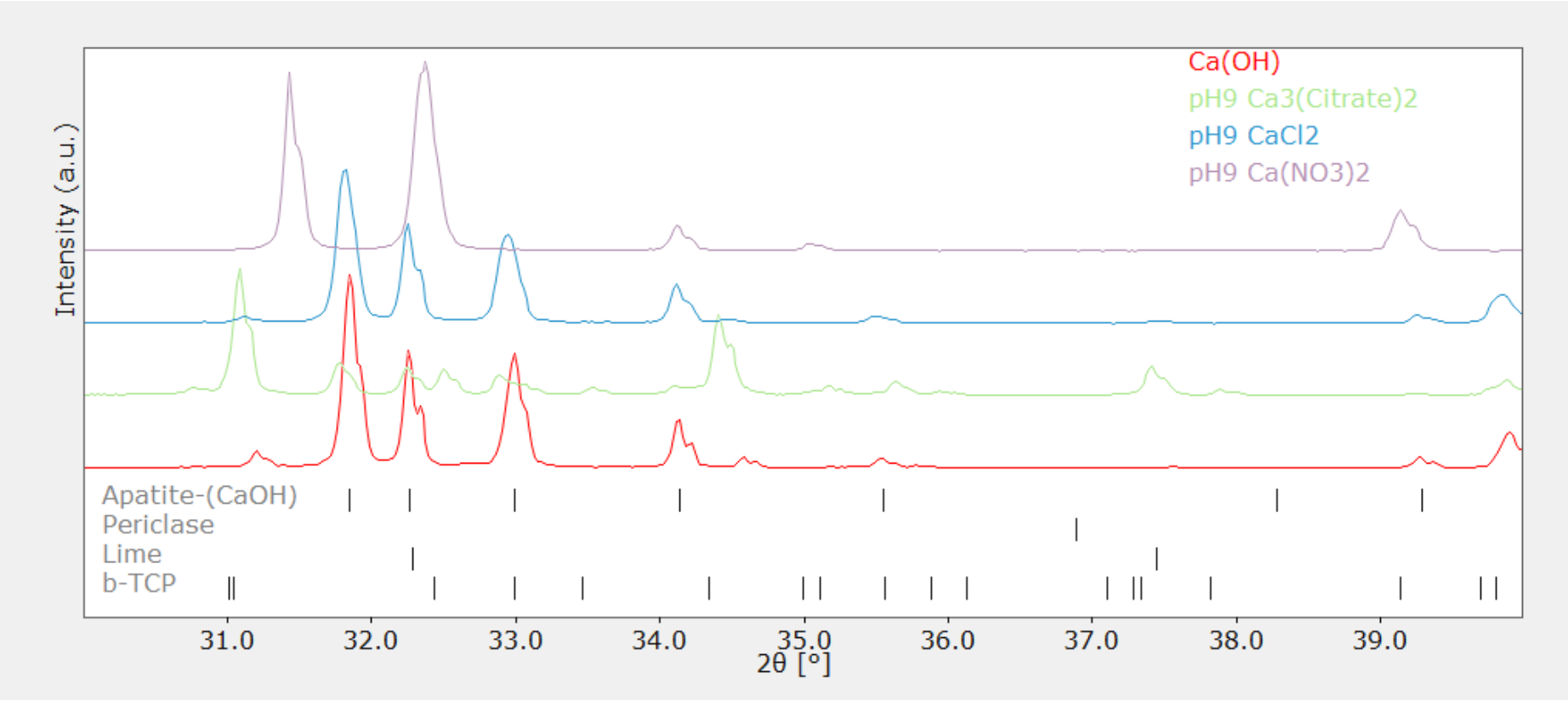


FIGURE 5.12: XRD Trace showing differences between samples prepared with various Calcium precursors precipitated with pH control to pH 9. Traces enlarged to show the range of 30 - 40 2θ.

TABLE 5.3: Table of FTIR stretching frequencies for Borate substituted HA as adapted from [109]. $^{*}Ca_3(BO_3)_2$, $^{**}Ca(OH)_2$

IR wave number (cm^{-1})	Assignment
3643	$\nu_{OH}{}^{**}$
3570	ν_{SOH}
2002	$\nu_3(BO_2)$
1932	$\nu_3(BO_2)$
1304	$\nu_3(BO_3)$
1280	$\nu_3(BO_3)^*$
1253	$\nu_3(BO_3)$
1229	$\nu_3(BO_3)^*$
1208	$\nu_3(BO_3)$
1090	$\nu_3(PO_4)$
1040	$\nu_3(PO_4)$
962	$\nu_1(PO_4)$
903	$\nu_1(BO_3)^*$
794	$\nu_2(BO_3)^*$
784	$\nu_2(BO_3)$
771	$\nu_2(BO_3)$
755	$\nu_2(BO_3)$
717	$\nu_2(BO_3)^*$
630	ν_{LOH}
616	$\nu_4(BO_3)$
603	$\nu_4(PO_4)$
571	$\nu_4(PO_4)$
472	$\nu_2(PO_4)^*$

The preliminary Neutron Beam data is included, although currently interpretation is proving difficult due to a lack of information regarding the speciation of the borate - a topic covered in section 3.4.4. The full traces are presented in figure 5.18, with enlargements of interesting peaks shown in figures 5.19 and 5.20. An initial review of the literature for any insight from other glass or ceramic neutron diffraction of borate species has not proven successful.

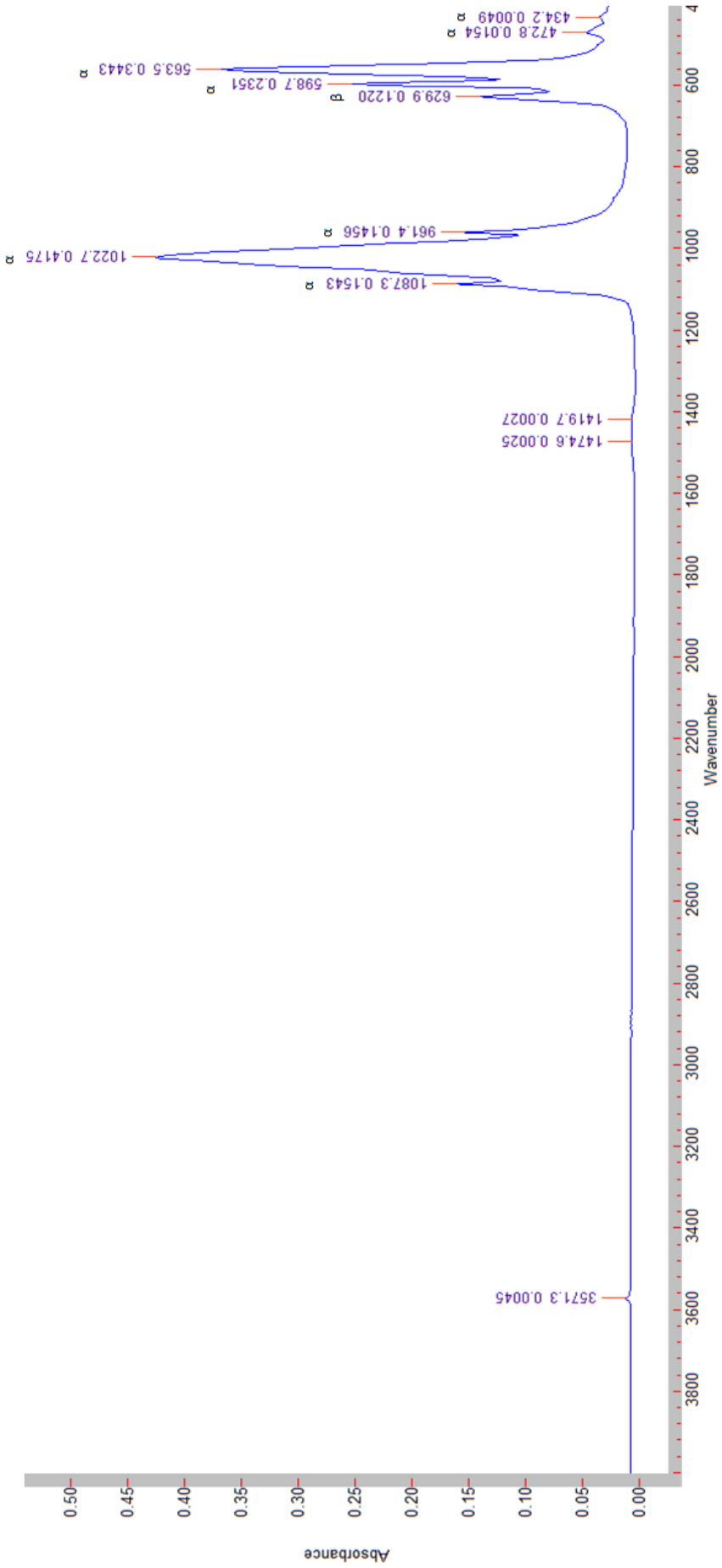


FIGURE 5.13: FTIR spectra of HA with peaks labelled. α denotes PO_4, β denotes OH. Peaks were assigned by following the table in [109].

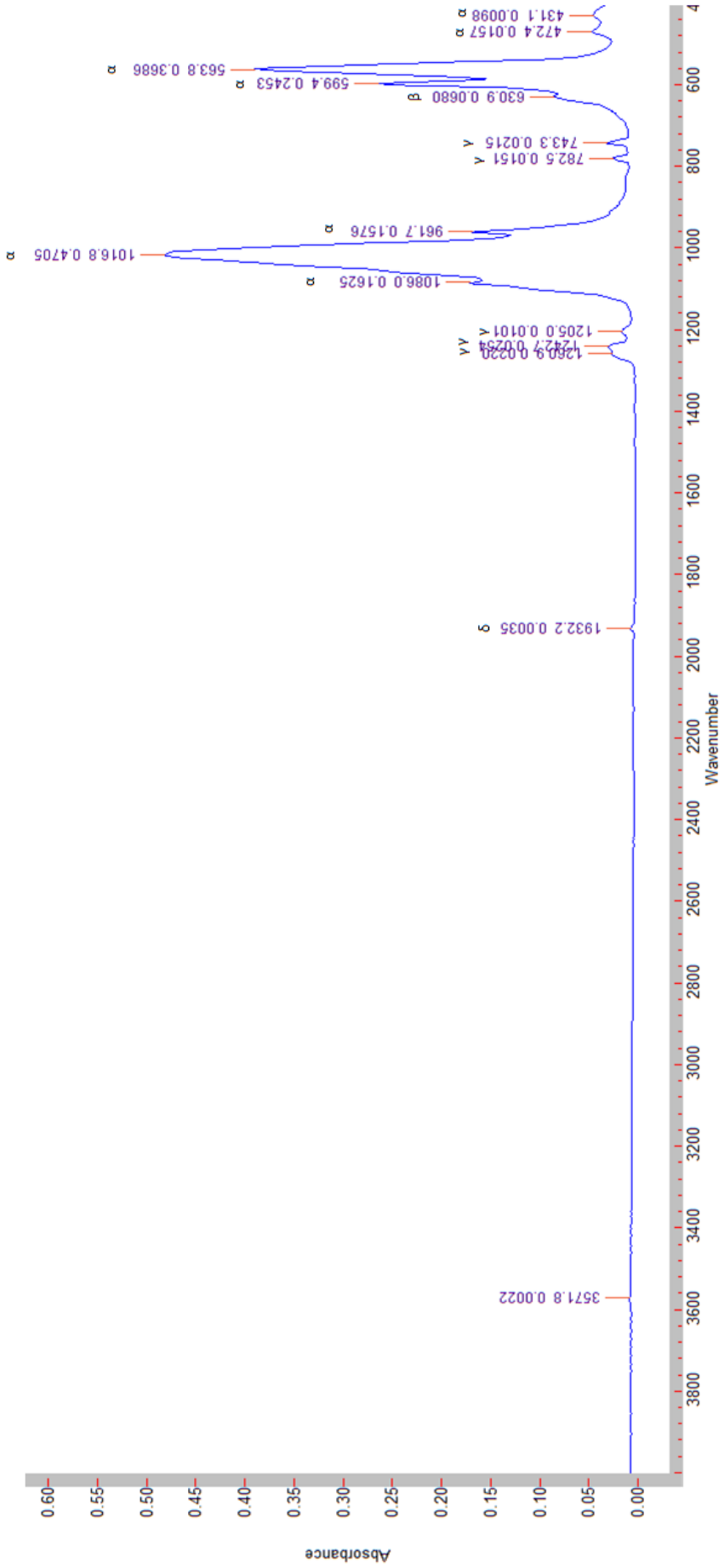


FIGURE 5.14: FTIR spectra of 2.5%B-HA with peaks labelled. α denotes PO_4, β denotes OH, γ denotes BO_3, and δ denotes BO_2. Peaks were assigned by following the table in [109]

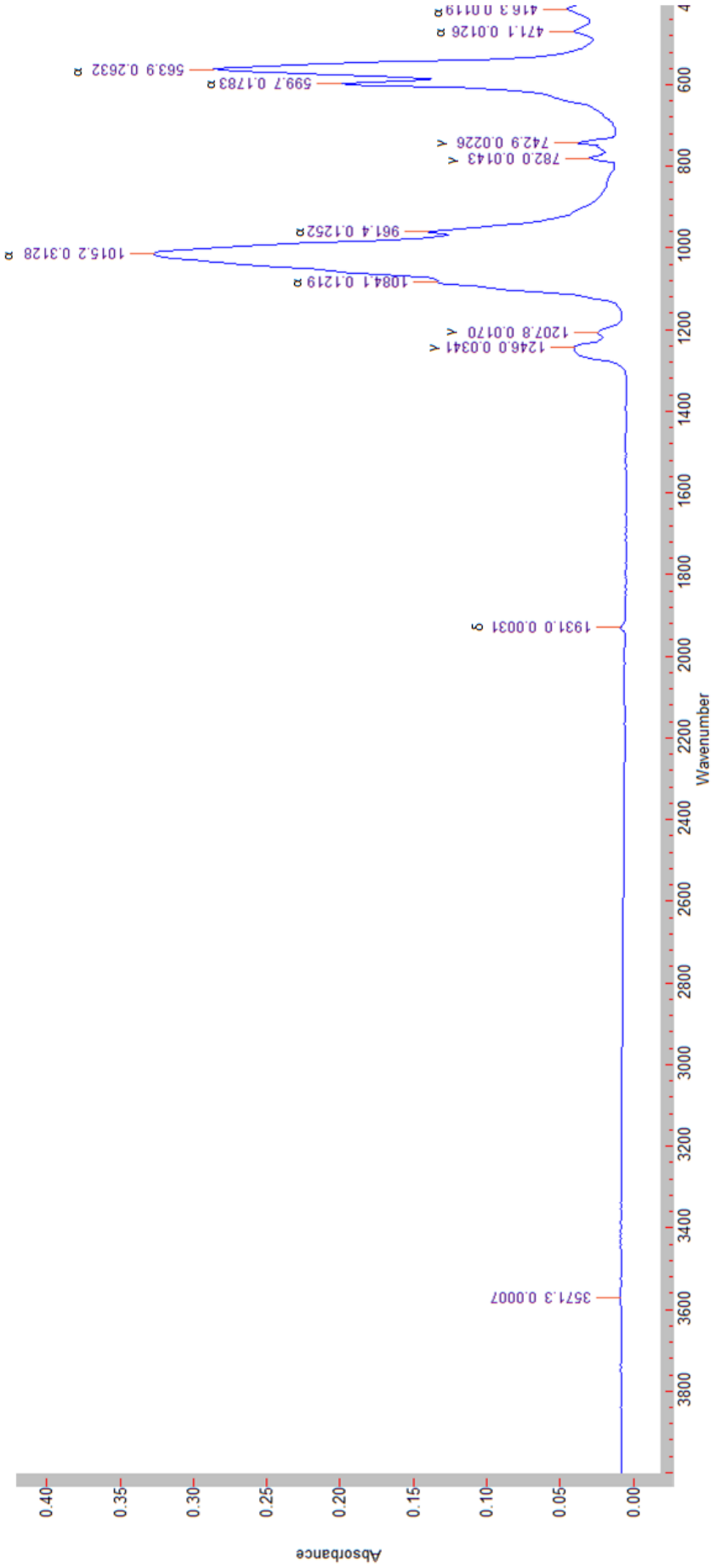


FIGURE 5.15: FTIR spectra of 5%B-HA with peaks labelled. α denotes PO_4, β denotes OH, γ denotes BO_3, and δ denotes BO_2. Peaks were assigned by following the table in [109]

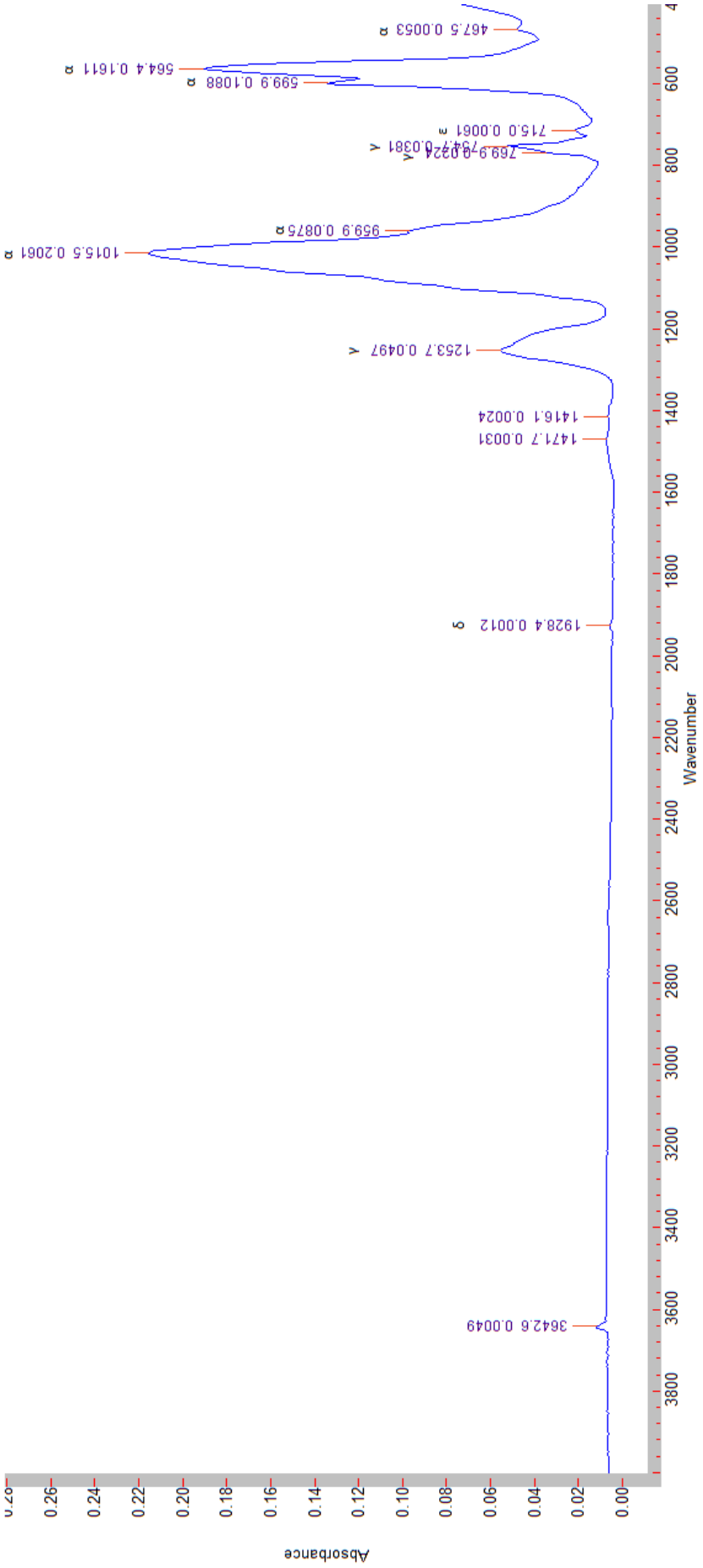


FIGURE 5.16: FTIR spectra of 10%B-HA with peaks labelled. α denotes PO_4, β denotes OH, γ denotes BO_3, δ denotes BO_2, and ϵ denotes BO_3 in $Ca_3(BO_3)_2$. Peaks were assigned by following the table in [109]

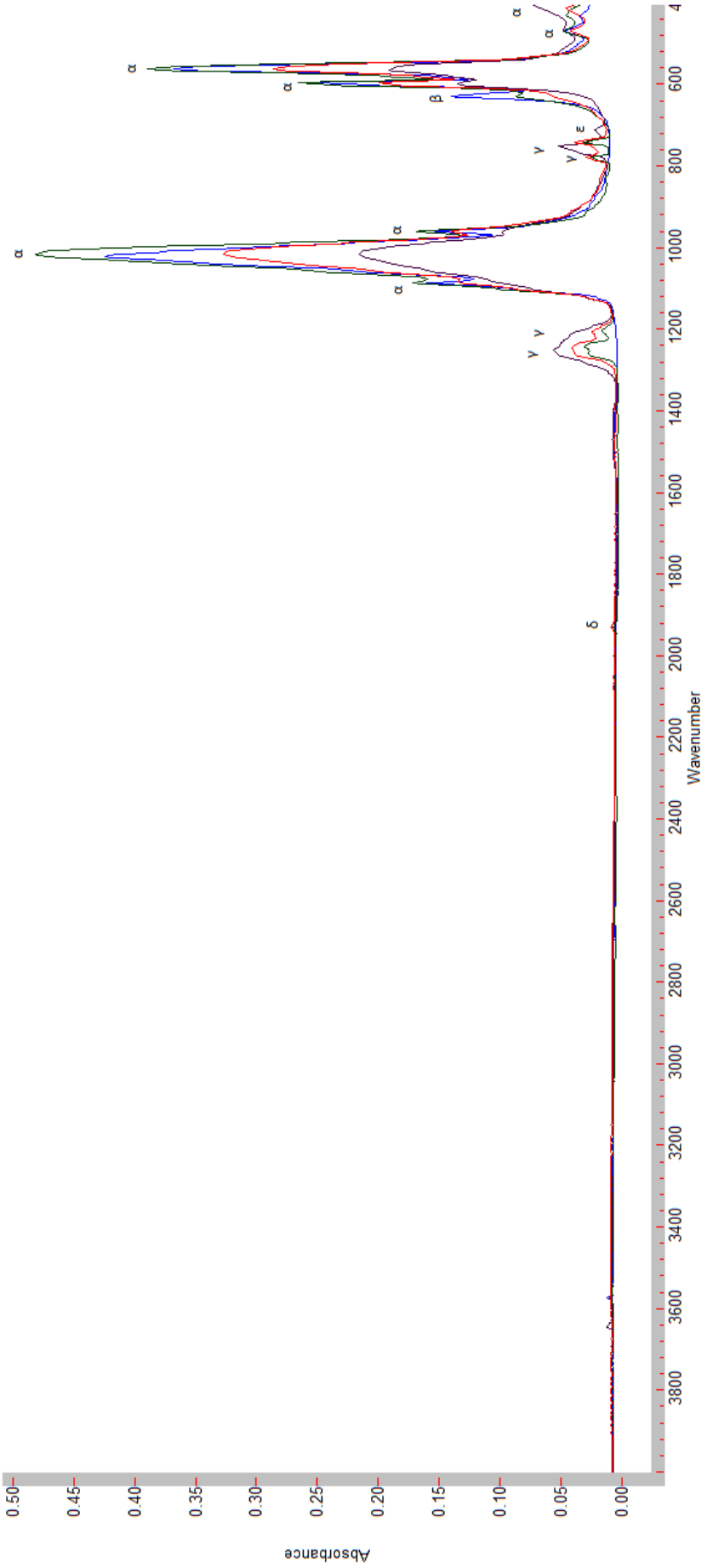


FIGURE 5.17: Comparison of all 4 samples. HA is shown as the blue line, 2.5%B-HA is green, 5%B-HA is orange, and 10%B-HA is purple. α denotes PO_4, β denotes OH, γ denotes BO_3, δ denotes BO_2, and ϵ denotes BO_3 in $Ca_3(BO_3)_2$. Peaks were assigned by following the table in [109]

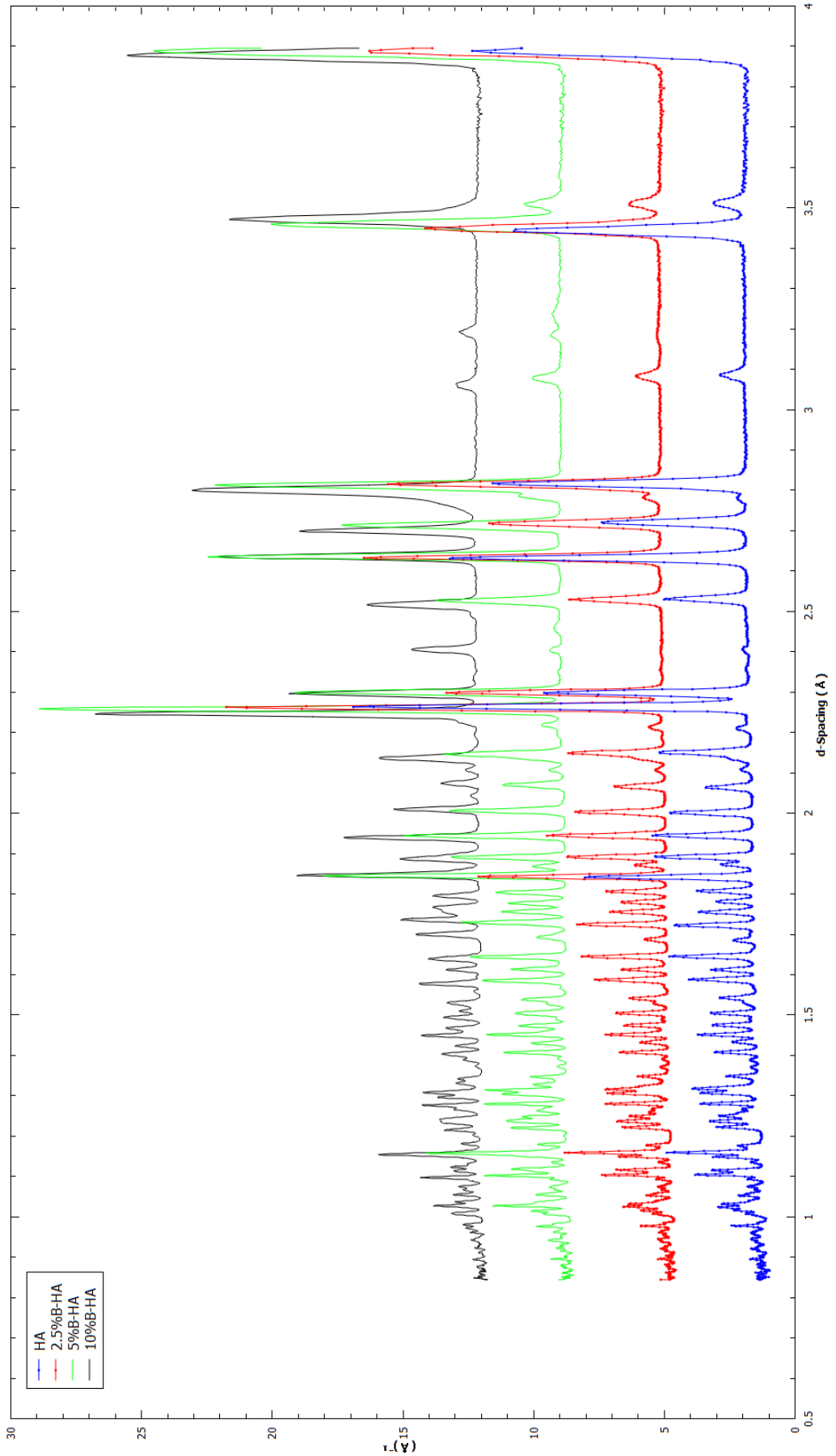


FIGURE 5.18: Neutron Beam diffraction traces for 3 Borate containing samples and 1 baseline HA sample.

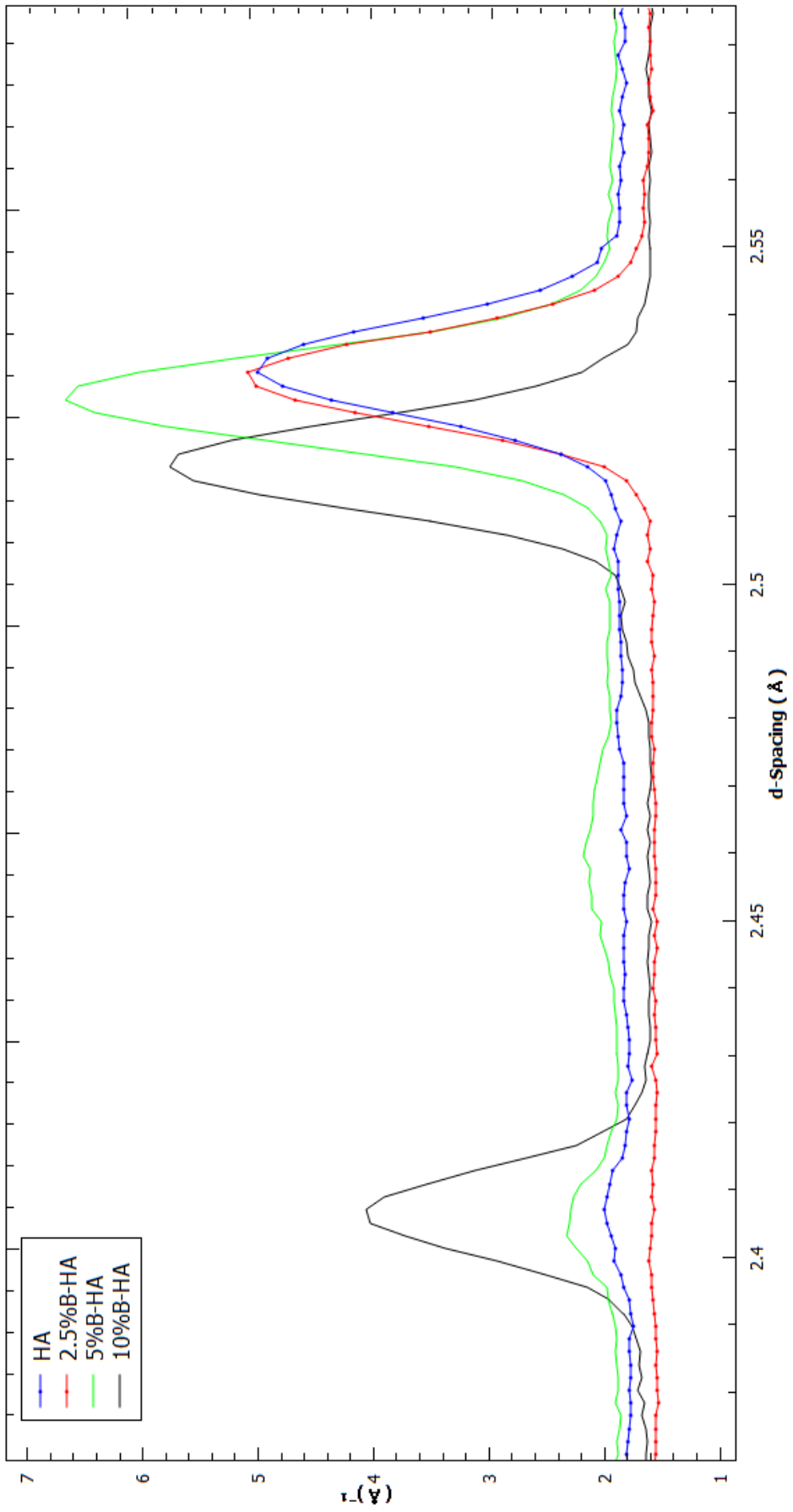


FIGURE 5.19: Neutron Beam diffraction traces for 3 Borate containing samples and 1 baseline HA sample. Highlighting the peak shifts seen with increasing Borate inclusion between 2.5 and 2.55 Å. Also demonstrates the formation of a peak at 2.4 Åwhich is predicted to be $Ca_3(BO_3)_2$

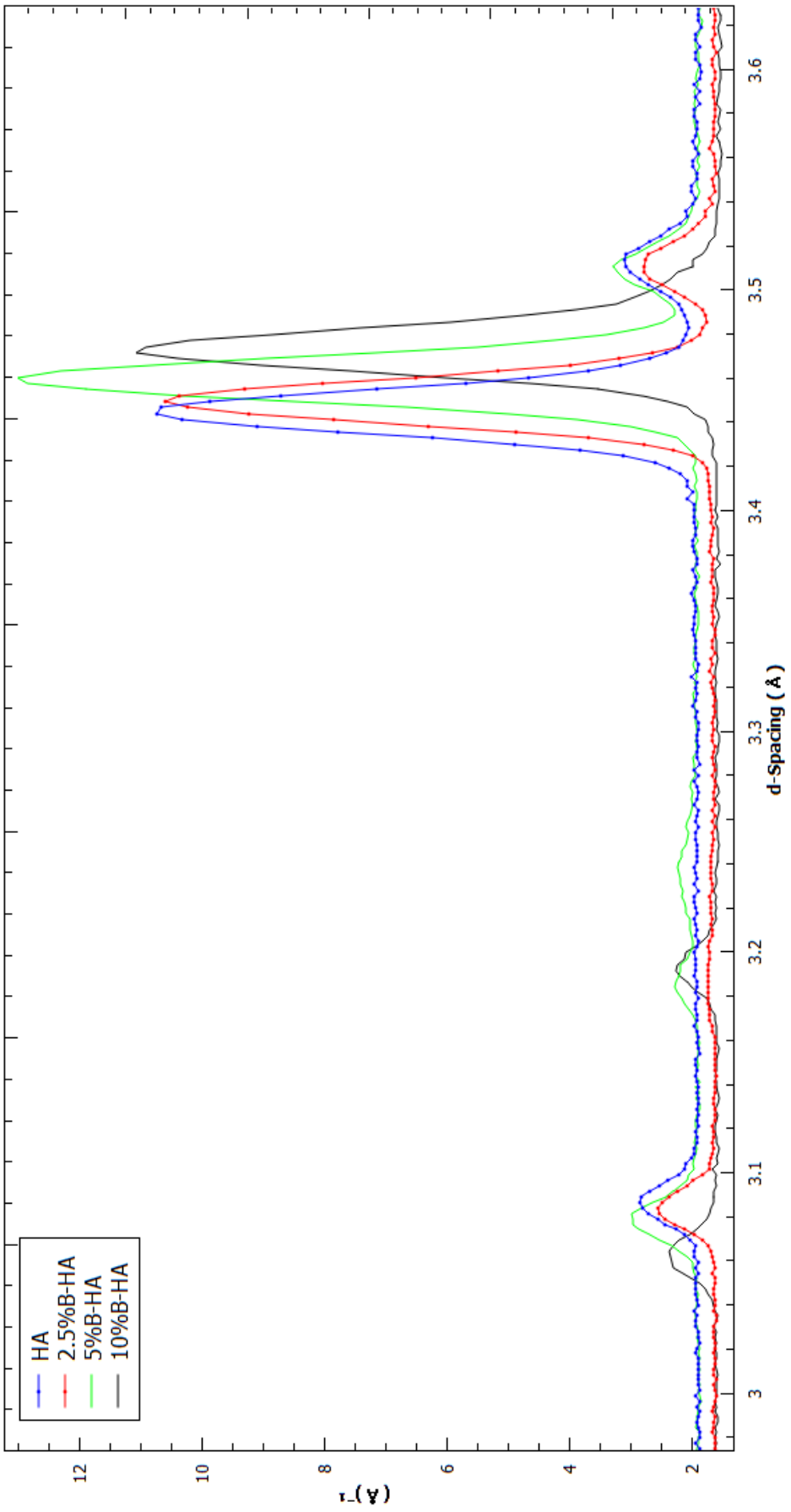


FIGURE 5.20: Neutron Beam diffraction traces for 3 Borate containing samples and 1 baseline HA sample.Highlighting the peak shifts seen with increasing Borate inclusion between 2.5 and 3.6 Ådemonstrating d-spacings for reflections to both be increasing and decreasing depending on the reflection. Also of note is the sudden loss of a peak at 3.51 Å

5.2 Foams

This section presents the results for the preparation of materials for foaming, and the characterisation (physically and chemically) of those foams.

5.2.1 Foam Trial Methods

A series of foams were initially produced to scope a best practice for reproducible ease of foam production. These structures were characterised after firing at both 1100 and 1200 °C by BET and cytocompatability by cell culture (presented in section 5.3.1). Surface area data shows that foams fired at 1100 °C there is a distinct difference in the surface area This is shown in figure 5.21. Variations are seen between samples prepared from material that had been pre-fired at 1100 °C, and samples prepared with material that had either not yet been fired, or had only been fired at 600 °C. This variation is not seen across samples fired at 1200 °C.

5.2.2 Mx-HA Powder Slurry

To better understand the variation in the foam structure found between samples when using different substituted materials, the base powders and their slurries then several parameters were measured. Namely: zeta potential, particle size, and rheological handling (when in a 40 wt.% slurry with 5 wt.% PVA). Two sets of data have been generated to compare the material before and after firing.

The tables (Table 5.4 for the precipitated material, and repeated in table 5.5 for the fired samples) show a summary of the data gathered, with representative plots of trends in their zeta potential in figure 5.22, figure 5.23, figure 5.24, and figure 5.25. Zeta potential data was generated using a 3 wt.% slurry that was mechanically agitated during measurement, thereby removing the need to form a stable suspension. This data demonstrates that in an unfired state the HA powders behave as expected for an inorganic powder with zeta values rising with a reduction in pH, and reducing with an increase in pH. The magnitude of the zeta potentials is rarely in excess of ± 20 mV meaning that the powders would not form a stable suspension on their own and are likely to rapidly flocculate. After firing the zeta profile changes to be quite unusual, as the zeta potential decreases with a drop in pH, and increases with an increase in pH. This is the opposite of the expected behaviour and is hypothesised to be due to K^+ adhesion to the powder surface.

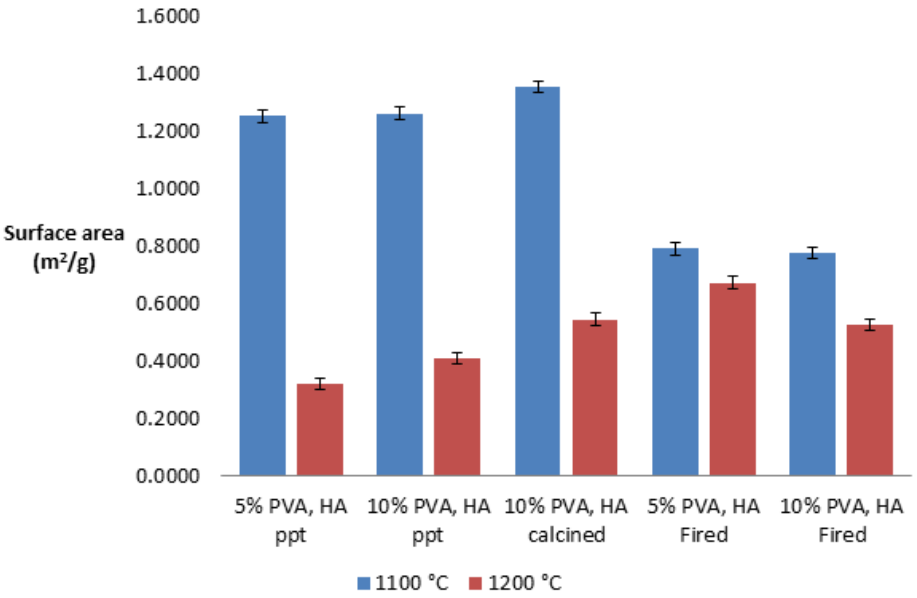


FIGURE 5.21: Surface area of 10 foams after firing, split into 5 groups relating to the method of production. The samples which used un-sintered material demonstrated a higher surface area when fired at 1100 °C, whereas at 1200 °C all samples showed reduced surface area. Error values for the BET kit are determined to be $\pm\ 0.02\,\mathrm{m}^2\,\mathrm{g}^{-1}$.

TABLE 5.4: Table of the precipitate Mx-HA powders showing the range of pH values, and the associated zeta reading when a 3 wt.% suspension was made in deionised water and placed into a zeta probe.

Sample	**Substitution**	**Initial pH**	**Initial Zeta (mV)**	**Zeta at pH 4 (mV)**	**Zeta at pH 12 (mV)**	**Isoelectric point ($\sim$ pH)**
Sr,Si-HA	Si, Sr	7.06	9.83	18.62	-3.39	11.5
Si,S-HA	Si, S	7.54	3.32	18.03	-20.67	10
Sr,B-HA	Sr, B	7.21	18.08	35.80	14.51	N/A
Sr,S-HA	Sr, S	6.75	11.82	34.06	-5.92	11.5
Si,B-HA	Si, B	7.12	5.78	21.13	-8.74	10
S,B-HA	S, B	7.04	3.06	18.23	-10.23	9
Sr,Si-HA r.r.	Sr, Si	6.18	4.43	19.32	-1.43	11.5
Si-HA	Si	9.15	2.32	19.36	-5.93	10
HA	HA	7.34	3.1	15.73	-9.61	8.5

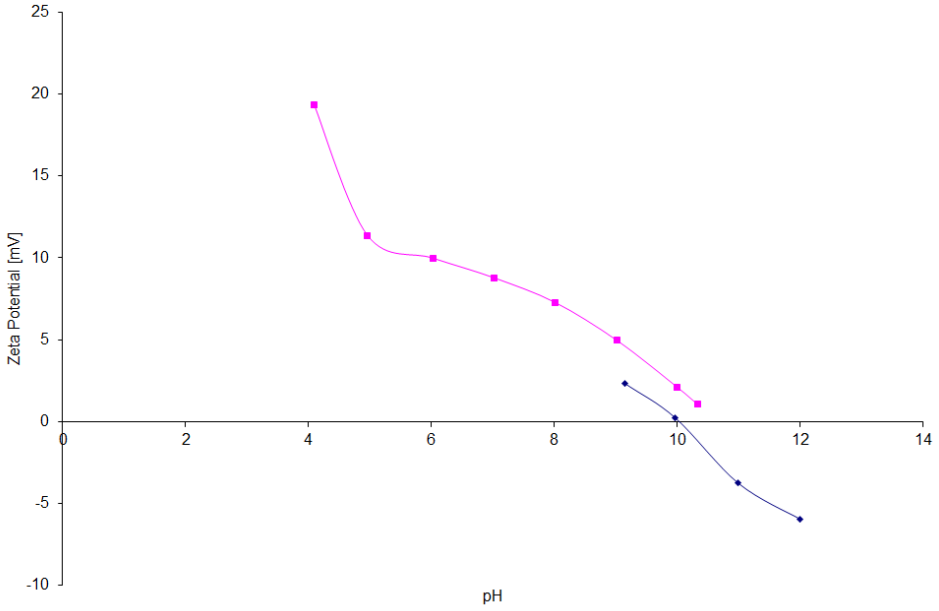


FIGURE 5.22: Zeta vs pH for sample Si-HA. The blue line demonstrates the basic pH sweep up to 12, with the pink line showing the acidic sweep down to pH 4. The isoelectric point is the averae of where the two lines cross the x-axis.

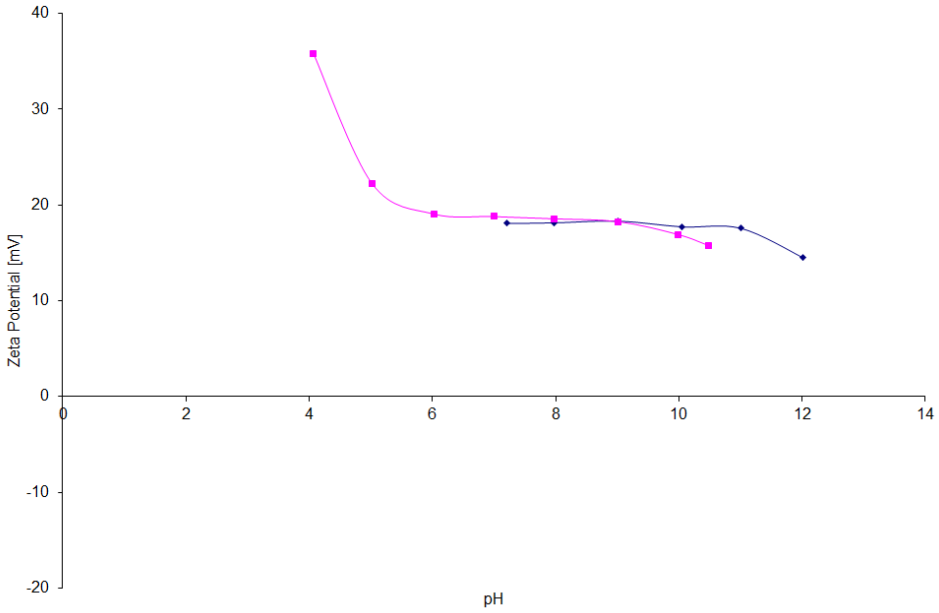


FIGURE 5.23: Zeta vs pH for Sr,B-HA precipitate. The curve is regular in appearance, but is moved positively by 20 mV.

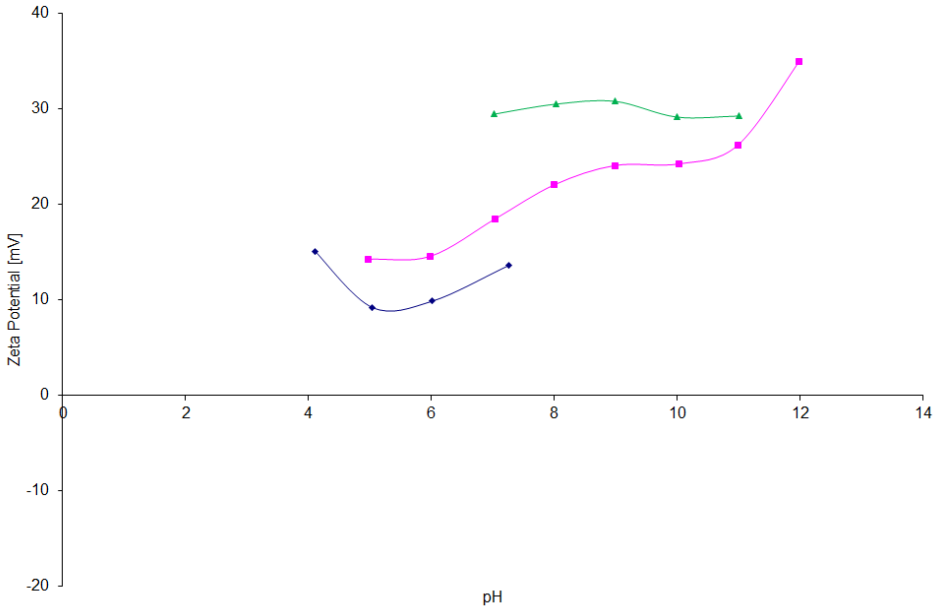


FIGURE 5.24: Zeta vs pH for Si,S-HA fired material. The form of the graph is similar to that expected (as seen in 5.22), but inverted. The order of the pH sweeps is blue -> pink -> green which shows the possible adhesion of K^+ as it is not removed by the second acid addition.

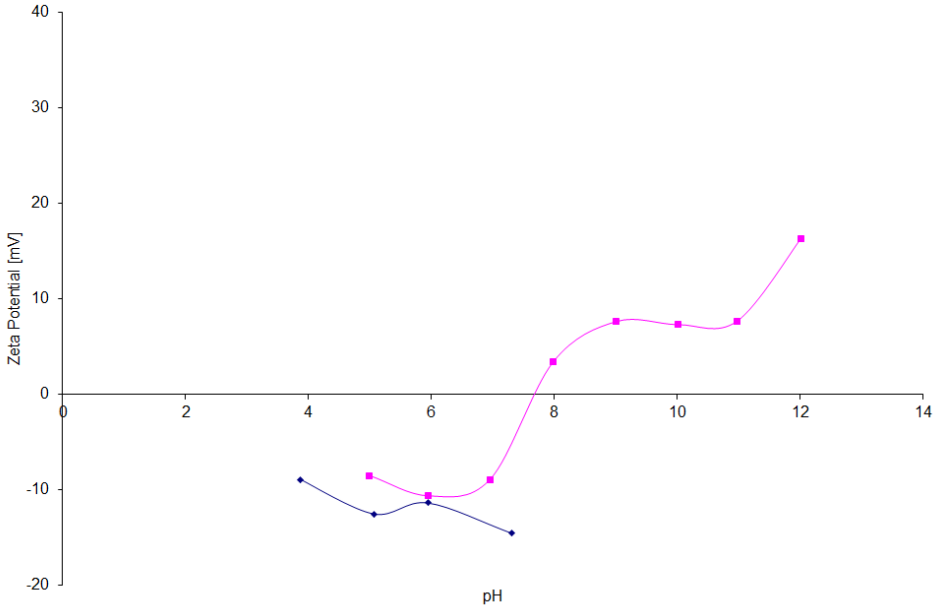


FIGURE 5.25: Zeta vs pH for Si,Sr-HA fired showing the same for as the other fired materials (i.e. the opposite to expected), but with the negative starting zeta.

TABLE 5.5: Table of the fired Mx-HA powders showing the range of pH values, and the associated zeta reading when a 3 wt.% suspension was made in deionised water and placed into a zeta probe.

Sample	**Substitution**	**Initial pH**	**Initial Zeta (mV)**	**Zeta at pH 4 (mV)**	**Zeta at pH 12 (mV)**	**Isoelectric point ($\sim$ pH)**
Sr,Si-HA	Si, Sr	7.31	-14.58	-8.94	16.31	7.5
Si,S-HA	Si, S	7.26	13.61	15.05	34.96	N/A
Sr,B-HA	Sr, B	8.12	4.14	5	18.6	N/A
Sr,S-HA	Sr, S	7.41	6.91	7.25	20.02	N/A
Si,B-HA	Si, B	7.64	3.62	4.38	20.95	N/A
S,B-HA	S, B	7.15	12.48	10.57	24.9	N/A
Sr,Si-HA r.r.	Sr, Si	7.62	11.37	5.52	23.48	N/A
Si-HA	Si	7.82	7.86	7.79	19.45	N/A
HA	HA	7.56	7.54	6.46	17.89	N/A

5.2.3 Mx-HA Foam Physical Characterisation

After firing the foamed Mx-HA samples, they were characterised physically by SEM, Zeta, Mercury Intrusion and BET. Table 5.6 summarises with a typical example of Mercury intrusion shown in figure 5.26. The data shows no obvious binary trends (i.e. between two factors), although all samples do demonstrate similar levels of porosity (54 - 75 %), pore sizes, and surface area (1.50 - 3.04 $\mathrm{m}^2\,\mathrm{g}^{-1}$) suggesting that as a test platform for the chemistries investigated they are suitable.

All foams were characterised by SEM at magnifications of x20, x100, x1000, and x4000. These are all displayed below in figures 5.30, 5.28, 5.29, 5.30, 5.31, 5.32, 5.33, 5.34, and 5.35.

TABLE 5.6: Overview of mercury intrusion and BET data for all Mx-HA foams showing the range of porosities and surface areas seen. All porosities fall within a 20% range, and the surface areas show a range of $1.5\,\mathrm{m^2\,g^{-1}}$. Error values for the BET kit are determined to be $\pm\,0.02\,\mathrm{m^2\,g^{-1}}$

Sample	**Substitution**	**Total Intrusion Volume** ($\mathrm{ml\,g^{-1}}$)	**Total >1** µm ($\mathrm{ml\,g^{-1}}$)	**Total <1** µm ($\mathrm{ml\,g^{-1}}$)	**Ratio of pore volume below** $1\,\mu\mathrm{m}$ **and greater than** $1\,\mu\mathrm{m}$	**Total Porosity (%)**	**Multipoint surface area** ($\mathrm{m^2\,g^{-1}}$)
Sr,Si-HA	Si, Sr	0.6	0.3394	0.2606	1.302	65.02	2.4374
Si,S-HA	Si, S	0.7926	0.4872	0.3054	1.595	61.76	3.0347
Sr,B-HA	Sr, B	0.4817	0.4133	0.0684	6.042	57.76	1.773
Sr,S-HA	Sr, S	0.5286	0.3732	0.1554	2.402	61.25	1.6247
Si,B-HA	Si, B	0.4065	0.3048	0.1017	2.997	54.78	1.5356
S,B-HA	S, B	0.9268	0.5734	0.3534	1.623	74.02	2.1653
Sr,Si-HA r.r.	Sr, Si	0.9459	0.5417	0.4042	1.340	70.62	2.8461
Si-HA	Si	0.6223	0.4002	0.2221	1.802	63.43	2.2833
HA	HA	0.7282	0.5381	0.1901	2.831	68.94	1.7733

TABLE 5.7: Chemical composition (in wt.%) of all multi-substituted hydroxyapatite foams and baselines fired at 1120 °C as determined by XRF, ICP-OES, and LECO. Errors are calculated to be 1% relative, or 0.05 wt.%, whichever is larger

Experiment	**CaO**	**P_2O_5**	**SrO**	**MgO**	**SiO_2**	**B_2O_3**	**S**
Sr,Si-HA	53.3	39.9	3.39	0.42	2.00	0.00	0.00
Si,S-HA	54.3	39.6	0.02	0.42	1.92	0.00	0.98
Sr,B-HA	53.9	40.5	3.42	0.42	0.07	1.16	0.00
Sr,S-HA	53.0	40.0	3.36	0.41	0.08	0.00	0.99
Si,B-HA	56.3	38.6	0.03	0.43	1.96	1.19	0.00
S,B-HA	55.2	40.3	0.02	0.42	0.05	1.14	1.02
Sr,Si-HA r.r.	54.1	38.8	1.55	0.42	2.00	0.00	0.00
Si-HA	57.2	38.4	0.02	0.44	1.99	0.00	0.00
HA	55.5	42.2	0.02	0.43	0.06	0.00	0.00

5.2.4 Mx-HA Chemical and Crystallographic Characterisation

After firing, the samples were characterised chemically and for their crystallographic nature. The various substitutions demonstrated a range of total crystallinities when fired at 1100 °C (figure 5.36), even with a cation:anion ratio in the targeted range. Two samples (Si,S-HA and S,B-HA) showed a cation:anion ratio below the target (nominally 1.667), and two (Sr,Si rr-HA and Si-HA) showed a cation:anion ratio above the target. The full composition (table 5.7) and crystal phase (table 5.8) data is supplied below. The XRD traces used to generate the data presented in the below graphs and tables is shown in figures 5.37 and 5.39. Enlargements of the traces are presented in figures 5.38 and 5.40. The XRD traces demonstrate low levels of amorphous content (as shown by the sharp peaks) with minimal secondary phase formation - except in the case of the two samples with low Ca:P ratios (Si,S-HA and S,B-HA at Ca:P ratios of 1.581 and 1.570 respectively).

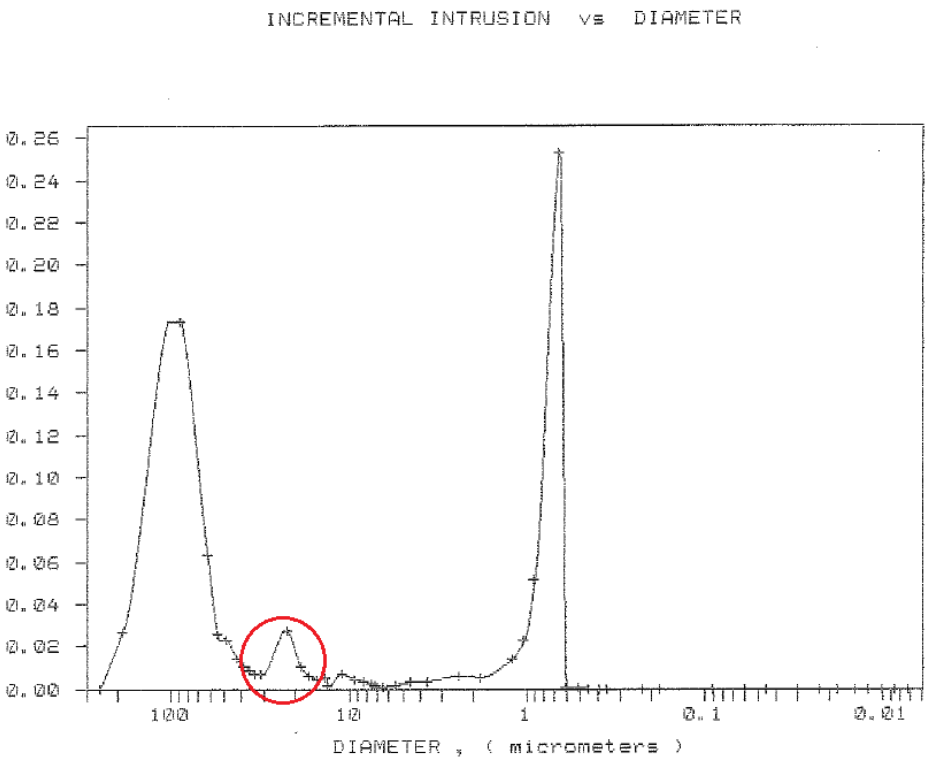


FIGURE 5.26: Example plot of Mercury intrusion with respect to pore diameter for sample D (Sr,S-HA) showing 3 distinct sized pores - main pores at $30 - 200\,\mu m$, connecting pores at $15 - 20\,\mu m$ (highlighted by a red ring), and wall pores at $0.6 - 1.1\,\mu m$.

TABLE 5.8: Crystalline composition (in wt.%) of all multi-substituted hydroxyapatite foams and baselines fired at 1120 °C as determined by XRD. Errors are assumed at 5%

Experiment	HA	β-TCP	α-TCP	Amorphous	Other	Phase
Sr,Si-HA	88.2	0.0	0.0	11.5	0.3	MgO
Si,S-HA	52.0	37.0	0.0	11.1	0.0	
Sr,B-HA	69.6	0.0	0.0	29.6	0.5	CaO
					0.5	MgO
Sr,S-HA	91.1	4.3	0.0	4.3	0.3	MgO
Si,B-HA	78.0	0.0	0.0	21.5	0.2	CaO
					0.4	MgO
S,B-HA	71.3	21.1	0.0	7.5	0.0	
Sr,Si-HA r.r.	86.0	8.4	0.0	5.4	0.3	MgO
Si-HA	78.0	0.0	0.0	19.1	2.6	CaO
					0.3	MgO
HA	82.0	3.1	0.0	14.7	0.3	MgO

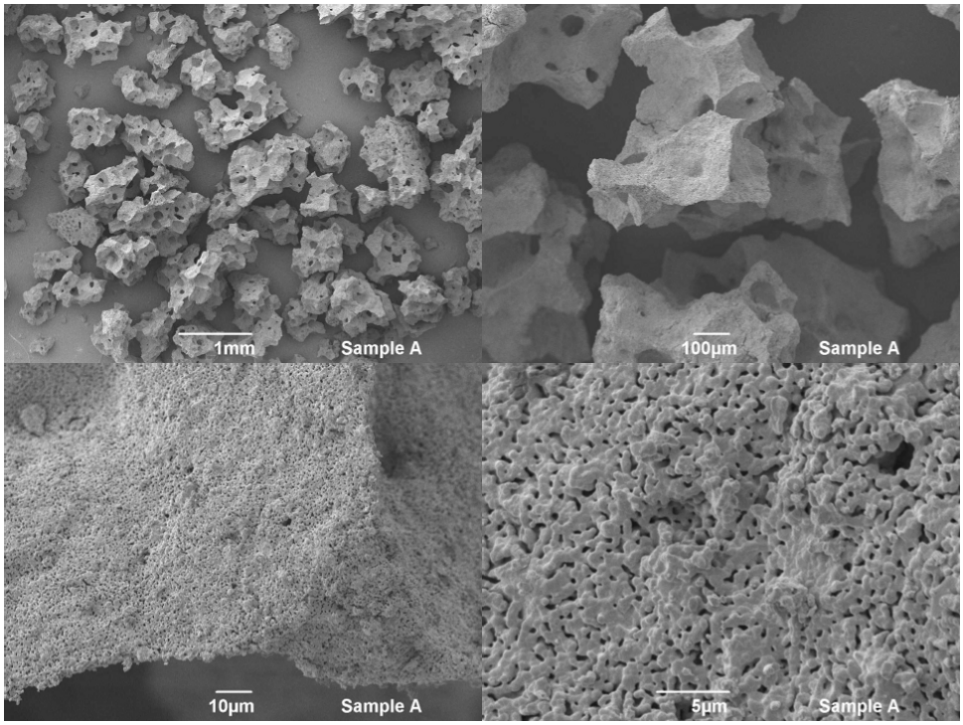


FIGURE 5.27: A series of SEM images for as produced Sr,Si-HA foam.

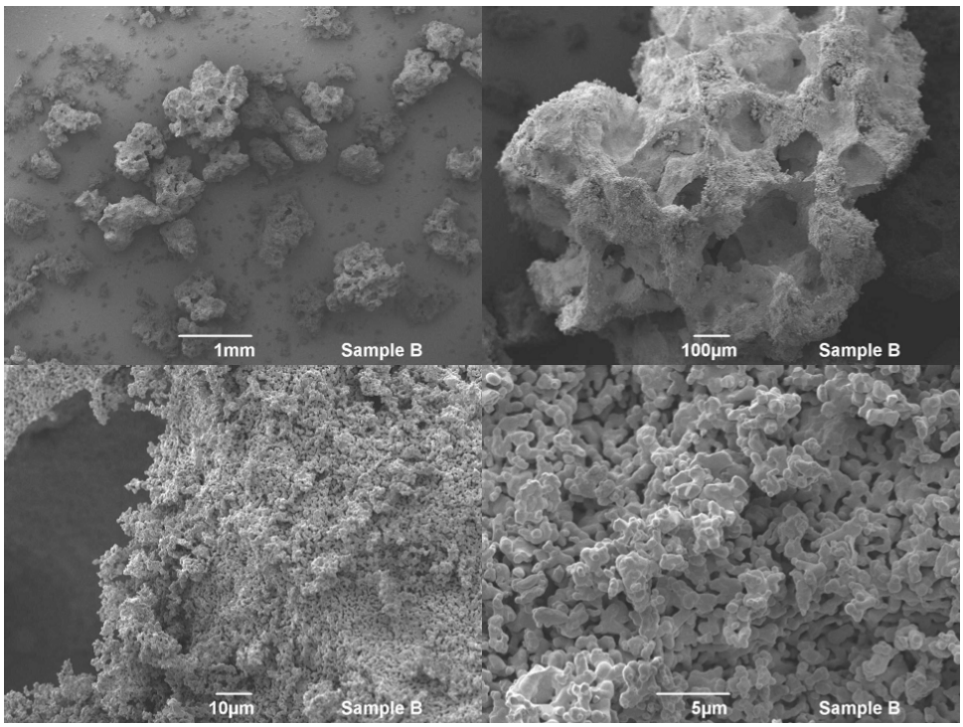


FIGURE 5.28: A series of SEM images for as produced Si,S-HA foam.

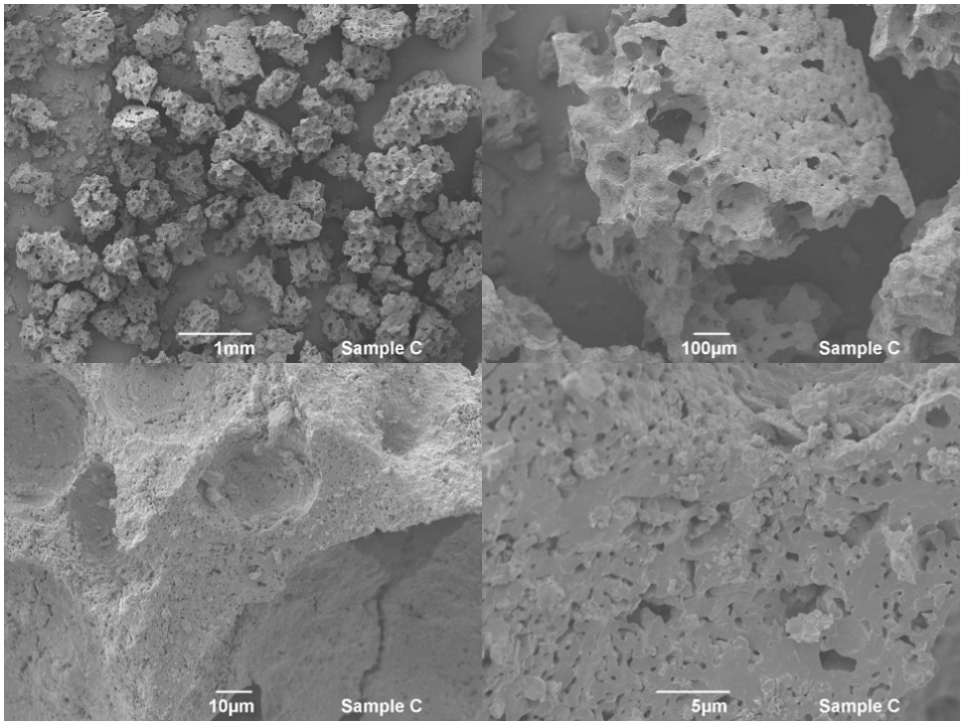


FIGURE 5.29: A series of SEM images for as produced Sr,B-HA foam.

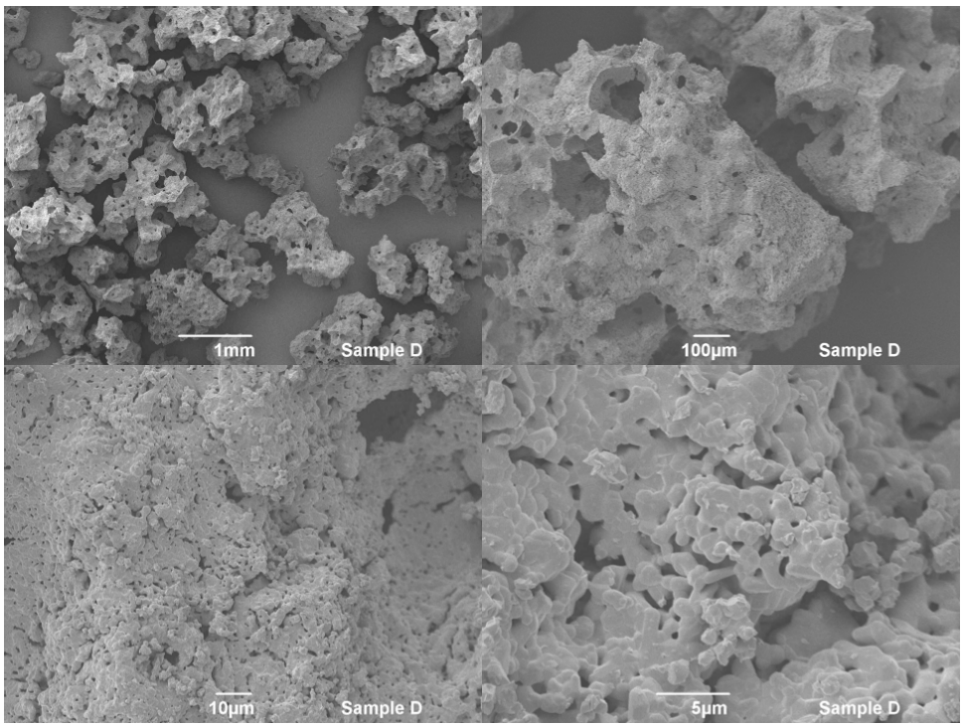


FIGURE 5.30: A series of SEM images for as produced Sr,S-HA foam.

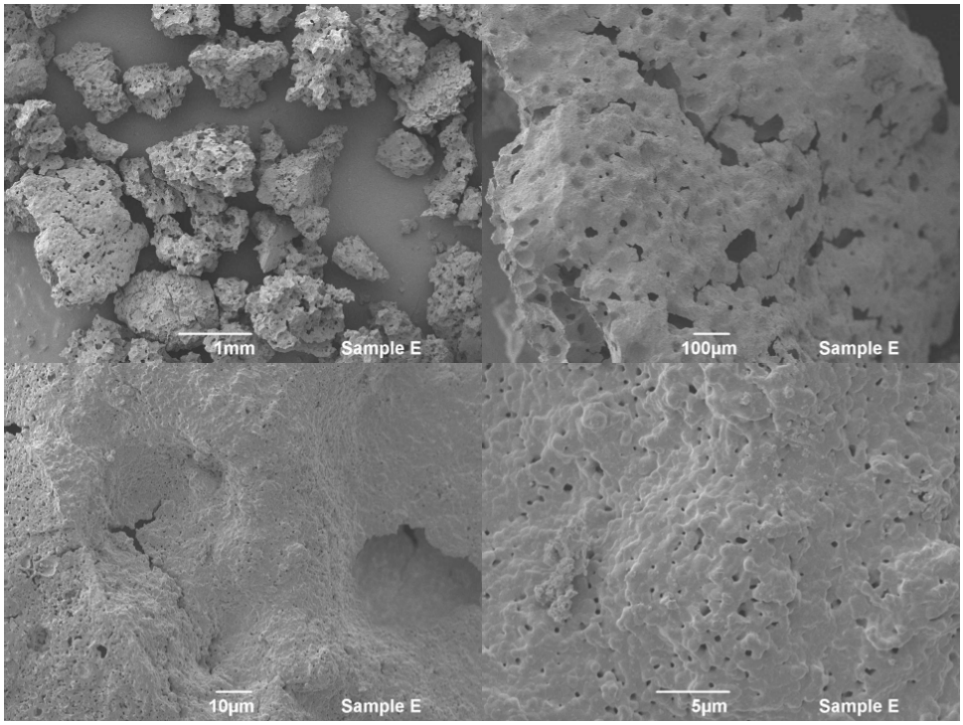


FIGURE 5.31: A series of SEM images for as produced Si,B-HA foam.

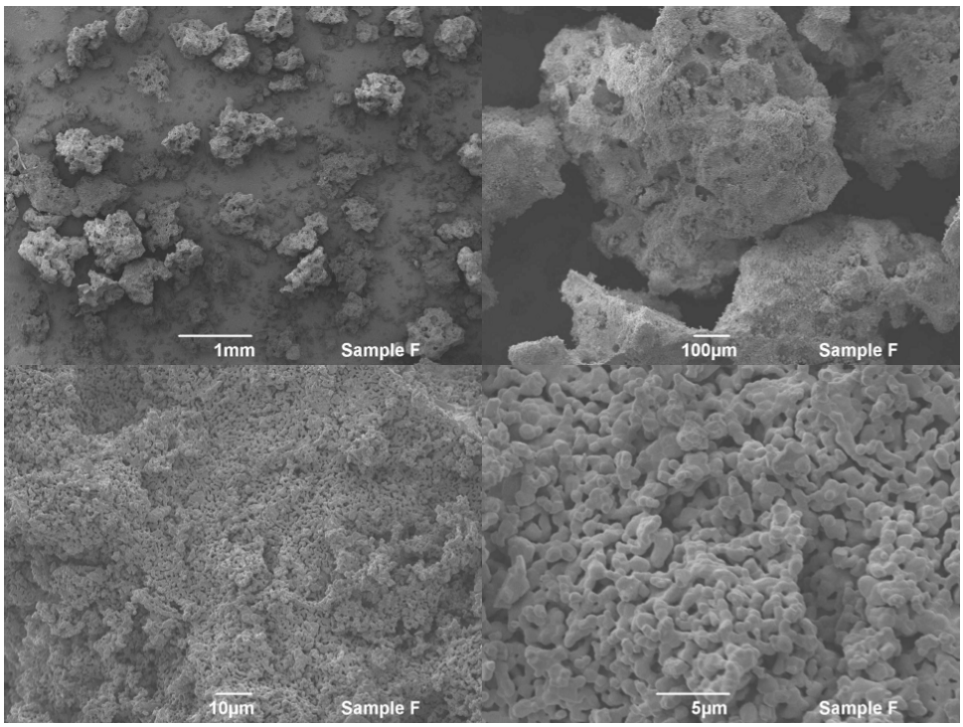


FIGURE 5.32: A series of SEM images for as produced S,B-HA foam.

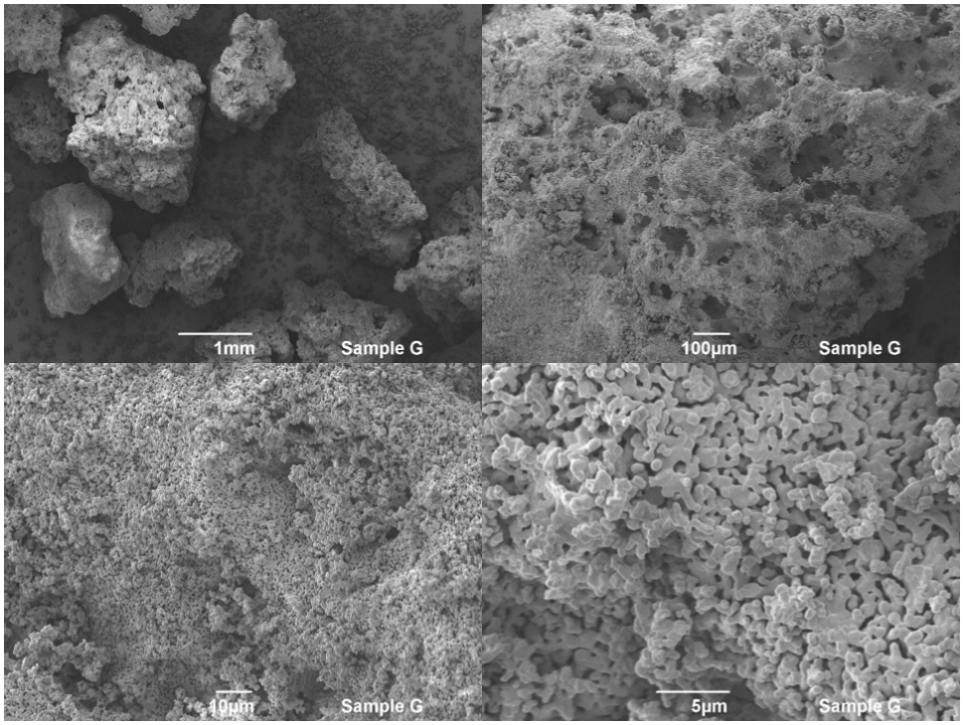


FIGURE 5.33: A series of SEM images for as produced Sr,Si-HA r.r. foam.

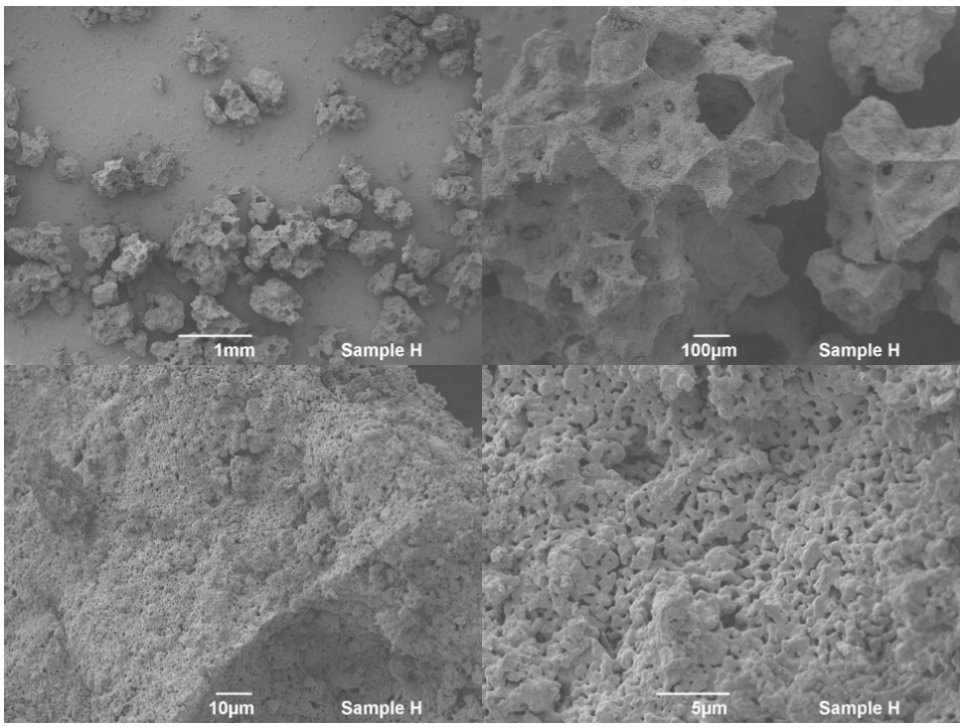


FIGURE 5.34: A series of SEM images for as produced Si-HA foam.

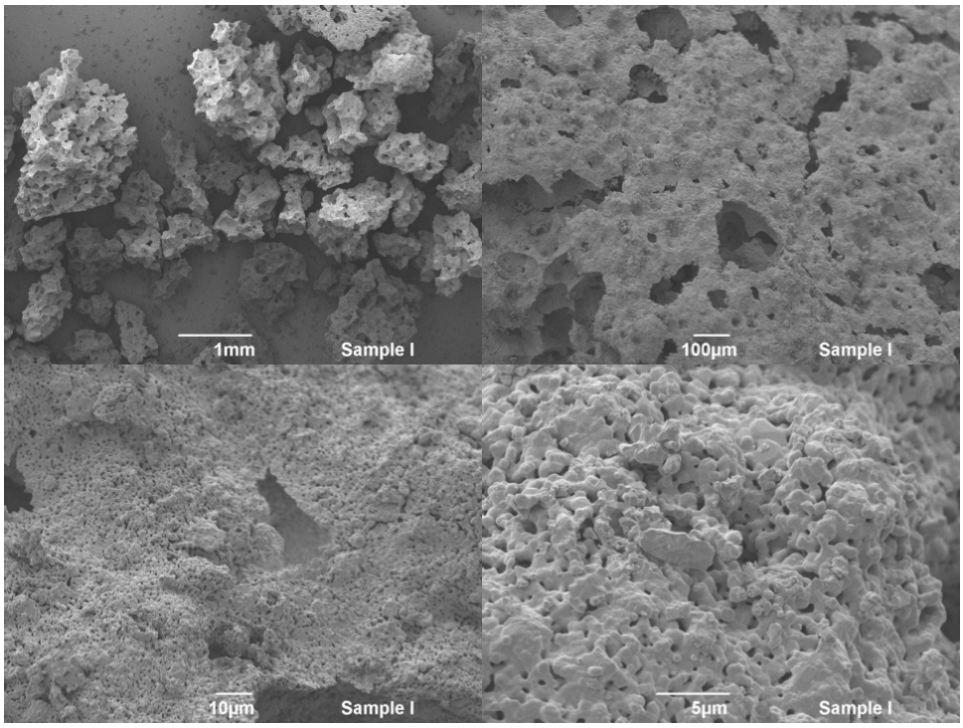


FIGURE 5.35: A series of SEM images for as produced HA foam.

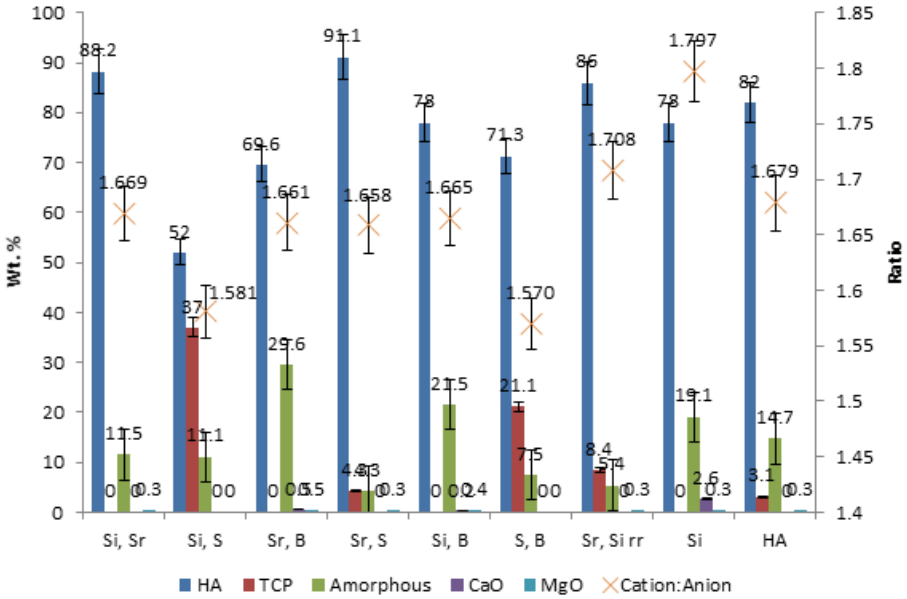


FIGURE 5.36: Graph showing the different crystalline phases formed by the synthesis, as well as the total cation-to-anion ratio of each sample. The left hand y-axis corresponds to the wt.% of each crystalline phase (the bar plots), whilst the right hand y-axis corresponds to the atomic ratio of cation-to-anion (the crosses). Errors on phase compositions are 5% relative for each phase, and 5% actual for amorphous as described in section 4.4.5

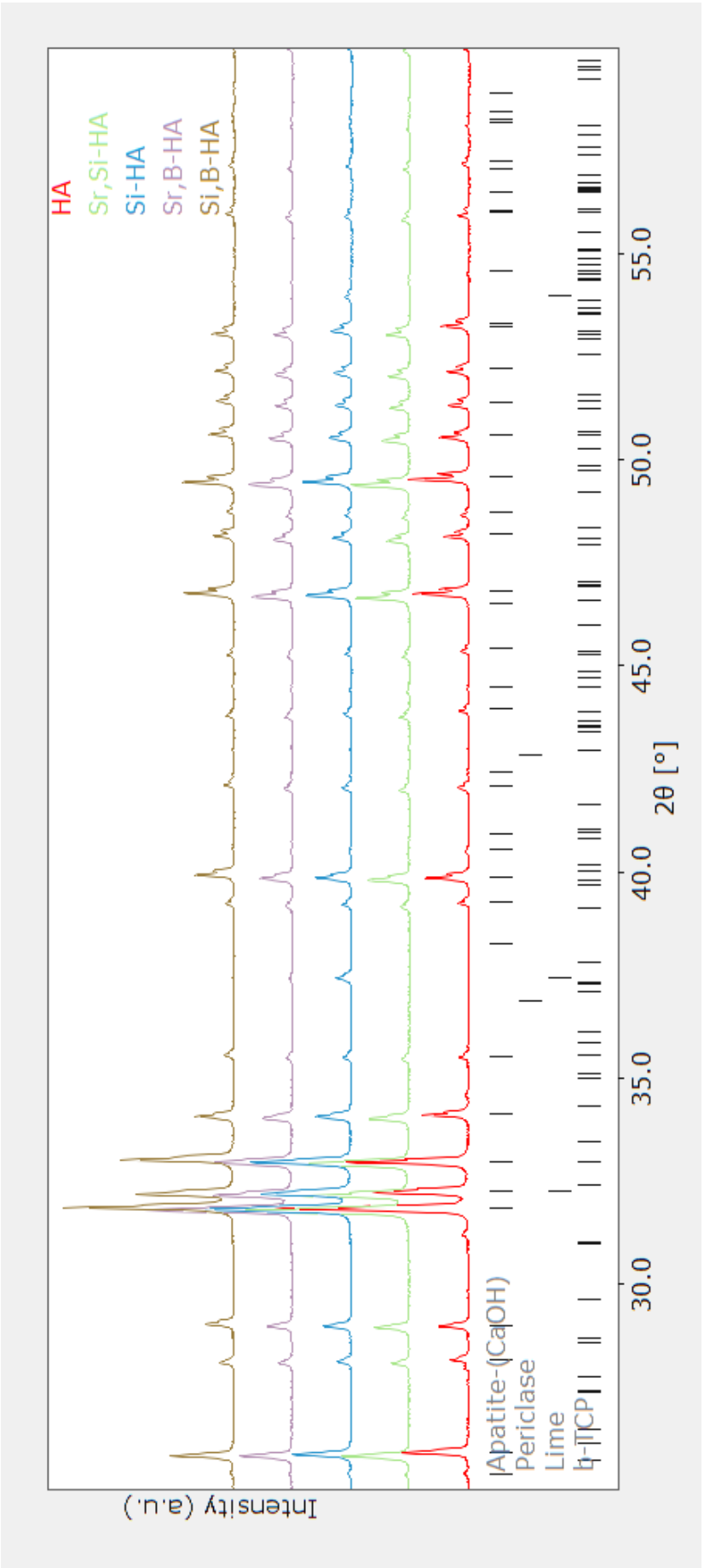


FIGURE 5.37: XRD traces for the first 3 Mx-HA samples along with the baseline HA and 1.8%Si-HA samples. Although the range 25-60 2Θ is very crowded, this area gives the most quantifiable detail and is interpreted by software.

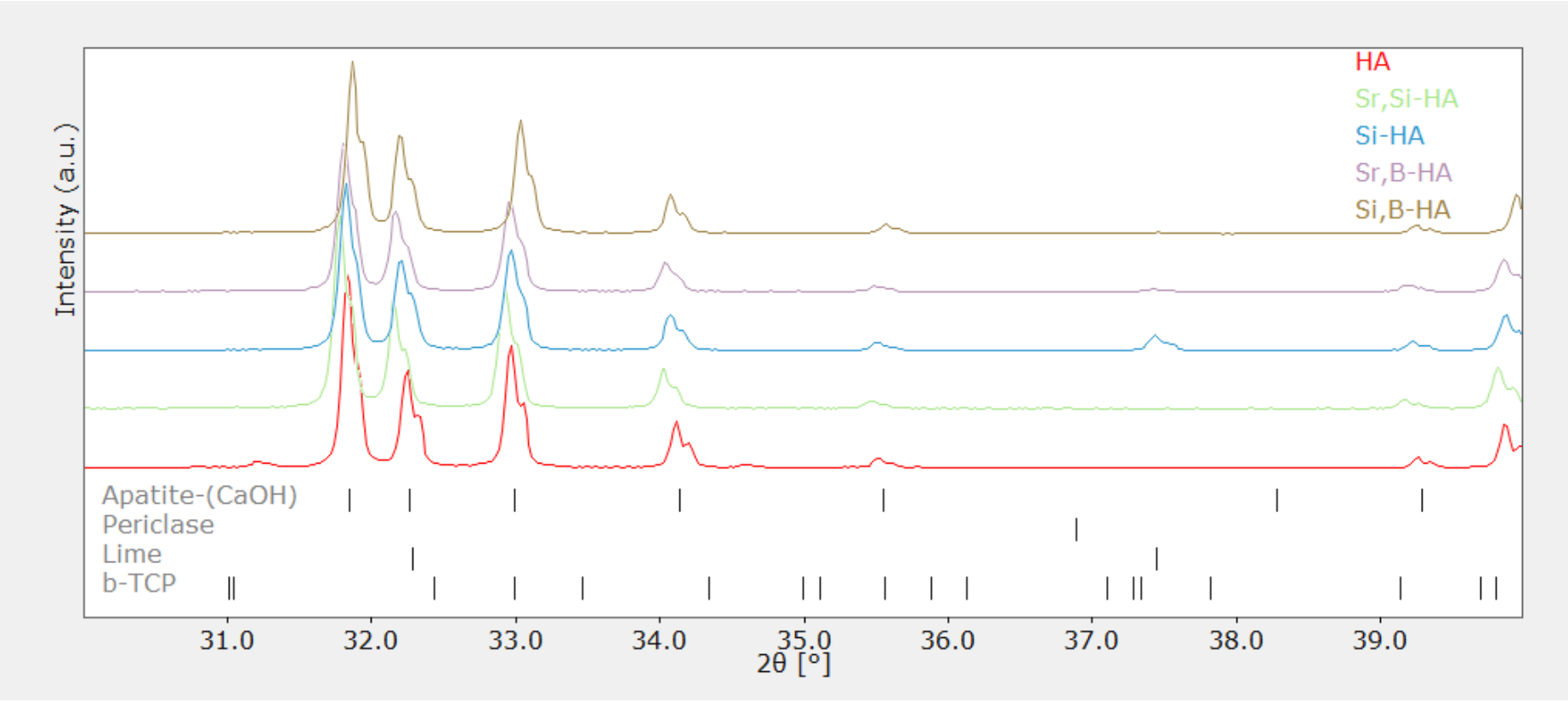


FIGURE 5.38: XRD traces for the first 3 Mx-HA samples along with the baseline HA and 1.8%Si-HA samples. Traces enlarged to show the range of 30 - 40 2θ.

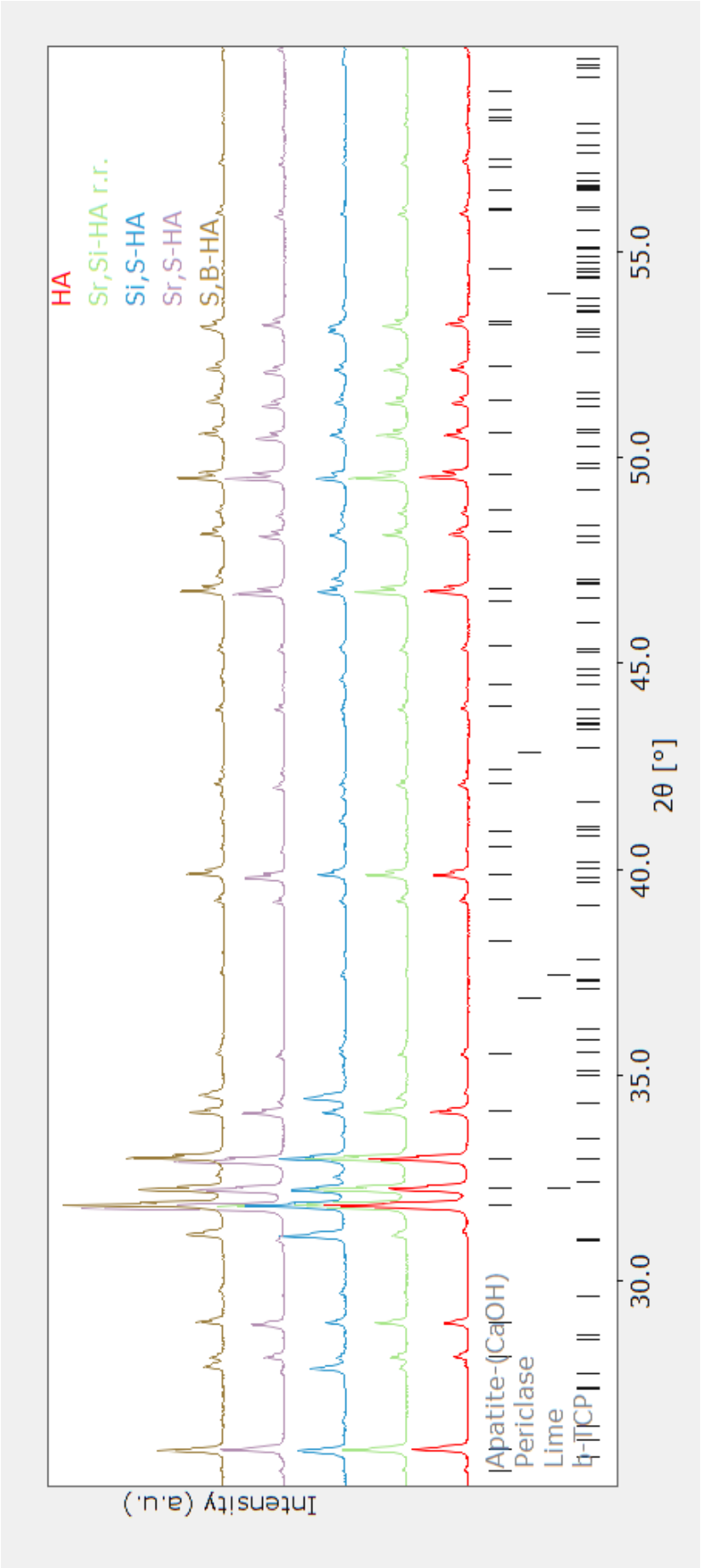


FIGURE 5.39: XRD traces for the final 4 Mx-HA samples along with the baseline HA sample. Although the range 25-60 2Θ is very crowded, this area gives the most quantifiable detail and is interpreted by software.

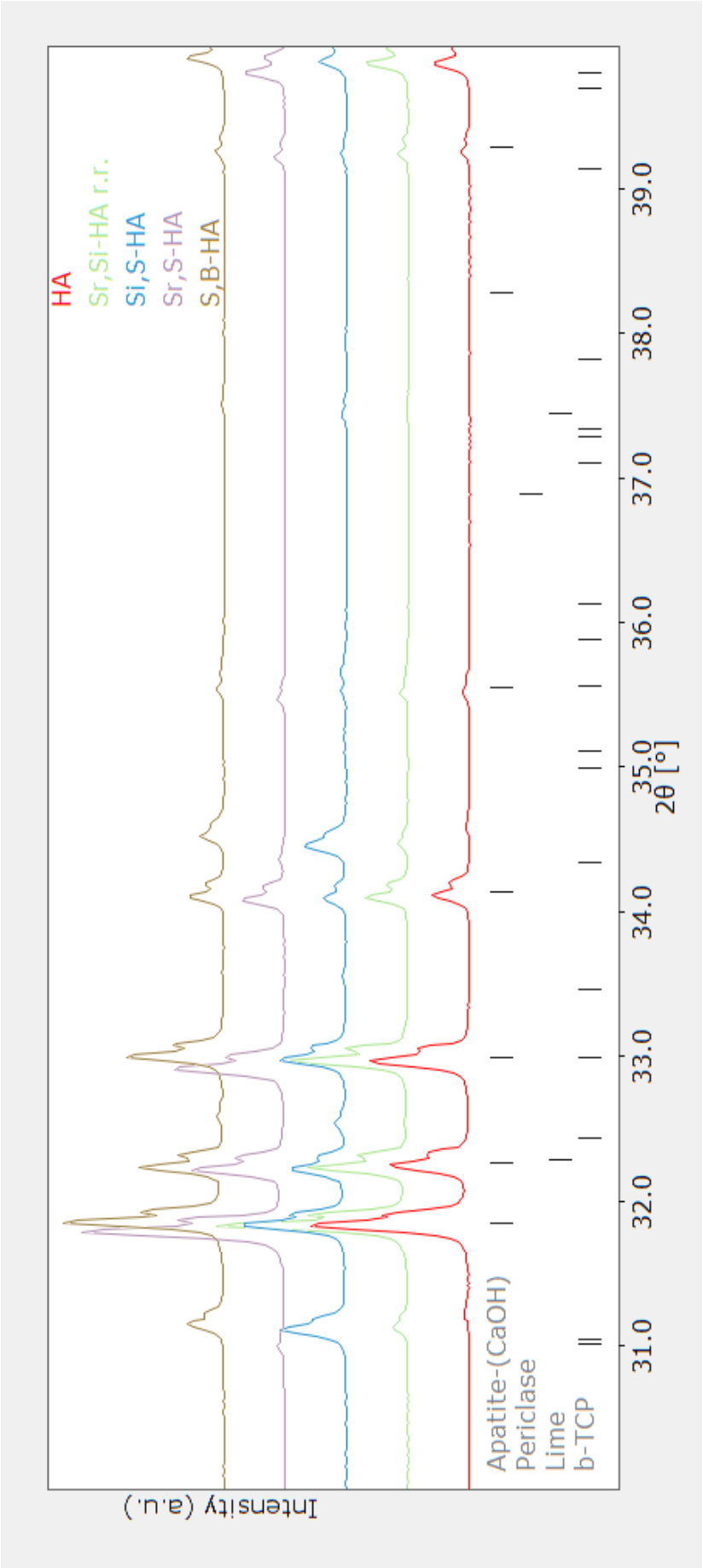


FIGURE 5.40: XRD traces for the final 4 Mx-HA samples along with the baseline HA sample. Traces enlarged to show the range of 30 - 40 2θ.

5.3 Cell Characterisation Data

In addition to the chemical and physical characterisation of materials, samples were tested for their cytocompatability in vitro using MG63 cells to represent an osteoblastic environment. The work was initially carried out to screen the various foaming methods to ensure there was not a particular processing route that gave a preferred or detrimental response, and then to compare the chemistries of the various substituted materials.

5.3.1 HA Foam Trial Characterisation

As an initial screen to ensure that different processing routes to a foamed structure did not give a significantly better or worse cell response, the ten (10) foams of the same chemistry were tested for up to 6 days with Alamar Blue to check cytocompatability. The samples used covered a range of PVA concentrations, thermal history conditions, and final sintering temperatures. As can be seen in the data (figure 5.41) the foams show similar levels of metabolic activity across all samples. Day 3 data is quite varied when considering the error bars, although by day 6 well-to-well variation is reduced.

5.3.2 Mx-HA Foam Characterisation

With a fixed foam processing method, the different substitutions and associated controls (Si-HA, and HA) were trialled. Initial cell results were generated, with trends confirmed by a repeat run carried out by MPhil students (Katie Bostock, Zheng Zhiqiang) under the supervision of Dr. Colin Scotchford. Samples were characterised by Alamar Blue (figure 5.42) and DNA concentration (via a Hoechst stain, figure 5.43). Significant ($p < 0.05$) differences are found in metabolic activity of separate samples, as per Alamar Blue results, but there is only one significant difference between samples with respect to DNA concentration. Whilst there is a significant difference between the metabolic activity of samples, it is not considered to be an important difference. The metabolic rate divided by DNA count was used as a measure of individual cell activity (figure 5.44). When the samples are normalised in this way, it is shown that there are no significant differences between samples at day 21. The marker used for osteo-activity was osteocalcin. Osteocalcin production for days 14 and 21 (figure 5.45) was shown to be relatively low across all samples, except for the Sr,S-substituted material

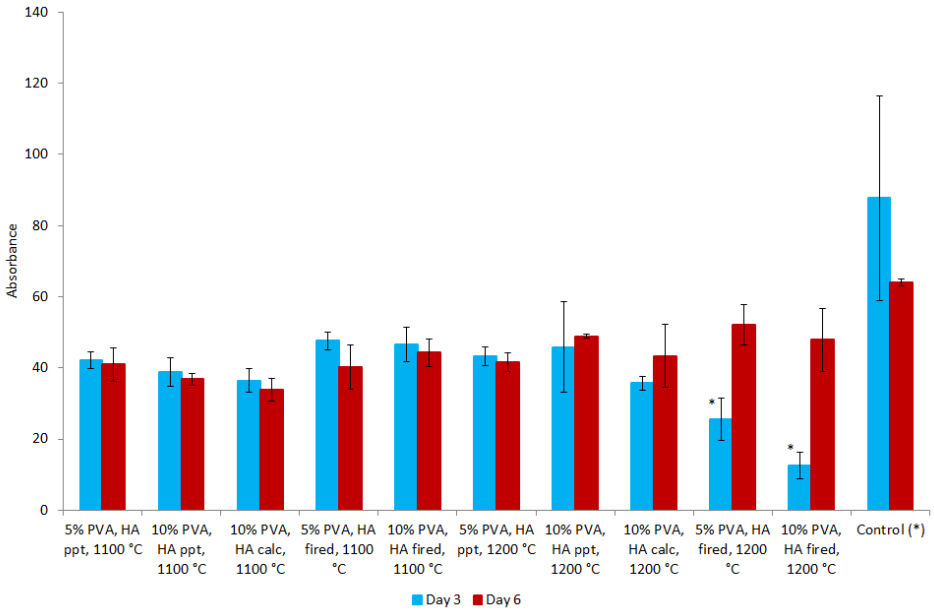


FIGURE 5.41: Day 3 and 6 Alamar Blue data demonstrating comparable cytocompatability between samples. Error bars are the standard error of the data (n=4, control n=3). The control was tissue culture plastic. Samples are detailed in section 4.3.4, the y-axis units are arbitrary. Significance of $p < 0.05$ is denoted by a mark above the data correlating with the appropriate sample marked on the axis (i.e. an * on the data shows a significant difference versus the control)

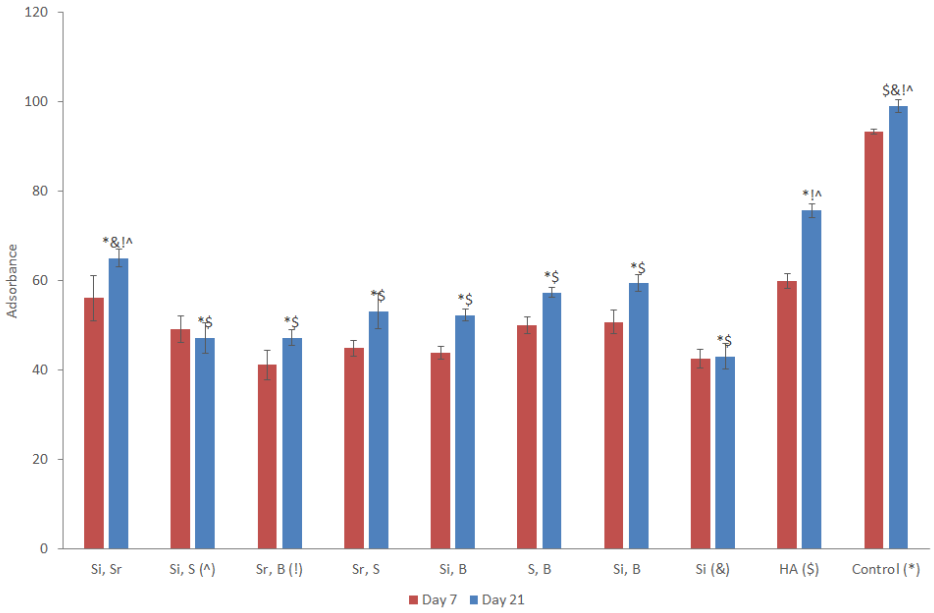


FIGURE 5.42: Day 7 and day 21 Alamar Blue data demonstrating comparable cytocompatability between samples. Error bars are the standard error of the data (n=5, control n=3). The control was tissue culture plastic. Foaming method is detailed in section 4.3.4, and sample composition is detailed in section 5.2.4, the y-axis units are arbitrary. Significance of $p < 0.05$ is denoted by a mark above the data correlating with the appropriate sample marked on the axis (i.e. an * on the data shows a significant difference versus the control)

which demonstrated higher production than any of the controls. This coupled with the equivalent DNA concentrations demonstrates that the Sr,S-HA sample is potentially a more bioactive material than either Actifuse®, or pure HA.

In the below graphs showing cell metabolic activity (figures 5.43 and 5.44) a drop is seen in both cell count, and cell activity as normalised versus cell count. There is no significant difference ($p < 0.05$) between any of the data points, however the observation of a trend on all samples is curious. It is theorised by Dr. Colin Scotchford, based on extensive personal experience with the cell line, that this minor drop may be due to the cells having reached confluence, and therefore their metabolism having slowed down [158]. At this point the author cannot find any literature to either confirm or deny the speculation and therefore leaves it to personal opinion.

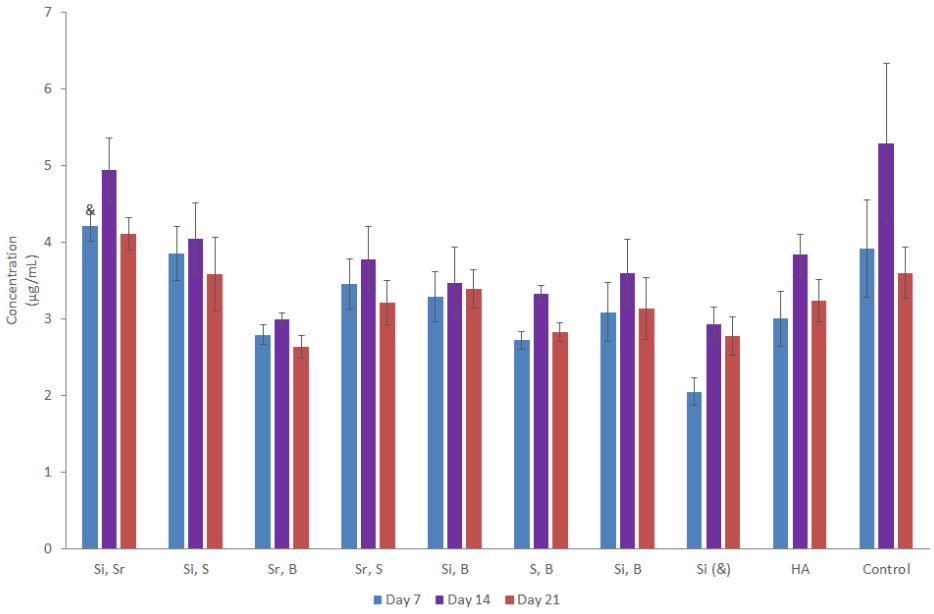


FIGURE 5.43: Day 7, 14, and 21 DNA data demonstrating comparable cell counts between samples. Error bars are the standard error of the data (n=5, control n=3). The control was tissue culture plastic. Foaming method is detailed in section 4.3.4, and sample composition is detailed in section 5.2.4, the y-axis units are $\mu g\,ml^{-1}$. Significance of $p < 0.05$ is denoted by a mark above the data correlating with the appropriate sample marked on the axis (i.e. an * on the data shows a significant difference versus the control)

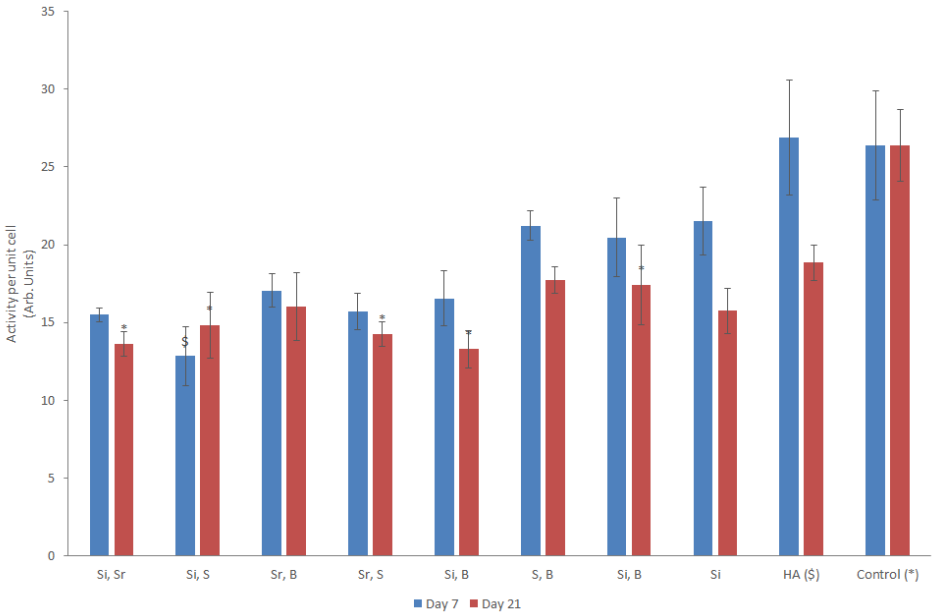


FIGURE 5.44: Metabolic rate normalised versus DNA concentration for all samples at both day 7 and day 21. Error bars are the standard error of the data (n=5, control n=3). The control was tissue culture plastic. Foaming method is detailed in section 4.3.4, and sample composition is detailed in section 5.2.4, the y-axis units are arbitrary. Significance of $p < 0.05$ is denoted by a mark above the data correlating with the appropriate sample marked on the axis (i.e. an * on the data shows a significant difference versus the control)

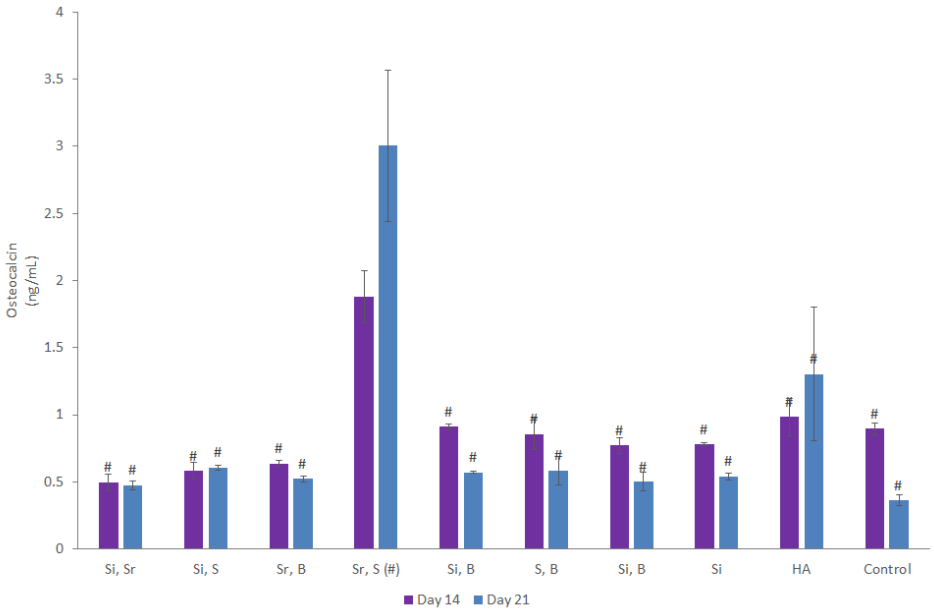


FIGURE 5.45: Day 14 and 21 osteocalcin data demonstrating significant increased production in osteocalcin for Sr,S-substituted hydroxyapatite. Error bars are the standard error of the data (n=3, control n=3). The control was tissue culture plastic. Foaming method is detailed in section 4.3.4, and sample composition is detailed in section 5.2.4, the y-axis units are $\mathrm{ng\,ml^{-1}}$. Significance of $p < 0.05$ is denoted by a mark above the data correlating with the appropriate sample marked on the axis (i.e. an ♯ on the data shows a significant difference versus Sr,S-HA)

6 Discussion

6.1 Introduction

The original aim of the project was to develop and characterise multi-substituted hydroxyapatites for applications in bone replacement devices – particularly bone void fillers. The 3 sub chapters in this discussion chapter cover;

a) the synthesis and characterisation of the base material (6.2)

b) the production and characterisation of usable samples in the form of foams (6.3)

c) the biological characterisation of the samples in vitro (6.4)

The 3 broad topics to be considered are vital when designing a material for a biomaterial – the material, the structure, and the biological response.

6.2 Synthesis of Substituted Hydroxyapatites

The primary objective of the work was to develop a robust synthesis route that can be used for industrially relevant processing such as producing a powder for foaming into a device. In addition the route must lend itself to reproducibility, scalability, and capable of substitution of various elements into the lattice – as opposed to being highly specialised and limited to a single substitution, although it is accepted that slight variations on the method may be required for different substitutions – especially with regards to the firing schedule.

6.2.1 Mono substitution of Hydroxyapatite with Strontium, Borate, and Sulphate by a wet-chemistry precipitation method

Synthesis of HA materials with the Ca^{2+} and $PO_4{}^{3-}$ sites substituted with a variety of other ions (for example mono substitution with: $CO_3{}^{2-}$, $SiO_4{}^{4-}$, Sr^{2+}, and Mg^{2+} [159]) are well reported. In order to validate a synthesis method a series of experiments were run. The experiments investigated the substitution of Ca^{2+} with Sr^{2+}, and the substitution of $PO_4{}^{3-}$ with $BO_3{}^{3-}$

or $SO_4{}^{2-}$. The $SiO_4{}^{4-}$ ion was excluded from this initial study as the area has been heavily explored by the original group from Queen Mary's University run by Bonfield *et al.* [160]. An important and commercially relevant difference to note between the methods generally used in the literature and that used in this experiment is the requirement of pH control. In research carried out by Hing *et al.* in substituting $SiO_4{}^{4-}$ into the lattice, pH control is used, however in the work investigated here it has been observed that pH control is not needed in the system $Ca(OH)_2$ + H_3PO_4 as the amount of H_3PO_4 added is not enough to neutralise the $Ca(OH)_2$ if the correct ion ratio is used.This is illustrated in Figure 5.5 (section 5.1.2). In the work reported by Hing *et al.* acid is titrated into a stirred mixture of $Ca(OH)_2$ whilst the pH is controlled by co-titration of ammonia.

When adding the acid to the base via an auto syringe, the pH will not drop provided that the addition is slow enough (for example, a 1L synthesis starting with $700\,\mathrm{ml}$ base will work with an addition rate of 6M acid added at $4\,\mathrm{ml\,min^{-1}}$ under vigorous stirring (250 - 350 rpm)). Previous work has also shown that immediate and intimate mixing does lead to pH swings (presumably whilst the various protons and hydroxyl groups dissociate and is therefore a kinetic effect rather than thermodynamic). When considering larger scale reactions for industrial purposes slow titrations are unfavourable due to the long reaction times and chemical engineering considerations such as efficient mixing. Indeed pH control is 'used' in industry in so much as within a larger reactor, a mixing tube where raw $Ca(OH)_2$ and H_3PO_4 are mixed, with the flow rates of both continuously adjusted so that the outflow into the larger tank is maintained at the correct pH (Schematic is shown in figure 6.1). In this case, it is more using pH as an indicator of the correct Ca:P ratio, rather than using the pH to force precipitation of HA.

Thus the largest differences between the method used here and methods of similar precipitations in the literature is the absence of pH control, instead relying on accurate concentrations of reagents and the inherent buffering potential of HA precipitates and excess $Ca(OH)_2$ throughout the precipitation. On the subject of Ca:P ratio required for complete neutralisation of the $Ca(OH)_2$ – the value required is 1.5 which also happens to be the ideal ratio for formation of TCP. Using this knowledge, it is possible to check for a successful synthesis by recording the pH vs time of a reaction to see if all the $Ca(OH)_2$ was neutralised – an event that is easily recognised by the sudden pH drop associated with it (as typified in figure 5.4, section 5.1.2).

Interestingly, the HA present in the mostly amorphous precipitate will then buffer the reaction back up to a higher pH, however the synthesis is already compromised and the low pH environment will have generated seed crystals for the formation of TCP during firing. These seed crystals could be

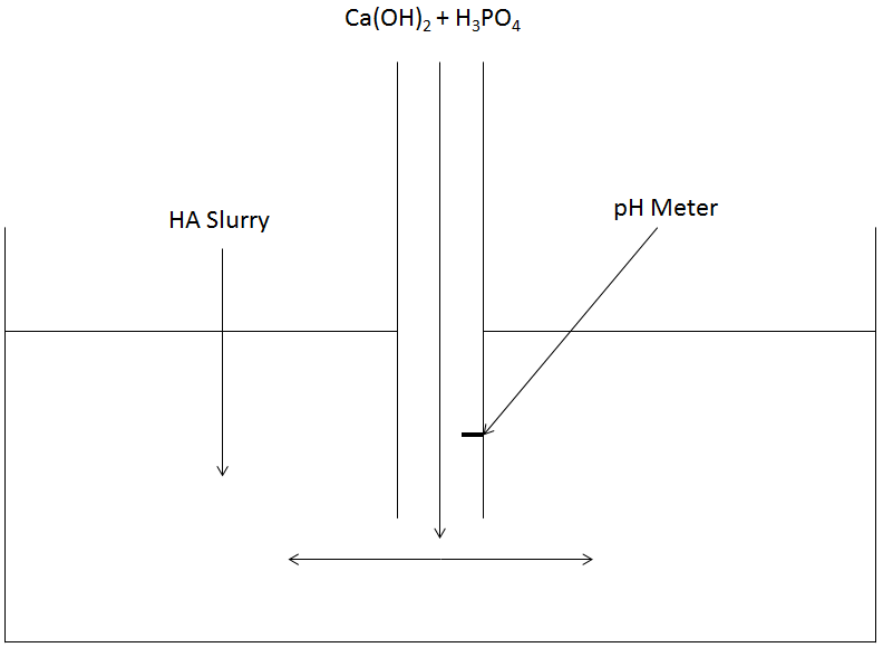


FIGURE 6.1: Schematic of a typical industrial scale HA precipitation reactor. Inputs of concentrated calcium and phosphate sources are individually rate controlled based on feedback from the pH meter in the mixing column. If the pH drops, the calcium is increased/phosphate decreased. If the pH rises, the calcium is decreased/phosphate increased. Design provided by Dr. Stephen Morrey.

various forms – monetite [161], amorphous tricalcium phosphate (ATCP) [162], apatitic tricalcium phosphate/calcium deficient HA [163]. During the mono-substituted HA synthesis in section 4.3.2 the most likely cause of TCP formation is through the generation of monetite in the reaction vessel which can combine with the Ca^{2+} present during firing to produce TCP. ATCP is also possible, and is well reported in the literature [162], however in previous trial experiments carried out at Lucideon Monetite has been found in the samples as-precipitated.

A further difference from the literature is that the inclusion of borate [164, 110, 109, 165] and sulphate are poorly reported, sulphate inclusion is only reported in one paper [115]. When considering the sulphate substitution, the levels attempted are of a similar range to those attempted in the work presented here (max reported is 3.125 mol%), although the levels of crystallinity they report are very low, 89.0 % for pure HA, dropping to 46.8 % for the 3.125 mol% S-HA. The 1.875 mol% S-HA is reported as having only 58.6 % crystallinity. The work reported in this section displays levels of up to 3 mol.% substitution (highest crystallinity 89.3 wt.%), whilst experiments discussed in section 6.2.3 include substitutions up to 4 mol.% (highest crystallinity - 91.1 wt.%). At these low levels of crystallinity, although no TCP or other secondary phases are detected, it is likely that the samples have not received enough heat work to fully consolidate. This is supported by their firing schedule reported – 1000 °C for 6 h. As can be seen from the firing schedule work reported (discussed in section 6.2.4) there is a critical level of heat work required to induce high levels of crystallinity, and it is plausible that 1000 °C is too low for the S-HA material they prepared.

Borate substitution is not seen in comprehensive reviews of substituted HA [159], although there is a number of papers in the public domain about not only the substitution, but also detailed characterisation of the borate site and the effect on human harvested primary MSCs [165]. The standard reported method for borate inclusion is dry milling and solid-state consolidation of reactants – possibly used so as to avoid precipitation of $Ca_3B_2O_6$ as has been encountered in this work. Of particular relevance from the work of Ternane *et al.* where they demonstrate that the inclusion of borate up to 3.125 mol% is possible whilst maintaining a monophasic system, and up to 4.56 mol% is possible within a bi-phasic system with the secondary phase being residual $Ca(OH)_2$ from the starting reagents. The work presented here is in agreement that borate levels of up to 3 mol% can be included without leaving residual reagent phases (although TCP was formed at low levels). Follow up work to produce mono-substituted, isotopically labeled (^{11}B) B-HA for neutron beam analysis also showed high levels of borate substitution were possible without splitting the HA phase into two, albeit

TABLE 6.1: Table demonstrating range of substitutions tested in experiments 4.3.2

Experiment	Substitution	Mol.%
Base-HA	N/A	N/A
5%Sr-HA	Sr^{2+}	5
2.5%Sr-HA	Sr^{2+}	2.5
3%B-HA	${BO_3}^{3-}$	3
1.5%B-HA	${BO_3}^{3-}$	1.5
3%S-HA	${SO_4}^{2-}$	3
1.5%S-HA	${SO_4}^{2-}$	1.5

with the formation of some $Ca_3B_2O_6$ alongside. Initial XRD work on the unlabeled samples showed high levels of HA formation, even across different operators owing to the reproducibility of the system. Unfortunately resolving the neutron beam data is proving difficult, and so additional techniques (FTIR and NMR) are being employed to help identify the possible borate species present (BO_2 and BO_3 being the primary species, although BO is possible). This work is currently ongoing.

The results from the initial experiments (section 4.3.2, first 7 lines of table 4.3) exploring the effect of substituting ${SO_4}^{2-}$, ${BO_3}^{3-}$, and Sr^{2+} on the crystallite yield are detailed in section 5.1.2, clearly show that the synthesis route of controlled addition without the need for pH control was successful, with all samples displaying a high quantity of HA material (82.1% - 90%), however in all but 3%B-HA (1.77 wt.% B_2O_3, 3 mol.% B) there is also significant (> 5 wt.%) amount of β-TCP present. β-TCP is a common secondary phase in HA materials due to its similar structure and composition (an ideal Ca:P for HA is 1.667, whilst for TCP it is 1.5). Seven experiments were carried out, with the first being a baseline HA sample, and the following six showing a range of substitution values as outlined in table 6.1.

The loadings of borate and sulphate in these experiments are of a similar scale to the highest levels reported in the literature (4.563 mol% for borate, and 3.125 mol% for sulphate), whilst the strontium levels are an order of magnitude lower (the max reported is 31.25 mol%, which corresponds to a 50% replacement of calcium [159]). These loadings are therefore ambitious for an initial study, and present challenges that may not be present in lower loadings – especially issues such as changing the thermal degradation temperature. The loadings used were chosen based on prior confidential work carried out at Lucideon as being both achievable, and commercially valuable.

The most likely method of TCP formation in the above experiments is during the precipitation step via the formation of monetite ($CaHPO_4$) which incorporates Ca, from either amorphous content or HA, into the structure at temperature to form TCP (both α and β potentially) - showing in figure 6.3. The formation of monetite is favoured in acidic conditions regardless of Ca:P ratio and is sparingly soluble (2.17×10^{-7} [166]) hence it is difficult to remove before firing. The two TCP phases preferentially form the β phase as it is more thermodynamically stable than the α phase <1125 °C [167]. Another potential method of formation for the TCP phase is through thermal degradation of the HA material due to it being heated too high. In experiments carried out by the author with pure HA the degradation temperature is approximately 1250 °C with different temperatures reported in the literature (1360 °C [131], and between 1200 °C and 1565 °C [168] as 2 examples) – likely due to the large effects time at temperature can have (and therefore total heat work), and the well-known inaccuracies in temperature measurements within a kiln at the temperatures in question, a problem that is usually remedied by using the same kiln for all firings, or calibration by using a Bullers ring [169]. It is also reported in the literature that sintering and degradation temperatures can be altered by substitution (a topic that will be discussed in section 6.2.4). TCP formation by thermal degradation (as illustrated in figure 6.2) is considered less likely as there is not much in the way of amorphous formation and still high levels of HA - i.e. there is still highly crystalline material and the HA level is above 30 wt.%. Typically if TCP is formed by thermal degradation then high levels of amorphous and low levels of HA will be found along with the formation of TCP, additionally these samples display almost exclusively β-TCP, whilst thermal degradation favours a mixture of α and β phases due to the fact that the temperature required for degradation of HA is above that for the conversion of β-TCP to α-TCP.

The most likely cause for the formation of TCP is the formation of monetite during the precipitation step, this would be identified by a decrease in the Ca:P ratio which would also allow the acidic condition in which the formation of monetite occurs. Figure 6.3 displays the experimental schematic that is found with monetite formation. This theory is supported by the Cation:Anion ratio being low (1.627 – 1.654) in all samples, except for 3%B-HA, leading to high levels of TCP formation. Furthermore, in the sample (3%B-HA) that has low (1.6 wt.% TCP), the Cation:Anion ratio is higher than calculated (1.687). With a ratio that is higher than 1.667, it would be expected to see the formation of CaO at low levels, which was observed for 3%B-HA, see figure 5.6. The cause of the drop/variability in Cation:Anion is likely due to poor control over the molarity of the starting reagents.

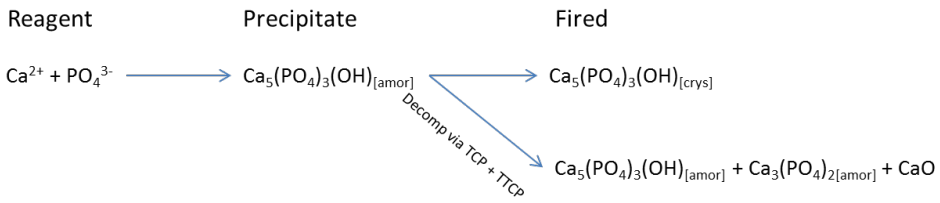


FIGURE 6.2: Schematic for the possible outcome when precipitating and firing HA material with a Ca:P of 1.667. The top line shows the ideal scenario of amorphous HA generation in the reactor, which is then calcined to produce a highly crystalline, phase pure material. The lower line shows what happens during a firing that is too hot, and leads to thermal decomposition. The HA material decomposes into TCP and TetraCalcium Phosphate (TTCP) – which is unstable above 660 °C [168]. TTCP further degrades back into HA and CaO. The entire process produces large amounts of disorder within the sample, and is hence highly amorphous when examined by XRD.

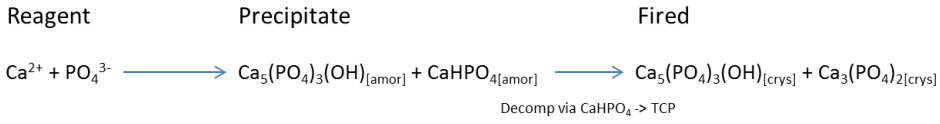


FIGURE 6.3: Schematic for the precipitation of Monetite ($CaHPO_4$) and HA alongside one another due to a pH drop during synthesis. On firing the Monetite and HA react to form TCP. As the Monetite is formed under acidic conditions at the end of the reaction, the levels are comparatively low, and as such the conversion to TCP is mediated to agree with the appropriate HA:TCP ratio for the Ca:P ratio. The major difference between this conversion to TCP and thermal degradation of HA (as demonstrated in 6.2 is the crystallinity)

As the $Ca(OH)_2$ feedstock is a dry powder and stored correctly, the most likely cause of poor control over reagent molarity is the H_3PO_4. The standard procedure for preparing the 6M feedstock is to prepare from a 85 wt.% H_3PO_4 bulk. Due to the hydrophilic nature of concentrated H_3PO_4 and general complications when handling bulk liquids it was found that the 6M H_3PO_4 solution used for the experiments for the first half of the project was only nominally 6M and in actuality demonstrated a variance of up to 3% between batches. In order to account for this discrepancy, future syntheses was carried out with H_3PO_4 that had the concentration checked by titration of 1M NaOH (Fixanal from Sigma-Aldrich).

Other possible methods for controlling the formation of monetite would be to track the addition of H_3PO_4 to pH as is done in several papers where the pH is kept high (above pH 8) – be that by halting addition to allow time for buffering, or by the addition of NH_3OH [170]. Due to the infrequent reporting of the level of crystallinity in samples, it is not clear whether the lack of monetite formation is linked to high levels of crystalline HA, or whether the TCP phase could be forced out at firing from possible seed crystals in a precipitate with a Ca:P of <1.667. It would be interesting to run a series of experiments looking at the effect of pH on various Ca:P ratios at a variety of firing temperatures to track how much influence pH control has on crystal formation over Ca:P. It is suspected that by controlling the pH to be above pH 8 - 10, HA could be produced with a lower Ca:P – although the extent of flexibility this would afford the system is unknown.

Due to the use of $Ca(OH)_2$ as the primary feedstock, there is typically 0.4 wt.% MgO present in each sample. The inclusion of Mg^{2+} into the reaction can allow for the stabilisation of β-TCP (as discussed in section 3.4.2). This stabilising effect ensures that at precipitation formation of seed crystals that can give rise to TCP is hard to avoid, and the higher temperature sintering of HA (1120 °C) is not enough to remove the β-TCP phase.

6.2.2 Effect of Ca^{2+} Source on Hydroxyapatite Formation

Various reports in the literature (as detailed in chapter 3) look at using calcium sources other than the $Ca(OH)_2$ preferred in the methods used in this thesis (for method, see section 4.3.2). Common sources include $CaCO_3$ and $Ca(NO_3)_2$ [170] as pure Ca^{2+} sources, whilst there is also literature around using different sources for their use as templating agents (e.g. Calcium Citrate) [171]. It is also known that different sources can alter the method of synthesis from a straight precipitation (as seen with $Ca(OH)_2$), to a sol-gel style reaction (typical for highly soluble Ca-salts such as $Ca(NO_3)_2$). An initial attempt at the experiments showed variations in the morphology of

particulates from the different reaction methods, a difference that could be interesting as it is known how important a role surface morphology can have on cell adhesion [20]. By investigation different Ca^{2+} sources, it is hoped that different precipitate morphologies and consequently fired morphologies can be developed. $CaCO_3$ is excluded from the study due to the well documented ease of substitution of ${CO_3}^{2-}$ into the HA lattice, either into the OH^- site, or the ${PO_4}^{3-}$ site. It is believed that this additional inclusion would add a complication to not only this set of experiments, but especially to later experiments involving substitutions.

Alongside changing the Ca^{2+} source, it is understood that the high pH of $Ca(OH)_2$ is significant in the synthesis of HA, so two runs of each material were undertaken with and without pH control to pH 9 so that the effect of pH adjustments could be investigated.

All data for this series of experiments is detailed in section 5.1.3. The data presents a surprising picture – not only is the Ca:P ratio not stable between samples, with the calcium citrate showing a significant difference (Ca:P of 1.835 vs 1.664 for the uncontrolled vs controlled runs) between runs; but also the calcium chloride samples attained high levels of crystallinity (93.7 wt.%) in spite of a low Ca:P ratio (1.627) and no pH control (both being factors that could inhibit a high percentage formation of HA). The XRD traces for these samples show that not only was a highly crystalline material formed, but that the crystal structure was changed from the typical hexagonal ($P6_3/m$) structure, to a monoclinic ($P2_1/b$) structure (see figure 6.4. The most plausible explanation for this change in unit cell is that the chloride ions are substituting into the OH^- channel. Hexagonal HA hydroxyl sites are half occupied, with spatial orientation causing the doubling of sites – effectively the OH^- can orientate with the proton either pointing north or south (see figure 6.4). This orientation is none preferential in hexagonal HA causing both sites to be occupied in a random manner. With the replacement of the OH^- with the bulkier Cl^-, and the loss of a dipole, the chloride sites gain a preferential orientation leading to the formation of the monoclinic phase. The change to monoclinic requires a higher energy of formation, and hence is rarely seen, although it is more stable and is potentially exciting for investigating the synthesis of HA crystals with ions that are either difficult to substitute and hold (for example Ag^{2+}), or for producing HA that is even less soluble – an area of particular interest in waste treatment for the mining and nuclear sectors.

The calcium citrate demonstrated sol-gel type behaviour in its formation of a clear sol on addition of acid, and producing a solid on drying – although of note the solid produced is visually marred by burnt carbon from residual

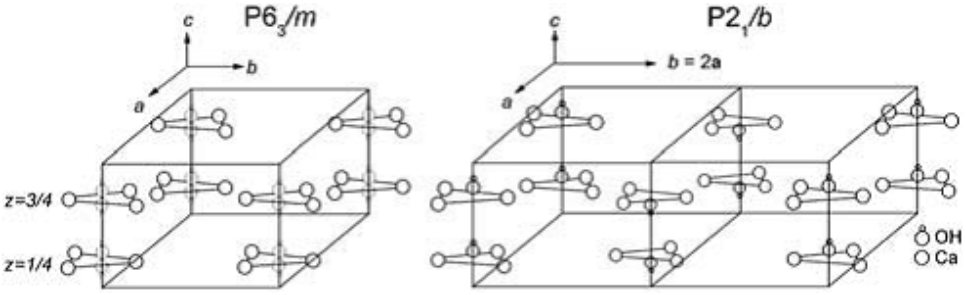


FIGURE 6.4: Graphical representation of the difference between hexagonal (left) and monoclinic (right) HA structures. In the hexagonal structure, each hydroxyl site is 50% occupied (note – there are twice as many sites – above and below each reflective plane), and the orientation can be in either direction, whilst in the monoclinic form the hydroxyl ions are fully ordered over the long-range. All additional phosphate and oxygen atoms have been left out to simplify the diagram Image taken from 'Investigation of the hydroxyapatite obtained as hydrolysis product of α-tricalcium phosphate by transmission electron microscopy' by Espanol, Montserrat, *et al.* [172].

citrate (citrate is retained due to the lack of a washing step, although as material only forms on drying, the carbon may have begun to oxidise prior to formation of the CaP crystals) which may have led to the variable Ca:P ratio and poor HA formation either by expulsion of material on firing, or by the carbon incorporating as CO_3^{2-} and thereby lowering the Cation:Anion ratio. The Calcium Citrate also showed a large change in Ca:P ratio between the two runs (the experiments being without pH control, and controlled to pH 9 with a respective change of 1.835 to 1.664), unlike the nitrate and chloride salts, which is likely due to the varying levels of hydration available to the citrate salt effecting the accuracy of calculations, as the calculations for mass to be added relies on an accurate molecular weight of the material. This is the same issue as using un-titrated H_3PO_4 and is discussed in section 3.6.1, but as an example, if the mass of calcium citrate is understated due to water adsorption by 3.25 % (i.e. 100 g of 'dry' calcium citrate is in fact 96.75 g calcium citrate and 3.25 g water) then the maximum yield would be 85 wt.% HA. A possible method for correcting this would be to dry the salt in a vacuum oven before use (oven drying is not suitable due to the thermal degradation the citrate undergoes), although this adds a time consuming and industrially expensive step – something which is the opposite of the stated aim to produce a robust, industrially relevant method.

The $Ca(NO_3)_2$ showed mostly expected data in that the pH controlled method produced purer material, with a minimal amount of TCP. The batch-to-batch Ca:P ratio was consistent (1.714 and 1.739 for samples with and without pH control respectively), and the process of synthesis a typical sol-gel

process which is comparatively simple. It was interesting to note that synthesis in the pH controlled method lead to precipitation of the material, whilst the non-pH adjusted formed a hard crystalline solid on drying. Due to the higher than calculated Ca:P ratio, the results are unexpected in that TCP has been formed, although the large amount of amorphous content (18.5 wt.%) does suggest that either a secondary phase hasn't had a suitable seed crystal – unlike CaO formation in a synthesis using $Ca(OH)_2$, or that the HA being formed is calcium-poor. Whilst the data is not ideal, the system obviously shows promise due to its wide use in the literature, however due to immediate issues surrounding scalability and development time, $Ca(OH)_2$ remains the preferred system.

6.2.3 Dual Substitution of Hydroxyapatite by a Combination of Silicate, Sulphate, Borate, and Strontium

The previous work (Various calcium sources - method in section 4.3.2, results in section 5.1.3) has shown that with the correct Ca^{2+} source, and appropriate control of H_3PO_4 addition, it is possible to produce crystalline, high purity HA material. The Ca^{2+} source was kept as $Ca(OH)_2$ as whilst $CaCl_2$ and $Ca(NO_3)_2$ showed promise there is still development work required to get them producing material of the same purity as the $Ca(OH)_2$ method previously used.

All data for this series of experiments is detailed in section 5.36 The data shows that the Ca:P ratio is mostly correct (5 of 9 experiments have a Ca:P of between 1.65 and 1.68), except for two experiments containing $SO_4{}^{2-}$ substitutions with low Ca:P ratios (Si,S-HA at 1.581, and S,B-HA at 1.570) – this was due to a similar error occurring with the $SO_4{}^{2-}$ concentration. Additionally two samples containing silicate (Sr,Si-HA rr and Si-HA) show high Ca:P ratios (1.705 and 1.797 respectively). The silicate source (TEOS) used in these experiments was not as concentrated as calculated, but as the levels of secondary phases is low (8.4% TCP in Sr,Si-HA rr, and 2.6% CaO in Si-HA which is washed out prior to cell tests) these materials are still suitable.

The most significant difference between this data and the mono-substituted experiments discussed in section 6.2.1 is the almost complete removal of TCP from the samples (excluding the low Ca:P found in the two erroneous sulphate samples, the highest level of TCP is 8.4%, with two more samples at 4.4% and 3.1%, and 4 samples with no TCP present. This is comparable to the data discussed in section 6.2.1 where all but 2 of the substitutions had TCP levels ranging from 12.7% - 17%), although there is a noticeable amount of amorphous present. This lack of TCP is indicative of the

improved control around the Ca:P ratio, and highlights the successful improvement of the method throughout the course of the project. This method development has allowed the successful substitution of 2 mol.% silicate in the presence of 2 mol.% strontium into a lattice that has survived thermal treatment at 1100 °C, whilst it is clearly reported in the literature that inclusion of $SiO_4{}^{4-}$ to a lower level (1.4 wt.%) causes the HA lattice to degrade at sintering temperatures [123].

The literature does not fully describe how to differentiate between a successful substitution, and an unsuccessful substitution. Typically researchers will look to FTIR [173] and possibly NMR [174] for evidence that the ion being substituted has an appropriate response for the expected environment, although this is usually circumstantial as it differentiates whether the X-O bond is 'capped' or not (i.e. the X-O bond is covalently bonded, or whether it is an ionic species) and therefore shows if the substitution is within an ionic lattice, or forming either a surface group or a glassy separate phase. This is useful for determining whether the HA material formed is Hydroxy- or Oxy- Apatite, as the XRD for both forms overlap due to only minor differences in d-spacings or structure factors [175] – characterised by a slight shift in the 00l peaks [176]. Within this body of work XRD has been used to determine substitution by way of discounting secondary phases, or a glassy phase. For this approach to work, it is important to correctly identify what amorphous (or indeed crystallinity) is, and how it is determined in an XRD trace.

The determination of amorphous content by comparing peak intensities and widths versus a standard material is suitable when comparing exact chemistries. In the case of substitutions, the presence of replaced ions that either change the atomic number of the atoms involved in the reflection (i.e. replacing Ca (z=20) for Sr (z=38)) will change peak intensities even in a 100% crystalline material, which corresponds to a reported amorphous content due to the method requiring equivalent chemistries. Furthermore, substitutions which effect the atomic environment around them (as all substitutions with a different element as opposed to a different isotope do) will also alter the structure factor that is applied to each reflection, and therefore its corresponding intensity. Due to these considerations and limitations of the technique, it is not possible to distinguish between amorphous content that is either a non-ordered secondary phase at the grain boundaries, a substitution that lacks long range order within the lattice, and therefore causes a peak distortion; or a substitution which changes the reflection intensity versus a pure CaP HA material. What can be drawn from the XRD data is that there is no inclusion of a secondary phase in which the substituted

material could be hidden – or there is and it can be quantified (see the inclusion of $Ca_3B_2O_7$). This is the primary benefit that XRD has over the other techniques mentioned (FTIR and NMR) as XRD can accurately distinguish between crystalline materials, whereas they cannot (although being able to distinguish between different chemical environments due to energy shifts can allow some degree of phase designation). In order to confirm that the substitutions do not exist in a separate glassy phase, a comparative experiment would have to be run to allow both techniques to be resolved and check their agreement. A good example technique for this comparison is neutron diffraction due to its sensitivity to nuclei rather than electrons. In an ideal world, a single crystal of the substituted material could be prepared and run through a single crystal X-Ray diffractometer, however this is not very feasible with the formulations in question due to the precipitate typically being in the order of nanometers.

There are alternative methods for determining the percentage crystallinity that are used in the literature. These methods all have positives and negatives, although the method reported above is still preferential as an appropriate mix of data throughput, and data accuracy. Two of the quicker methods reported involve either comparing the maximum peak intensity of the 002 reflection [110], which whilst suitable for a material with no variation in chemistry, any level of substitution can affect the intensity of the reflection, which would then give erroneous results. In the referenced paper, the author proceeded to support the data with a figure derived from NMR which did give a similar figure for 'disordered' HA (defined as HA material without OH^- groups). This value was calculated as the integrated peak area at $\sim$5 ppm shift, whilst 'ordered HA' (sample with OH^-) was calculated as the integrated peak area at $\sim$2.3 ppm. Another quick method reported is using a comparison between the maxima of the 300 reflection, and the minima between the 300 and 112 reflection. This method is heavily reliant not only on no interference to the peak intensity due to changing structure factors, but also on the assumption that all peak broadening is due to crystallite size, and not the formation of poorly ordered HA material, which would equally broaden the peak, whist still potentially being missed out from the comparison. This method is better than merely comparing a single peak due to the ability to include amorphous secondary phases. A third method reported compares the full trace of a sample versus two standards that are assumed to be 100% crystalline [177]. The standards in question are a hexagonal and a monoclinic HA sample. For the purpose (to compare the quantity and quality of a monoclinic HA) this is the best way to reasonably quantify the variation – assuming the standards are of a high quality. A useful technique used in the paper is the inclusion of a $\pm$10% marker to the crystallinity values, accepting the inherent flaws in using XRD traces

to determine crystallinity. For substitution samples, this method is clearly unfeasible as the standards are non-existent, and comparison to a standard HA is the method currently used.

One possible method to try and clarify the XRD data would be to undergo a series of firing trials to demonstrate the effects of firing temperature – or more accurately thermal work as validated by a Bullers ring – on crystallinity. This series of gradient firings and dwell times would provide a detailed data set detailing how crystalline the material can get under temperature, and allow better resolution of the crystal. The obvious trade off to this is the amount of time and resources it would require, especially for each dual substitution, and each single substitution to provide a baseline for interpretation. Some work has been done investigating the effect on thermal stability for substitutions of CO_3^{2-} (A and B type) [178], SiO_4^{4-} [123], and Sr^{2+} [179]. An excellent detailed review of thermal stability of apatites looking at fluoro-, chloro-, and substituted hydroxyl- apatites has been published and covers in detail CO_3^{2-} substitution, as well as sulphate inclusion (amongst others) [180]. Notably missing from this review is borate substitution.

It is important that the work be reproducible in order to meet the objectives originally set out (see section 2 - specifically to devise a suitable method for the consistent synthesis of novel multi-substituted hydroxyapatites). Whilst there are small variations in the Ca:P ratio (see table 5.8), it is clear that the overall reproducibility of the method is high, and work not detailed here (due to commercial sensitivity) looking at the substitution of Si, and S into the lattice and 2 mol.% each, and 4 mol.% each have shown reproducibility over several experiments (>90 wt.% HA, with no secondary phases detected). Work carried out in Lucideon has shown that inter-operator reproducibility is high so long as a stringent protocol is adhered to, with several students trained in the substitution of borate into HA generating equivalent XRD traces on samples prepared independently of one another, although under the guidance of the author. One major obstacle to showing reproducibility is the large change that a small difference can have in the material, for instance a slight change in Ca:P ratio can cause the formation of monetite, and therefore large amounts of TCP (for instance a Ca:P of 1.63 similar to that found in section 5.1.2 – sample HA2, is only 1.8% less than 1.67 as found in section 5.2.4 – sample Si,Sr-HA, but gives a difference of 17 % TCP vs 0 % TCP), whilst a change in the firing regime due to kiln variations can hugely change the crystal structure – either by overheating and degrading the structure, or by not supplying as much thermal work and leaving a less crystalline sample – a situation further exacerbated by XRD's poor sensitivity to amorphous content and therefore limited accuracy with

regard to its quantification.

6.2.4 Effect of Firing Temperature on Crystal Structure and Phase Stability

The process of consolidating the crystal structure of a ceramic material is typically referred to as either calcination, or sintering. There is a slight difference between these two processes: calcination is more general crystal consolidation and removal of volatiles, sintering is the complete densification of the structure.

The need for inorganic materials to be heat treated is well known and understood in the literature, with firing regimes typically reported in a format consisting of temperatures and dwell times. This is done for ease of understanding, with it known that once over a certain activation energy (traditionally supplied thermally, although not always as demonstrated by techniques like spark plasma sintering [181]) there is an amount of heat work required to perform consolidation of the material. Due to the engineering considerations, it is unfeasible to accurately control a kiln to the exact temperature, hence industrial tunnel kilns which are kept at temperature are usually calibrated by using a Bullers ring. This is not possible for intermittent kilns, making it important to appreciate that temperatures as reported from kilns is a 'best guess' at a figure dependent on the kiln design and thermocouple. The nuances of kiln design and control are outside of the scope of this thesis, but the basic consideration that temperatures reported in the literature are almost certainly not the same across different kilns and groups, and that the important characteristic is the heat work is above an activation point, but preferably below a degradation point.

With respect to HA materials, the common temperatures of interest are $\sim$600 °C (removal of excess water and organic), $\sim$1100 °C (towards the maximum temperature to avoid degradation), and $\sim$1300 °C (the point of thermal degradation). Typical firing schedules will focus on heating the sample sufficiently above 600 °C to encourage solid-state diffusion and crystal growth/consolidation, with higher temperatures significantly speeding up the process of densification [182]. Common temperatures seen for this are 1000 °C - 1200 °C, with dwell times varying from minutes to hours. Often researchers investigating the thermal properties of CaP materials will look at a range from <1000 °C to >1300 °C to get the full spectrum of results from poor crystal growth, to degradation of the sample.

HA degradation occurs via the schematic shown in (figure 6.2), once the activation energy is passed, the HA crystal breaks down into TCP and TTCP,

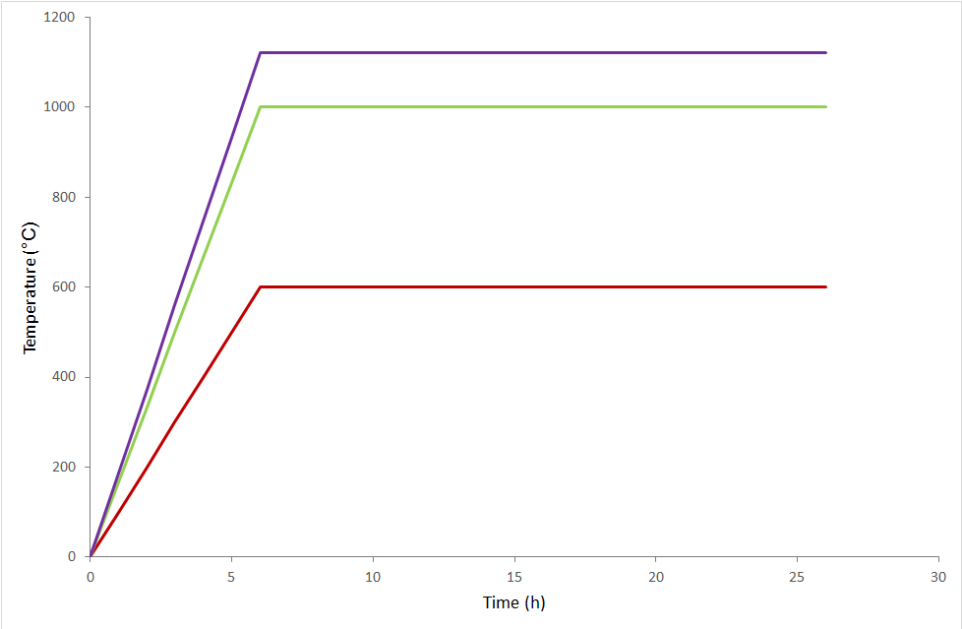


FIGURE 6.5: Firing schedules for samples to trial different dwell temperatures. Notably the ramp rates were varied to ensure temperature was reached at the same time for all samples (6 h). Dwell time was 20 h before natural cooling was allowed to occur.

which then further reacts to form additional TCP and CaO. The binding energies for the various ions within the lattice are key in controlling both the activation energy (and therefore the temperature at which diffusion and degradation occur), but also the kinetics as different ions are more or less mobile.

In a complex system such as a ceramic is it usual to rely on gathered data to design an optimal firing programme rather than building a mathematical model due to the difficulty of such an endeavour [183]. This difficulty is multiplied by the inclusion of substitutions into the calculations and therefore the best way to assess the effect of substitution on thermal properties is to perform a series of firings at different temperatures, times, and ramp rates. In reality for simplicities sake, the dwell times are often fixed, and the temperature is changed. Ramp rates may change so that the heating step takes the same time across all samples, or the experiments are carried out so that the same ramp rate is kept (i.e. 1 °C/s), and therefore the higher temperature samples spend longer getting to temperature. There is no clear benefit to one system over the other, so long as the differences are made clear and accounted for in the reporting of the data.

In the course of the experiments carried out in this work, an initial series was used to compare crystallinities at 3 different firing temperatures (600 °C, 1000 °C, and 1120 °C – see figure 6.5). The outcome of this experiment

(section 5.1.1) was to confirm that the firing schedule previously developed at Lucideon (1120 °C in 6 h, then dwell for 20 h) was appropriate and delivered low levels of amorphous content. Of particular note from these experiments is that at low temperatures the formation of TCP was not seen, yet as the crystallinity increases, TCP is clearly present in significant amounts. This difference is important as in poorly crystalline samples, many authors may report producing phase pure materials [115, 184], however either the TCP isn't highly crystalline and merely contributing to the amorphous content, it is a separate CaP form that results in TCP on firing (such as monetite), or it is hidden by the peak broadening of the dominant HA phase. In both the papers referenced for this example, the XRD traces show broad peaks for the HA (either due to amorphous content or nano-crystallites) that could easily be obscuring β-TCP peaks - especially the most intense β-TCP peaks at $\sim$31.0 and $\sim$34.4 2Θ

It is reported in the literature that the inclusion of silicate into the lattice increases the temperature required for full densification from 1000 - 1150 °C to 1200 – 1300 °C [185], additionally, and that the inclusion of higher levels of Si (> 2 wt.%), and the co-substitution of Si and Mg (>1 wt.% of each) [186] leads to destabilisation of the lattice at temperature before densification causing degradation to TCP and calcium phosphate silicates. It is important to note that the common contaminant in Calcium sources is Magnesium. This involuntary inclusion into every synthesis (typically 0.4 wt.% MgO) can play havoc with the formation of β-TCP and the firing stability of the sample. Kannan *et al.* have shown that even with a correct stoichiometry of (Ca+Mg)/P = 1.67, the inclusion of Mg leads to the formation of biphasic systems [95]. Their work considers a lowest substitution of 1.75 mol.% so there is clearly a significant gap between the loading levels they intend, and the levels seen in this work due to contamination, but the point is important to consider as Mg^{2+} inclusion does favour formation of a Ca-deficient apatite, and formation of a stabilised β-TCP phase. This demonstrates that there is a fine balance to be struck to ensure that there is a suitable level of densification without running the kiln too hot leading to degradation. This balancing act shows itself in the varying levels of amorphous content on the different substitutions and may be due to the firing not being hot enough for some samples to fully sinter.

Figures 5.2 and 5.3 show the lack of crystallographic change in samples between 1000 °C and 1120 °C, which suggests that the chemistry of samples fired at either temperature should be relatively similar, but gives no information relating to physical characteristics. When considering the physical aspect of the powders, the surface area of the trial HA foams (figure 5.21) demonstrates elegantly the change in densification of the samples

between two different firing temperatures, even though the chemical and crystallographic content of the materials have not changed. The foams produced from precipitate powder has a drop from $1.22\,\mathrm{m^2\,g^{-1}}$ ($\pm 0.02\,\mathrm{m^2\,g^{-1}}$) to $0.30\,\mathrm{m^2\,g^{-1}}$ ($\pm 0.02\,\mathrm{m^2\,g^{-1}}$) between samples fired at 1100 °C and 1200 °C. This 75% reduction in surface area is partly due to densification of the macro-scale foam structure (for example, contraction of the walls and pores) and not purely based on densification of the powder that form the grains in the structure walls with porosity (and subsequent surface area) in the sub-micron range, but it illustrates how much additional consolidation the 100 °C increase to the firing temperature causes.

6.2.5 Adaptation of the Hydroxyapatite Crystal to Accommodate Substitution

When replacing species in the HA lattice, there are two conditions to fill. Firstly there are steric considerations, and these typically lead to the lattice distorting slightly (as can be measured by XRD). The second condition to fulfill is charge balance within the lattice. HA is an ionic lattice (as opposed to a covalent lattice like a silica glass) and the replacement of an ion with a different charge requires the balancing of this new imbalance elsewhere in the lattice.

For the different substitutions looked at in this project (Sr, Si, S, and B), there are 3 possible sites for substitution (Ca-1, Ca-2, and P-1). Sr readily replaces Ca into one of the two Ca^{2+} sites within the lattice as Sr^{2+}. For this substitution to occur, there is only a steric change (Ca^{2+} - 100 pm, Sr^{2+} - 126 pm) [187] as the oxidation state is the same. There is a change in electronegativity of the ions, but that affects the properties of the material – for instance solubility – rather than changing the lattice noticeably. The remaining 3 substitutions have the potential to go into two different sites, but are far more likely to replace into just one. The two remaining sites are the ${PO_4}^{3-}$ site and the OH^- site. It is already widely reported that Si substitutes into the lattice as ${SiO_4}^{4-}$ to replace ${PO_4}^{3-}$ [188, 189], with the charge balanced by loss of a OH^-. Other mechanisms for the balance of charge have been proposed, such as balance by inclusion of ${CO_3}^{2-}$ into a neighbouring phosphate site [190], filling of a previously void Ca site (i.e. the structure is calcium deficient HA, until the inclusion of $2{SiO_4}^{3-}$ allows inclusion of the Ca^{2+} [189]), and the filling of a voided Ca^{2+} site by inclusion of 1 ${SiO_4}^{4-}$ and the conversion of $OH^- \rightarrow O^{2-}$. Gomes *et al.* published a detailed breakdown of the various charge balancing methods [191], and detailed the most influential methods of charge balancing in Si-HA to be:

$$PO_4^{3-} + OH^- \leftrightarrow SiO_4^{3-} + \square_{OH} \tag{6.1}$$

$$2PO_4^{3-} \overset{RT}{\leftrightarrow} SiO_4^{3-} + CO_3^{2-} \overset{\approx 800^\circ C,\, CO_2\uparrow}{\leftrightarrow} SiO_4^{3-} + O^{2-} \tag{6.2}$$

Evidence for the first mechanism is easily obtained by measuring physical parameters of the powders, for instance the zeta potential, and may be one of the major reasons for the improved bioactivity of Si-HA as the inclusion of SiO_4^{3-} causes the surface charge of the material to be made more negative. The additional negative charge leads to better Ca^{2+} adhesion from solution, which in turn results in better binding protein attachment [192]. The co-substitution of CO_3^{2-} is particularly of interest as CO_3^{2-} exists as a trigonal planar species, and the tetrahedral site into which it substitutes is not planar. This is important as it lends weight to the discussion of how borate is presented in B-HA.

Borate is a complex species that can take several different structures (BO_4^{5-}, BO_3^{3-}, BO_2^-) and so there is a variety of different locations that borate could possibly sit within. When replacing PO_4^{3-} both the BO_4^{5-} and BO_3^{3-} species would seem possible, BO_4^{5-} fits the steric restrictions of the site very closely, however the 2 additional free electrons causes trouble when trying to balance the charge – as seen above with silicate. BO_3^{3-} obviously leaves no charge balancing to occur, although it leaves a steric gap within the structure as it is trigonal planar (like CO_3^{2-}) and not tetrahedral like the site it is occupying. There is also scope for borate to substitute into the OH^- channel in the same way as CO_3^{2-} can do. It could either distort the channel heavily as BO_3^{3-}, or substitute as the linear BO_2^-, again leaving no charge balancing, although BO_2^- is significantly bulkier than OH^- or O^{2-}. An initial study by Ternane *et al.* in 2002 studying B-HA for potential application as a laser phosphor demonstrated both BO_3^{3-} and BO_2^- present in B-HA, with the fraction of BO_2^- decreasing as the total amount of borate inclusion is increased [109]. FTIR analysis (figure 5.17 on increasingly substituted B-HA (0, 2.5, 5, and 10 mol.% substitution) demonstrates that both BO_3 and BO_2 are present, with BO_3 being heavily preferred - as demonstrated by the lack of evidence for BO_3 at lower loadings, however quantification is not possible due to the lack of suitable standards. BO_2 is not seen until the 5 mol.% sample, and it is currently unknown where it resides within the lattice. Peak heights for the PO_4 stretches show significant reduction in line with increasing borate inclusion which suggests a replacement at the phosphate site over replacement of the hydroxyl. Equally, the hydroxyl peak ($\sim 630\,\mathrm{cm}^{-1}$) is reduced in intensity as the borate inclusion increases to 2.5 mol.%, and it is smothered by the broader PO_4 peak it sits

as a shoulder on in the 5 mol.% and 10 mol.% samples. According to Balachandera *et al.* BO_4 stretches can be seen around the 800 to 1200 cm^{-1}, unfortunately this region is already covered by the much more prevalent PO_4 stretches.

Sulphate inclusion in HA is a poorly studied field currently, and as such there are no structural studies available online at this time. The results here show that sulphate forms a ${SO_4}^{2-}$ anion, and it readily substitutes into the HA lattice via a simple precipitation method. Samples 3%S-HA and 1.5%S-HA (5 mol.% and 2.5 mol.% respectively) were synthesised resulting in highly crystalline material with high levels of HA generation (83 wt.% and 87.3 wt.% respectively). $CaSO_4$ was not seen at a 2.5 mol.% loading, but 0.6 wt.% was detected in the 5 mol.% sample. The major secondary phase was β-TCP.

Initial studies suggest that its inclusion can be used to effectively charge balance versus more negative anions (such as ${SiO_4}^{4-}$), in fact studies carried out at Lucideon by the author on client related projects have successfully produced high crystallinity (95 wt.% upwards), phase pure, di-substituted HA with 4 mol% of Si, and 4 mol% of S which demonstrated thermal stability up to 1120 °C. In this piece of work, the co-substitution of Si and S produced a poor material (52 wt.% HA and 37 wt.% β-TCP). The cause of this poor result is not immediately clear, although it is likely to be a result of a pH crash during preparation. In the absence of a more negative co-substitution (such as when including borate or strontium), how exactly does the lattice balance the charge? While HA is nominally a hydroxyl containing mineral, it is possible to dehydrate the OH^- channel to produce Oxyapatite, and in typical fired HA samples, there is a small amount of O^{2-} present. A potential mechanism for the inclusion of sulphate would be for the precipitate material to have a poorly ordered HA structure (as is typical of a precipitate), and on firing the crystal growth and sintering of the structure the hydroxide channel loses water to form O^{2-}. This process typically takes place >1100 °C, and completely occurs >1200 °C [193], but the charge balancing requirement may lower the temperature requirement. Alternatively, ${CO_3}^{2-}$could replace the OH^- in a similar style to the charge balancing seen for ${SiO_4}^{4-}$, and then either persist as a substitution or, more likely, burn out leaving O^{2-}. Both of these theories lead to the inclusion of O^{2-}, evidence of which can be checked by using FTIR. Alternatively, zeta potential may provide some insight as to the surface characteristics of the material, which could provide some credence to either theory in the same way as the reduction in negative charge in Si-HA is best explained by the formation of hydroxyl vacancies. Another technique that could be employed to check for ${CO_3}^{2-}$ incorporation is FTIR. ${CO_3}^{2-}$ is easily observed

by FTIR, with distinguishment between A and B –type substitution possible by looking at the ν_2 bands at $880\,\mathrm{cm}^{-1}$ (A-type) and $873\,\mathrm{cm}^{-1}$ (B-type). FTIR was only run at the end of the project on borate substituted samples, however no significant peaks were detected for CO_3 inclusion in either the pure HA, or the substituted materials as can be seen in figure 5.17.

Comparison of the zeta profiles for the double substituted materials offers some insight. The precipitated materials follow a standard zeta curve as expected an example is shown in figure 5.22), and across the substitutions a small range of isoelectric points are seen (ranging from 8.5 – 11.5 pH), with the exception of Sr,B-HA (figure 5.23) which shows no isoelectric point due to the zeta profile being increased by ∼20 mV. This is possibly due to three factors. Firstly, there may be some salts present in the dry powder, which on suspending in water dissolve and act as a surfactant for the particles and therefore provide a positive slip plane which is what is recorded by the zeta probe. This seems unlikely as the pH of the suspension is 7.21, and anything which is stabilising a 20 mV charge onto the powder would be affecting the pH as well. It is possible, that the inclusion of borate into the lattice has resulted in a net positive charge for the lattice, although this scenario does not fit in with the possible methods of substitution outlined in the above section. To distinguish between these different possible causes of change of surface charge additional analytical techniques could be employed, either a bulk technique such as ICP before and after a chemical wash to isolate soluble ions, or a localised technique such as Scanning Electrochemical Microscopy (SECM), combined with an EDX to measure where the positive charge is, and gain an understanding of the chemical composition of the area. These analysis techniques could also be run against the other samples which are not displaying the increase in zeta potential as a way to better understand why it is only present in one sample.

Comparison of the post-firing zeta potential is, on the other hand, is different and unexpected. All samples demonstrate an inverted trace, with the zeta potential presenting a minima at in acidic conditions, and increasing with pH (figure 5.24). This is likely caused by preferential ionic adhesion of K^+ (the base used for increasing the pH in a zeta potential titration is KOH), resulting in an increase in surface charge as KOH is added. It is likely that a similar trend would be seen if NaOH had been used for the titration, although the effect of $NH_3(OH)$ would be interesting. All samples are comparatively stable – the starting pH ranges from 7.15 – 8.12, and the magnitude of initial zeta potential values are low with all materials falling between 3.62 and 13.61 mV, except for Si,Sr-HA which has a zeta potential of -14.58 mV. These values are too low to form a stable suspension, and

would lead to rapid flocculation. At this level, the accuracy of a zeta potential measurement is nominally $\pm$4 mV, meaning the values seen are similar. Si, Sr-HA follows the same style curve; however the initial zeta potential is -14.58 mV (figure 5.25). This is still insufficient for a stable suspension, but may be indicative of the $SiO_4{}^{4-}$ causing an increase in the negative charge of the surface – as typically reported for Si-HA [99]. This decrease is not seen in any of the other silicate containing substitutions made.

The unusual form of the zeta potential vs pH profile seen in the fired materials is similar to that seen in polymeric ion exchange media [194]. This is due to the material itself having no noticeable charge, but retaining open sites for adhesion of ions. The ions then impart a surface charge to the material. This is also seen in resins that contain aminophosphate active groups to act as chelating agents [194]. Whilst this is unexpected to see as it isn't reported for HA materials, it is possible that the process of burning out the PVA binder left a residue that has coated the surface of the foams, leading to this effect. This is still hard to justify by literature as the burn out process of PVA is well characterised, with zero residue burns only needing to reach 450 °C in air [195]. Potentially the surface HA material took up a large level of $CO_3{}^{2-}$ leading to their behaviour being similar to that of an organic resin. If it is a surface coating, FTIR may not be suitable for picking up the low total level of carbon, though SEM-EDA would be a good start, possibly followed by SECM. Ultimately, the act of the HA material rapidly binding cations may be beneficial and indicative of an improved cell adhesion. The reasoning for this is that cell adhesion is mediated by attachment proteins, which are negatively charged. These proteins bind preferentially to adsorbed positive species – especially Ca^{2+} [192].

6.3 Production of Foams

In order to test the materials prepared in this project, a robust and simple method was needed for processing the primary powders – which are difficult to handle for cell work – into a more usable, and industrially relevant form. It was decided after consultation with colleagues and clients, that a foam material would offer the best compromise between device relevance, ease of production, and ease of handling.

6.3.1 Preparation and Characterisation of Foams

Six different foams were produced by varying the powder used (3 different powders) and the amount of PVA used as a foaming agent (2 wt.% loadings). The 3 powders used were all the same batch of HA, but processed at different temperatures. The raw precipitate (ppt) was used to investigate how densification and the inclusion of soluble phases may affect the final product. A calcined powder material was heated to 600 °C to a) replicate processing reported in the literature [196], and b) to investigate any differences between a foam made without low burning species that are possibly present in the ppt). The final powder for comparison is a sintered HA powder that had been pre-fired at 1120 °C. The two PVA loadings were 5 wt.% and 10 wt.%. These two loadings were chosen in an attempt to minimise the PVA content. The aim in reducing the PVA loading is to both streamline the process – PVA dissolution was by far the longest step (foaming is a 5 min process, preparation of the concentrated PVA stock for the 10% loading typically takes a full day), and to see what influence it would have on the morphology. The role of the PVA in the foam system is to provide green strength pre-firing, and to increase the viscosity of the slurry so that on agitation a foam would form.

Of all the six wet foam samples prepared, only the 5% PVA, calcined powder collapsed during drying. It is likely that the foam collapsed due to the powder being in a calcined state and lacking in green strength due to the low PVA level. This all contributed to the coalescence of the bubbles within the foam and the settling of the powder. It is unknown exactly why the calcined powder was unable to hold a foam, whilst the precipitate and fired materials were able to. The fact that the 10% PVA solution was able to maintain foam demonstrates that the issue lies in stabilisation of the foam whilst drying. A possible cause for the powder to settle may be a poor zeta potential charge leading to flocculation of the powder over time, which would then allow the larger agglomerates to settle before the foam fully dried – in accordance with Stoke's Law. It may also be possible to improve the foaming by using zeta measurements to select a better pH for foaming at, however pH controlling a 40 wt.% slurry is an awkward task and not worth investigating in the light of the 10% PVA sample working. This may either be because of the increased viscosity causing the settling of the powder to be slower, alternatively if the foam failed not because of creaming, but by coalescence then the increased PVA content and associated viscosity increase would also be significant. The final possible cause of failure is Ostwald ripening, which is unlikely in this scenario as it would be just as possible in any of the 5 other foams as the method of bubble generation (shear mixing) generates a tight size distribution of bubbles.

Once the foams were prepared, they were fired at 2 temperatures (1100 and 1200 °C) to consolidate the structure by burning out the PVA, and fusing the granules of HA together. The two different firing temperatures along with the 5 foams that survived drying provided 10 samples. These 10 samples were characterised by BET to investigate the effect that firing temperature has on surface area, as well as whether there was an increase in surface area associated with additional organic burnout of the higher PVA samples. The foams as dried were highly friable, with the high PVA samples being the least friable when handled. On firing, all samples became easily crushed, and still highly friable. The strongest foams were the lower PVA content after firing, due to the larger amount of burn out between grains ultimately reducing initial density and therefore the level of sintering and final strength. The foams produced from pre-fired HA powder also demonstrated a greater entrainment of air with the sample volume of slurry producing approximately 50% more foam by volume. This is shown in figure 5.21.

Where the precipitated and calcined samples clearly show a higher surface area at the lower firing temperature, figure 5.21. This suggests that the HA has not fully sintered therefore leaving voids and a porosity in the foam walls. At the higher firing temperature, sintering is seen, leading to a decrease in surface area. The feedstock powders which had already undergone sintering also demonstrate some additional densification, although not of the same magnitude as the samples prepared from powder feedstock that were as-precipitated, or calcined at 600 °C. It is hypothesised that this decrease in surface area from firing at 1200 °C, is due to the contraction of foam walls and sintering of grains, a process which allows any nanoporosity to coalesce and be included into larger pores that exhibit a lower surface area/volume. Upon firing to only 1100 °C the material does not finish densifying, thereby opening up a wide range of nano and meso porosities and not allowing them to finish sintering into larger pores. This is not seen in the pre-fired samples as there is not the large amount of un-sintered material to densify and therefore provide additional void generation. This could be confirmed by more detailed analysis of the foams pre- and post-firing. SEM would give clarity on the macro porosity, but the nano and meso features would be difficult to image.

As the aim of this initial foaming work was to produce a testbed for processing sample powders of the different bi substituted species so that the chemistries could be assessed for cytocompatability, as such the pore volumes and diameters were not considered critical – so long as the selected method delivered material that could be tested in vitro. When a suitable

chemistry for progression into a bone void filler is found, then this section will need to be revisited with a focus on optimising properties such as physical toughness, pore size, window size, and total porosity.

6.3.2 Multi-Substituted Hydroxyapatite Foams

The current proposed method for the formation of pores within the structure suggests that on mechanically foaming, the larger pores are formed and retained by the generation of green strength as the PVA dries. As the different powders all display different zeta values (although all positive values), it is presumed that the main driver for the macro-pore diameter is the viscosity of the PVA slurry, and the diameter is possibly controllable by varying the PVA chain length used as that will affect the contact angle that it is able to hold, along with the amount of buoyancy – and therefore air bubble volume – it can counteract. It was expected that the change in zeta value would either effect the pore sizes seen – for instance if the particles were acting as a surfactant to stabilise the air-slurry interface, then changing the particle surface charge would change the bubble volume; or that the change in zeta would change the micro porosity formed.

Zeta potential determines the level of flocculation that a system will experience, and whilst the value can be either negative or positive, it is the magnitude that is the controlling factor. Typically a value in excess of 30 mV in magnitude is required for a well dispersed mixture. Below $\sim$5 mV a slurry will rapidly coagulate and flocculate. Between these two values a rapid drop in viscosity due to particle interactions is seen. In the experiments being carried out, a difference in zeta will be found between the particles, partly due to varying pH levels from the synthesis – and therefore residual mobile alkali/acid species, and partly due to difference occupancy of ion channels in the (poorly formed) HA crystals. The ion channel in pure HA is not full, and it is known that when substituting $PO_4{}^{3-}$ for $SiO_4{}^{4-}$ the OH^- channel occupancy is lowered to maintain an overall charge balance within the crystal. It is possible that the opposite is true when replacing $PO_4{}^{3-}$ with $SO_4{}^{2-}$, however this substitution is not reported in the literature. As an additional caveat, occupancy and surface charge of substituted HA is calculated for a pure, highly crystalline material, whereas the powders used for foaming are precipitates with high (50%) levels of amorphous material. It is expected that the powders showing a higher Zeta value will consequently have larger primary pores due to the lower viscosity.

An original theory was that whilst the macro porosity was created during the mechanical process, the micro porosity was likely due to either water

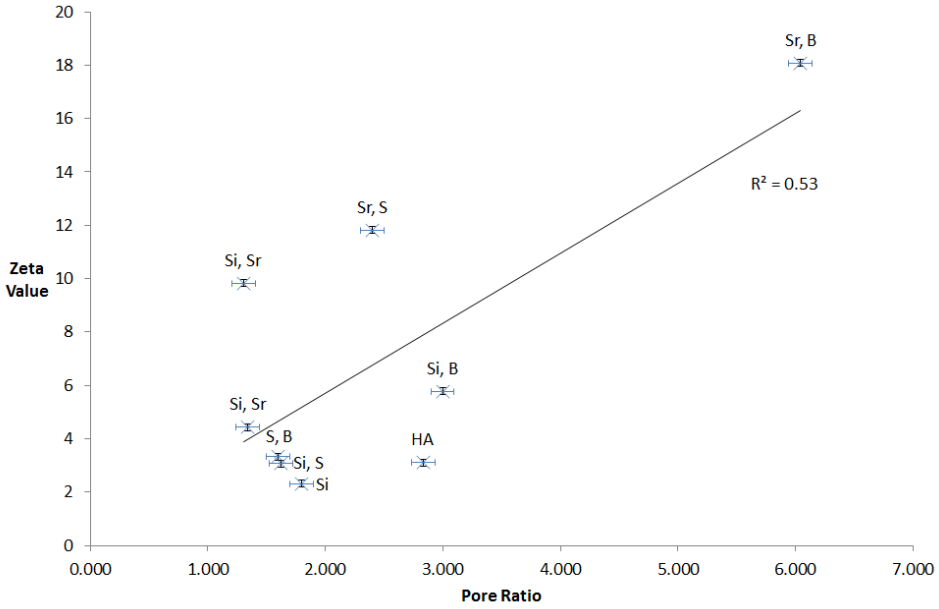


FIGURE 6.6: Zeta value Vs the Ratio of Pore Volume Greater Tan 1 µm and Smaller than 1 µm demonstrating lack of correlation between particle surface charge and pore diameter

evaporation from between ceramic particles on drying/firing, or the contraction and densification of ceramic grains on firing. If it was primarily controlled by water evaporation and therefore the opening up of pores on drying, then the Zeta charge of the particles would be an important factor in controlling the level of micro porosity – which could be represented as a change in the micro:macro intrusion volume. However, when pore ratio is plotted against Zeta, the results show very little correlation (linear line of best fit R^2 = 0.53 shown in figure 6.6)

The independence of Zeta from the foams physical properties is further highlighted by the lack of correlation between zeta and surface area. As Zeta values for the samples range from negligible (< 5 mV) through to values that are almost high enough to expect a stable suspension (18 mV, 25 mV is considered the minimum for a stable suspension), it would be expected to see some correlation between zeta and surface area. This is suspected as the higher surface area will cause a larger force to act between the particles, thereby allowing more water to be present between particulate as the foams dry. This extra water will then leave significant porosity behind, which will increase the surface area. Figure 6.8 demonstrates the lack of correlation (R^2 = 0.17) between surface area and Zeta charge.

Indeed, even the surface area and pore distribution of the samples lacks any correlation with surface area vs porosity having a R^2 value of 0.16. This is shown in figure 6.7

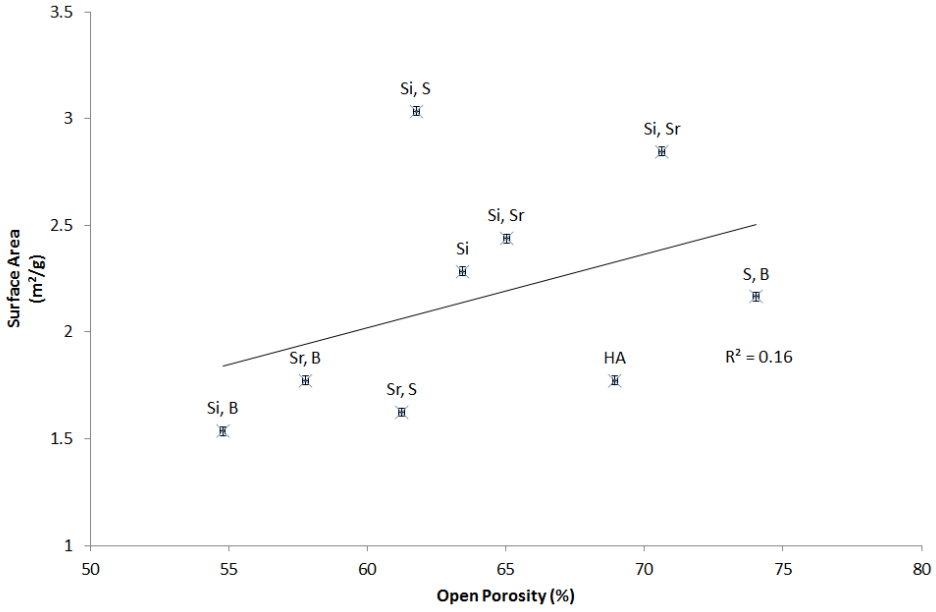


FIGURE 6.7: Surface area versus porosity graph demonstrating the lack of correlation between the volume of open space and the area of ceramic exposed. This lack of correlation shows that the surface feature is likely not tied to the volume or number of pores

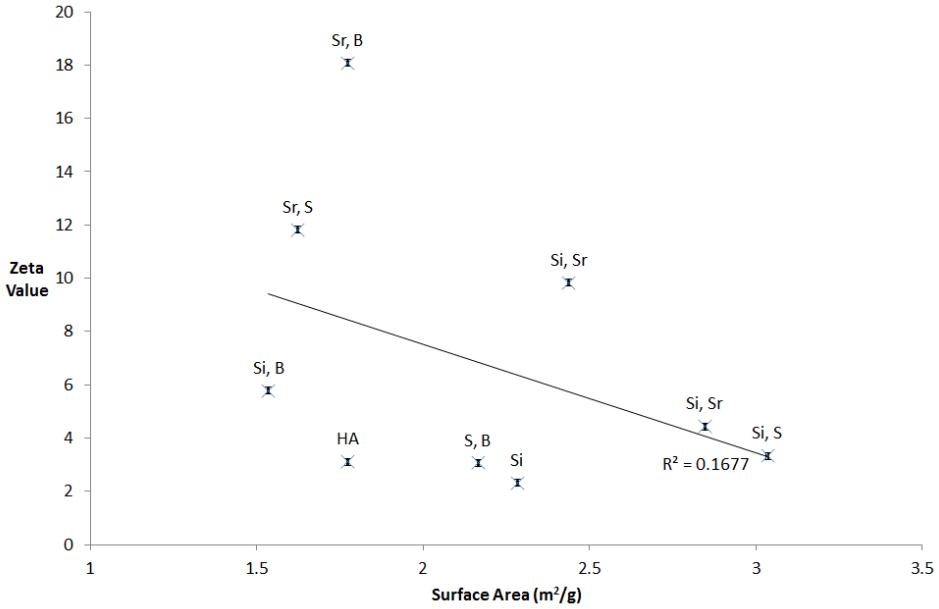


FIGURE 6.8: Graph demonstrating the lack of correlation between the surface area and zeta potential. This is an unexpected result as a lower zeta potential would cause a more flocculated system. In turn, this higher flocculation would lead to a better packed wall which, it could be assumed, would ultimately leave a lower surface area

With this complete lack of relation between such key characteristics the question is raised – what is controlling the porosity? Currently the surface area seems to have little relation to the porosity, nor does the zeta charge. It may be that the surface area is being more directly linked to nano porosity left by molecular scale channels of water evaporating – a facet that could be checked by employing BJH to measure porosity down to nm scales. Additionally, if the water channels are forming on a nano scale, then the zeta values may begin to relate to porosity at $< 0.1\,\mu\mathrm{m}$. Another possible explanation is that with zeta potential values below 30 mV, there is not a sufficient magnitude for the zeta potential to be having a significant effect, hence no noticeable difference, whereas if the same differences in zeta potential were seen, but at a range of 40 - 60 mV, then a trend may appear. It may be possible to cause such an effect with the addition of suitable surfactants.

Porosity may also be forming from grain contraction in the pore walls – whilst it is unexpected for this to produce such regular sized pores across all samples it is possible. This is further demonstrated by the SEM images, where it can be seen that in some samples (figure 6.9), high surface areas is related to a highly porous and 'noodley' pore wall, whereas other samples show what could be the formation of a liquid glassy phase that has screened the porosity, or is perhaps a final densification of the grains. The distinction between phases could be investigated by utilising TEM to investigate a specific area and look for evidence of whether the skin is amorphous or crystalline, XRD is unsuitable for this as the surface amorphous layer would be lost in bulk reflections of the underlying crystalline material and there is no way to distinguish between amorphous material, or small crystallites as a cause for peak broadening. Unfortunately, it is not always the case that the lower surface area correlates to a smoother internal wall structure, as demonstrated by Si-HA which has an equivalent surface area to Sr,B-HA, but a much more open wall structure (figure 6.10). The influence of this on the final sample characteristics could be investigated by measuring the porosity after drying, but before firing, alongside running a measurement of the level of contraction seen on firing the precipitate. It would also be interesting to link the level of contraction to the level of amorphous material present at precipitation.

Another consideration that has not been accounted for is the reliability of the foaming method – whilst the foams all display the same pore diameters (suggesting that all foams encountered a similar shear rate vs viscosity leading to bubble formation in line with Taylor's model described above), and similar total porosities, there have been no repeat foaming of the same material to check how the porosity changes from run-to-run. This batch variation may well explain the lack of correlation, as it would mean that

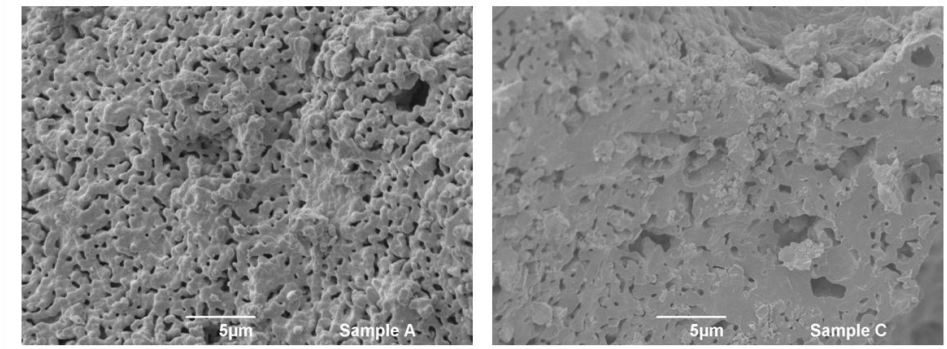


FIGURE 6.9: SEM micrograph demonstrating the difference in pore surface seen between a sample with a high surface area ($2.44\,\mathrm{m^2\,g^{-1}}$, left), and a low surface area ($1.77\,\mathrm{m^2\,g^{-1}}$, right). Sample A (left) is Sr,Si-HA and Sample C (right) is Sr,B-HA

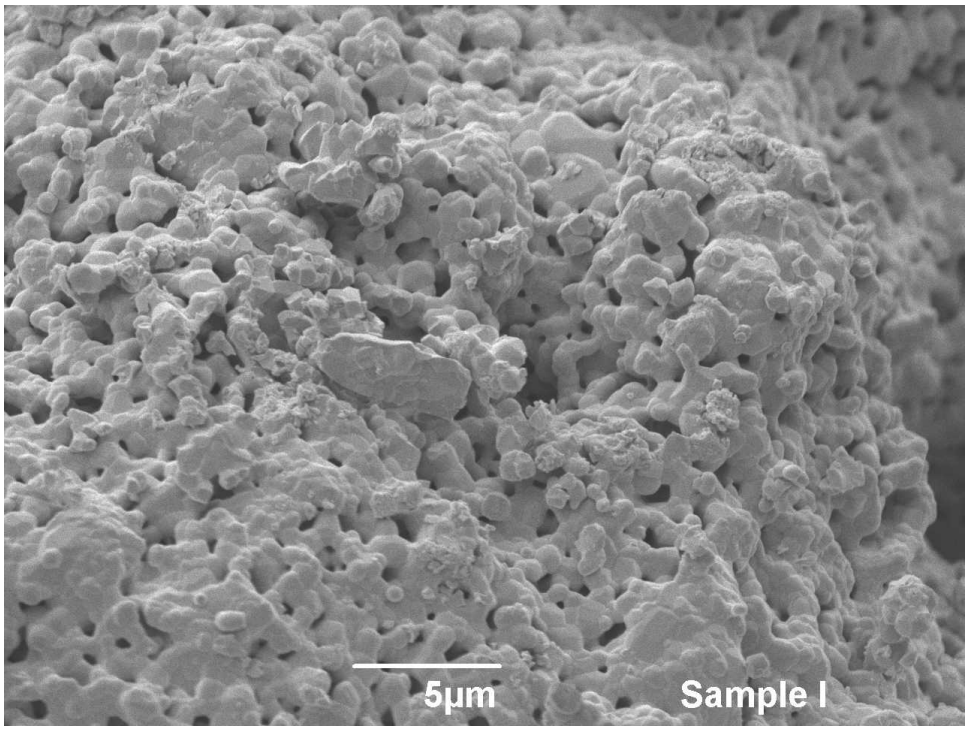


FIGURE 6.10: HA internal wall structure demonstrating an open porosity without significant densification, yet still showing a comparatively low surface area ($1.77\,\mathrm{m^2\,g^{-1}}$.)

the final physical properties of the foams are more heavily related to the mechanical processing of the slurry, rather than any slight change in surface chemistry.

A common feature seen in direct foams, as described in section 3.5.3, is the formation of interconnecting, or 'strut', pores. These typically form as windows between two main pores, and will be around an order of magnitude smaller than the main pores. They are often easily identifiable by both mercury intrusion, and SEM. In the samples presented here, some degree of strut porosity is seen on mercury intrusion, however it is either a hump on the side of the main pore peak, or a small component sat separately (As shown in an example trace in figure 5.26), suggesting that the strut pores are of a similar size to the main pores. This could be due to the drying process being too fast, therefore causing swelling of the pores or a pressure increase from water evaporation. Potentially this increase in pressure would cause the bubbles to pop, rather than open slowly hence causing the features seen. Equally, the strut porosity is not clearly seen by SEM (figure 6.11), as commonly it would be expected that one can see pores in the struts opening up into additional cells within the body of the material. Similar surface structure is seen in figure 6.13 where a paper presented by Munar *et al.* shows the surface to be formed by the fusing of individual particles leaving a submicron porosity between particles. This is not in complete disagreement with the literature, as A. Studart *et al.* report in their review of ceramic processing, they show two different SEM images of direct foamed materials, one unknown and the other alumina that show both the porosity typically expected (clean, circular pores and strut pores well defined), and similar to the porosity seen in these samples (less-regularly shaped pores, pore strut porosity). These two SEMs are reproduced below (figure 6.12) and it can be seen even by observation that the alumina sample (on the right) shows similarities to the SEMs reported here.

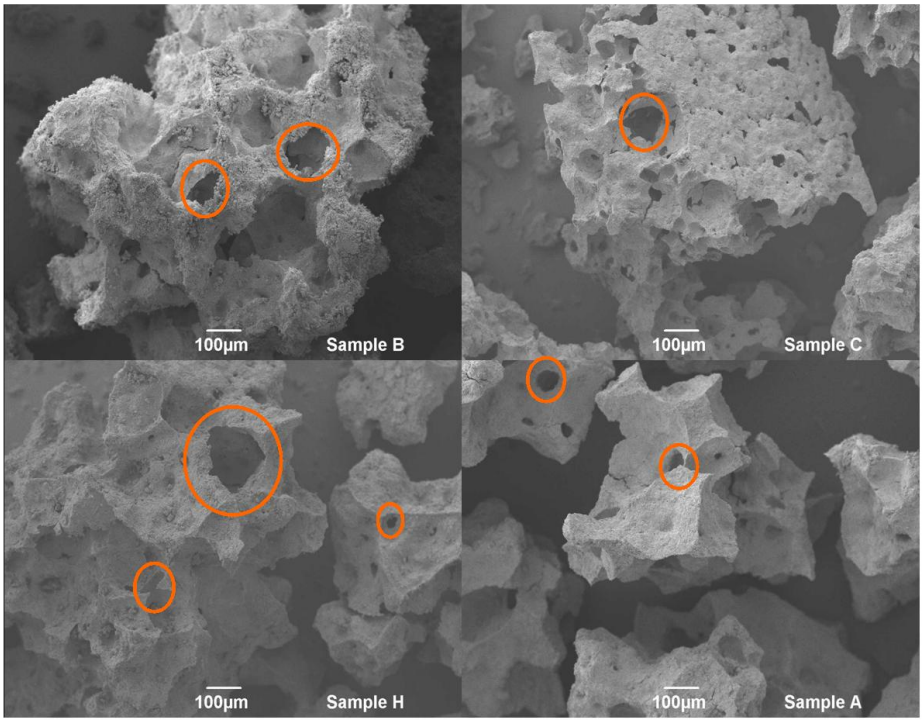


FIGURE 6.11: Comparison of various foams highlighting visible strut pores. As can be seen the different samples display varying levels of visible strut porosity, however in all cases it is much lower than expected, and does not seem to follow a regular shape – leading to questions about their mode of formation

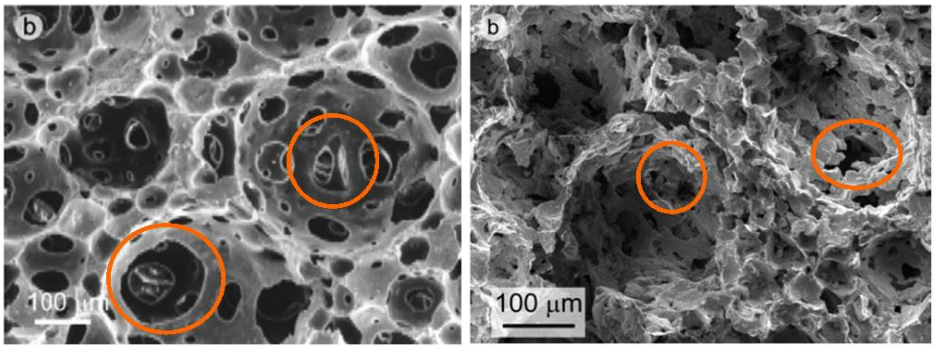


FIGURE 6.12: Comparison of two SEMs from A. Studart *et al.* Both foams were produced by direct foaming, however one was produced using monomer polymerisation to lock the structure (left), and the other was an alumina sample foamed in alginate (right). The difference in pore structure is highly evident, with the sample on the right more closely resembling the materials presented here.

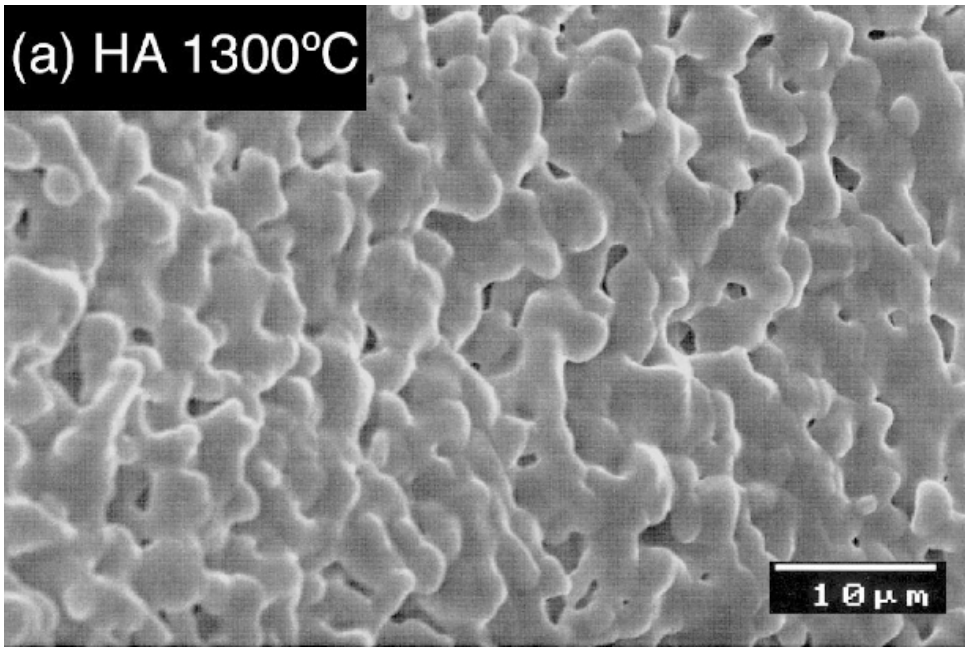


FIGURE 6.13: Example of the surface of a HA foam after firing at 1300 °C. Image taken from a paper by Munar *et al.* [197]. The structure was derived by casting a HA slurry onto a polyurethane foam and burning out the foam, in comparison to the method used in this thesis. The structure displays the same form of individual particles fused together presenting a surface with significant sub-micron porosity.

6.4 Biological Assessment of Materials

As an initial screen for biological efficacy preliminary studies of material using MG63 cells to assess cytotoxicity and bioactivity were carried out.

6.4.1 Cell Viability on Various HA Foams

By varying the firing regime that the feedstock HA powder was exposed to (i.e. either using the precipitate as-is, calcining at 600 °C, or sintering at 1100 °C) it was possible to produce a range of different foamed materials. Changing the weight percentage of PVA was showed to be relatively insignificant in comparison to the pre-treatment of the powder, except for foam stability an issue only for the calcined powders. The physical characterisation of the foams is discussed further in section 4.3.4.

Once the foams had been produced, a short cell assay was run to determine if there was an optimum processing method for producing a suitable 3D structure to at as a test platform for measuring *in vitro* responses to substituted HA. A key requirement was that the structure not display any cytotoxic responses (as detected by poor cell adhesion and spreading). Samples were run in triplicate, and compared to a positive control of Tissue Culture Plastic. Measurements were taken at both day 3 and day 6 to check initial cell health at a time point when confluence would have recently been achieved, and a later time point to show continued cell health. As an initial screen only cell activity was measured via Alamar Blue®, and not normalised versus a DNA assay due to the interest being the foam as a test platform, meaning that a suitably high response is required to show up variations due to chemical alteration of the ceramic.

The day 3 data (figure 5.41) shows the most heavily fired samples (pre-fired HA powder, re-fired as a foam at 1200 °C) as being significantly ($p < 0.05$) to the control. All other samples are equivalent, within the group of foams, and compared to the culture plastic. Of the 8 foams that are equivalent, the foam made from precipitated powder and 5 wt.% PVA are by far the simplest to reproduce. Day 6 data (5.41) shows the foams all being significantly different to the controls, with the exception of foam produced from pre-fired material, and subsequently burnt out at 1200 °C. Even with a reduced total cell activity level, there appears to be very little justification for the additional steps required to make the better performing foams, when the simplest production route offers a structure that is equivalent in all but 3 cases (2 foams worse performing at 3 days, 1 better performing at 6 days). The lower cell activity compared to the positive control (bare tissue culture plastic) is reported in the literature [198], and is likely due to a lower total

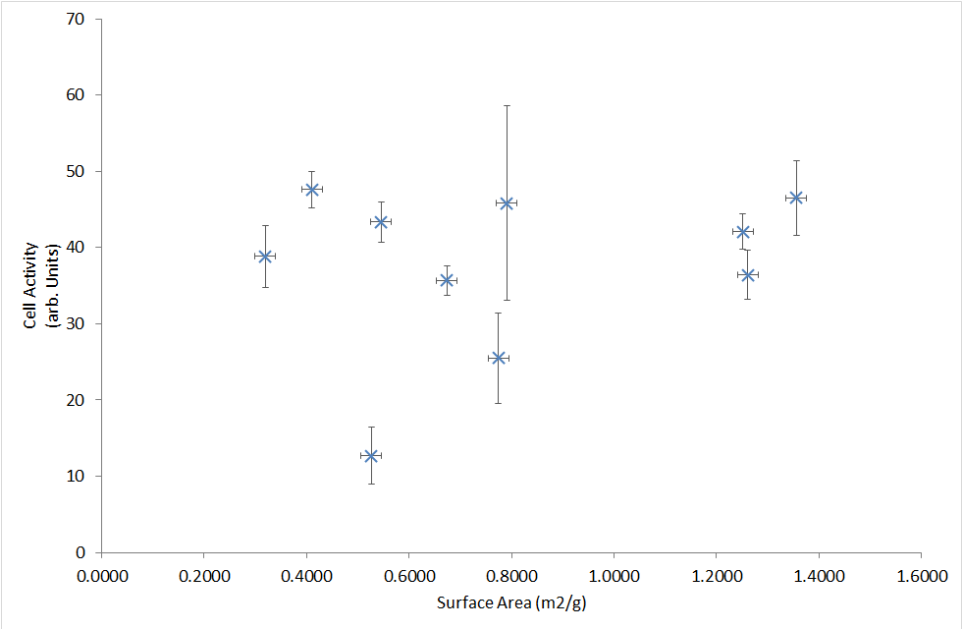


FIGURE 6.14: Comparison graph of cell activity (y-axis, arbritary units) versus surface area (x-axis, m^2/g). Sample labels have been left off in order to maintain legibility. The Graph demonstrates the lack of correlation between surface area and cell viability. Error bars are $\pm 0.02\,m\,g^{-2}$ for the x-axis, and the standard error for the y-axis.

cell count as the 3D structure is non-optimal for larger cell numbers than a flat surface.

As the different processing parameters for forming the foams gives rise to variations in surface area (as discussed in sections 6.3.1 and 6.3.2) the cell response was plotted against surface area for day 3 (figure 6.14). The lack of correlation between these two parameters further strengthens the decision to use the simplest production method as even large changes in surface area (within the relatively small ranges investigated here) are not correlated to cell activity.

6.4.2 Mx-HA Foam Cell Analysis

This section discusses the preliminary cell data generated on Mx-HA foams. The samples were initially run by the author, with the trends confirmed in subsequent experiments by MPhil candidates under the supervision of Dr. Colin Scotchford. As the data is preliminary it is important to note that all results and trends discussed here are merely indicative and require further work.

All samples were shown to be non-cytotoxic with Alamar Blue confirming cells were actively metabolising, and DNA staining showing that samples had reached confluence within 7 days. By normalising the metabolic data to DNA concentration (figure 5.44), There is only one significant difference within the 7 day data set (Si,S-HA vs baseline HA), though at 21 days several pairs demonstrate significant reductions as compared to the Tissue Culture Plastic control, but not versus the baseline HA composition, or the Actifuse analogue. This data suggests that none of the substitutions are negatively affecting the ability of the material to act as a general cell scaffold. There does appear to be a downward trend in the data that may justify more rigorous testing to prove out.

In order to assess cell activity specifically relating to bone turnover an Osteocalcin assay was performed, to check for signs of cell maturation as a marker of advanced cell processes.

MG63 demonstrates both mature and immature osteoblastic features [199], and as such Osteocalcin production doesn't tend to occur until later into the culture period when the cells have matured. This can be expedited by activating the cells with β-glycerophosphate and ascorbic acid. In these trials there was no activation procedure followed so that it could be investigated if the biomaterial had an effect on the differentiation of the cells. Osteocalcin's specific mode of activity isn't well understood, but it is known that it is excreted solely by osteoblasts and plays a function in bone mineralization. It is widely used as a biomarker on the effectiveness of a material on bone formation, both *in vitro* and *in vivo* [200]. As figure 6.15 demonstrates, one sample (Sr,S-HA) showed a marked increase over the tissue culture plastic (control), baseline HA, and the Actifuse analogue (Si-HA). This increase in Osteocalcin is indicative of the material providing an early trigger for MG63 cells to mature and start being more specific in their metabolic activities. The significance of this improvement over the positive control, baseline hydroxyapatite, and the Actifuse analogue is important – it shows a specific improvement in the secretion of a marker that is solely produced by active osteoblasts, and as such demonstrates that this sample has an improved bioresponse. It appears that the other samples have negligible levels of Osteocalcin, which could either be attributed to slow maturation of the MG63 cells (a process that can typically take 21-28 days [158]) or to a retardation of the maturation process. In order to differentiate between these two options, a longer time period is required (in excess of 28 days). Additionally, Alkaline Phosphatase data will show if the cells are engaged in osteo-activity, or just general proliferation and cell activity for earlier time points. This marked improvement is a significant development and shows that one of the compositions produced has the potential to answer

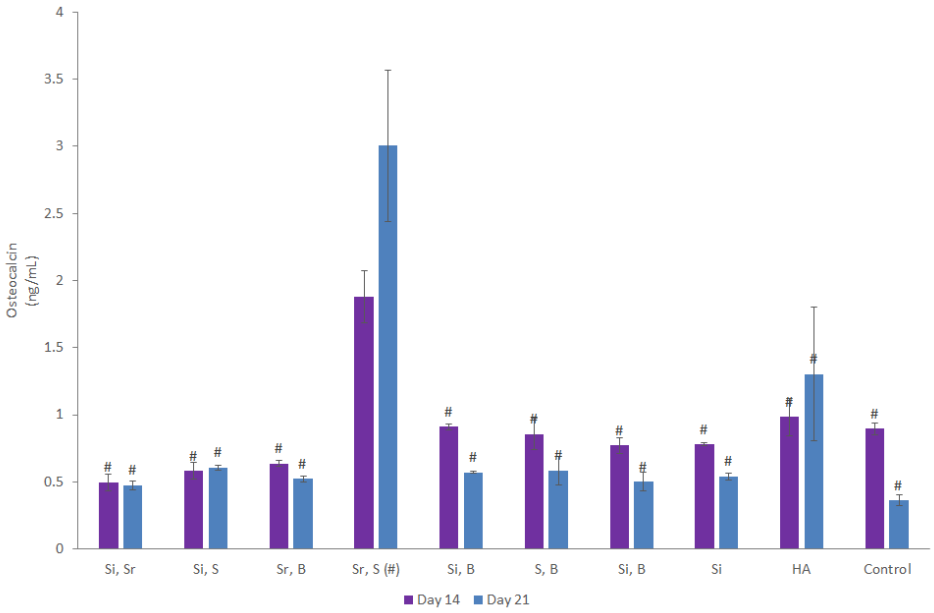


FIGURE 6.15: Osteo-activity measurement of samples by tracking osteocalcin content at day 14 and day 21. All samples are shown to be equivalent, except for Sr,S-HA which has a significant increase in the levels of osteocalcin produced. Error bars are the standard error of the data (n=3, control n=3). The control was tissue culture plastic. Foaming method is detailed in section 4.3.4, and sample composition is detailed in section 5.2.4, the y-axis units are $\mathrm{ng\,ml^{-1}}$. Significance of $p < 0.05$ is denoted by a mark above the data correlating with the appropriate sample marked on the axis (i.e. an ♯ on the data shows a significant difference versus Sr,S-HA)

the aim of the project - namely to provide an effective alternative to autologous bone.

The cause for this improvement in osteo-activity is not currently understood, as the increase is not seen in other combinations with either Sr or S. It is possible that the inclusion of sulphate increases the rate of release of Sr^{2+} which is shown to have a noticeable effect on osteo-activity [82], however data by Aina *et al.* did not show an increase in cell activity on dosing with $SrCl_2$ to mimic pure Sr^{2+} dissolution [76]. It is worth noting that Aina only measured general cell activity, and not a specific osteo-activity marker, such as osteocalcin or alkaline phosphatase.

The *in vitro* aspect of the work demonstrates that the co-substitution of Sr and S into HA provides a significant benefit to osteoactivity, however the mechanism for it is not clearly understood. In context of the project objectives this preliminary cell data has shown that a material with superior bioactivity has been synthesised and processed into an appropriate form.

A suitable continuation of the work would be to repeat the synthesis of this composition, repeat the initial assays along with more sophisticated *in vitro* techniques (such as gene expression and use of primary lines), and then explore the mechanism of action.

7 Conclusion

This thesis has been set out to address three objectives, as repeated below:

1. Devise a suitable method for the consistent synthesis of novel multi-substituted hydroxyapatites
2. Develop a suitable method for forming a 3D structure with the novel ceramic
3. Characterise the material chemically, physically, and biologically *in vitro*

In order to succeed in these objectives, work was carried out to iterate and improve on an existing wet chemistry precipitation method for the production of calcium phosphate materials. Through modification of raw material selection, addition parameters, and post-processing temperatures it was possible to arrive at a synthesis route that allows for easy scale up and consistently yields high purity material. By following the procedures outlined in section 4.3.2 kilo scale batches of novel, multi-substituted hydroxyapatites were produced for analysis.

Having developed a suitable synthesis method, a simple foaming technique using PVA as a foaming agent, and physical agitation to introduce air bubbles was trialled. The method was chosen to be simple, quick, and low cost - again to lend itself to large scale production in future. A series of samples all using the same base material were conducted to investigate any effects that post processing of the precipitate had, and what amount of PVA was required for a stable foam. By testing the foams *in vitro* it was also possible to investigate the effect that small changes in surface area had on cell response in order to better select a final processing route. The foaming experiments indicated that so long as a stable foam was generated, there was no important differences to be found in cell response and as such the simplest and quickest foaming method could be used.

Finally preliminary *in vitro* analysis of the multi-substituted hydroxyapatite foams was performed, demonstrating that there is no significant loss in general cell activity, and no instance of cytotoxicity, with the inclusion of substitutions discussed in this project. The *in vitro* work also highlighted one substitution (Sr,S-HA) that showed a significant increase in the production of

osteocalcin, an important marker or cell differentiation and osteo-activity. This result is exceptionally promising and suggests that the novel substitution presented here may offer enhanced activity *in vivo*. The obvious next steps for this work would be to confirm the increased osteo-activity with a wider range of *in vitro* trials in order to better understand the mechanism causing the increased activity.

The project set out to provide a foamed, novel substituted-hydroxyapatite. In this it was successful with a host of novel substitutions carried out and characterised. Novelty is found both in the levels achieved, as well as the combinations described. With these novel materials a simple series of *in vitro* tests have highlighted a potential material for further development, as well as confirming no ill affects from the other inclusions.

Possible further work based on this thesis can be split into 3 key areas:

1. Further analysis of Sr,S-HA to understand mechanism of action, and demonstrate improved performance *in vivo*
2. Push the capability of the precipitation method to produce samples with increasingly high levels of substitution for applications both within and without the biomaterials field
3. Assess the substitutions for use in superior processing routes. The current PVA foaming method is suitable for a non-load bearing application, but advances in 3D printing and composite production (for instance) open up possible applications where increased bioactivity is required for the lower surface areas at point of anchor for the medical device (i.e. knuckle, ankle, and knee replacements)

Bibliography

[1] ASD Report. Orthopedic Devices Market to Grow at a CAGR of 7.6% from 2010-2017;. Available from: https://www.asdreports.com/news-295/orthopedic-devices-market-grow-at-cagr-76-20102017.

[2] BA LC. Orthopaedics and industry;.

[3] Markets and markets. Orthopedic Devices Market (Forecast to 2016);. Available from: http://www.marketsandmarkets.com/Market-Reports/orthopedic-device-280.html.

[4] Gomez PF, Morcuende JA. Early attempts at hip arthroplasty-1700s to 1950s. Iowa Orthopaedic Journal. 2005;25:25.

[5] Kurtz SM, Lau E, Ong K, Zhao K, Kelly M, Bozic KJ. Future young patient demand for primary and revision joint replacement: national projections from 2010 to 2030. Clinical Orthopaedics and Related Research. 2009;467(10):2606–2612.

[6] Sen M, Miclau T. Autologous iliac crest bone graft: should it still be the gold standard for treating nonunions? Injury. 2007;38(1):S75–S80.

[7] Ng VY. Risk of disease transmission with bone allograft. Orthopedics. 2012;35(8):679–681.

[8] McKay WF, Peckham SM, Badura JM. A comprehensive clinical review of recombinant human bone morphogenetic protein-2 (INFUSE® Bone Graft). International orthopaedics. 2007;31(6):729–734.

[9] Ramani P, Babhulkar S, Pawar S, Cahyadi A, Singh A, Faris M. New surgical technique to degenerative lumbar canal stenosis in the elderly without instability: Senior author's design;.

[10] Witte F, Kaese V, Haferkamp H, Switzer E, Meyer-Lindenberg A, Wirth C, et al. In vivo corrosion of four magnesium alloys and the associated bone response. Biomaterials. 2005;26(17):3557–3563.

[11] Van der Stok J, Van Lieshout EM, El-Massoudi Y, Van Kralingen GH, Patka P. Bone substitutes in the Netherlands–a systematic literature review. Acta biomaterialia. 2011;7(2):739–750.

[12] Weiner S, Wagner HD. The material bone: structure-mechanical function relations. Annual Review of Materials Science. 1998;28(1):271–298.

[13] Lowenstam HA, Weiner S. On biomineralization. Oxford University Press on Demand; 1989.

[14] Currey JD. Role of collagen and other organics in the mechanical properties of bone. Osteoporosis International. 2003;14:S29–S36.

[15] Hassenkam T, Fantner GE, Cutroni JA, Weaver JC, Morse DE, Hansma PK. High-resolution AFM imaging of intact and fractured trabecular bone. Bone. 2004;35(1):4–10.

[16] Jackson S, Cartwright A, Lewis D. The morphology of bone mineral crystals. Calcified Tissue Research. 1978;25(1):217–222.

[17] Guagliardi A, Giannini C, Cedola A, Mastrogiacomo M, Ladisa M, Cancedda R. Toward the x-ray microdiffraction imaging of bone and tissue-engineered bone. Tissue Engineering Part B: Reviews. 2009;15(4):423–442.

[18] Fantner GE, Rabinovych O, Schitter G, Thurner P, Kindt JH, Finch MM, et al. Hierarchical interconnections in the nano-composite material bone: Fibrillar cross-links resist fracture on several length scales. Composites Science and Technology. 2006;66(9):1205–1211.

[19] Rey C, Combes C, Drouet C, Glimcher MJ. Bone mineral: update on chemical composition and structure. Osteoporosis International. 2009;20(6):1013–1021.

[20] Deligianni DD, Katsala ND, Koutsoukos PG, Missirlis YF. Effect of surface roughness of hydroxyapatite on human bone marrow cell adhesion, proliferation, differentiation and detachment strength. Biomaterials. 2000;22(1):87–96.

[21] Martin J, Schwartz Z, Hummert T, Schraub D, Simpson J, Lankford J, et al. Effect of titanium surface roughness on proliferation, differentiation, and protein synthesis of human osteoblast-like cells (MG63). Journal of biomedical materials research. 1995;29(3):389–401.

[22] Lohmann C, Sagun R, Sylvia V, Cochran D, Dean D, Boyan B, et al. Surface roughness modulates the response of MG63 osteoblast-like cells to 1, 25-(OH) 2D3 through regulation of phospholipase A2 activity and activation of protein kinase A. Journal of biomedical materials research. 1999;47(2):139–151.

[23] Alberts B, Johnson A, Lewis J, Raff M, Roberts K, Walter P. Molecular biology of the cell. new york: Garland science; 2002. Classic textbook now in its 5th Edition. 2010;.

[24] Jahangir A, Nunley R, Mehta S, Sharan A. Bone-graft substitutes in orthopaedic surgery. AAOS Now. 2008;2(1):35–37.

[25] Baer W, Schaller P, Carl H. Spongy hydroxyapatite in hand surgery–a five year follow-up. Journal of Hand Surgery (British and European Volume). 2002;27(1):101–103.

[26] Ooms E, Wolke J, Van Der Waerden J, Jansen J. Trabecular bone response to injectable calcium phosphate (Ca-P) cement. Journal of biomedical materials research. 2002;61(1):9–18.

[27] Erbe E, Clineff T, Lavagnino M, Dejardin L, Arnoczky S. Comparison of Vitoss (tm) and ProOsteon 500R in a critical-sized defect at 1 year. In: Annual Meeting of the Orthopaedic Research Society; 2001. p. 25–28.

[28] Shors E. Bone graft substitutes: clinical studies using coralline hydroxyapatite. Biomaterials in surgery Stuttgart: Thieme. 1998;1998:83–9.

[29] Bodde EW, Wolke JG, Kowalski RS, Jansen JA. Bone regeneration of porous β-tricalcium phosphate (Conduit^{TM} TCP) and of biphasic calcium phosphate ceramic (Biosel®) in trabecular defects in sheep. Journal of Biomedical Materials Research Part A. 2007;82(3):711–722.

[30] Ploumis A, Albert TJ, Brown Z, Mehbod AA, Transfeldt EE. Healos graft carrier with bone marrow aspirate instead of allograft as adjunct to local autograft for posterolateral fusion in degenerative lumbar scoliosis: a minimum 2-year follow-up study: Clinical article. Journal of Neurosurgery: Spine. 2010;13(2):211–215.

[31] Kunakornsawat S, Kirinpanu A, Piyaskulkaew C, Sathira-Angkura V. A comparative study of radiographic results using HEALOS collagen-hydroxyapatite sponge with bone marrow aspiration versus local bone graft in the same patients undergoing posterolateral lumbar fusion. Journal of the Medical Association of Thailand= Chotmaihet thangphaet. 2013;96(8):929–935.

[32] Daculsi G, Laboux O, Malard O, Weiss P. Current state of the art of biphasic calcium phosphate bioceramics. Journal of Materials Science: Materials in Medicine. 2003;14(3):195–200.

[33] Simmonds MC, Brown JV, Heirs MK, Higgins JP, Mannion RJ, Rodgers MA, et al. Safety and effectiveness of recombinant human bone morphogenetic protein-2 for spinal fusion: a meta-analysis of individual-participant data. Annals of internal medicine. 2013;158(12):877–889.

[34] Fu R, Selph S, McDonagh M, Peterson K, Tiwari A, Chou R, et al. Effectiveness and harms of recombinant human bone morphogenetic protein-2 in spine fusion: a systematic review and meta-analysis. Annals of internal medicine. 2013;158(12):890–902.

[35] Smucker JD, Petersen EB, Fredericks DC. Assessment of MASTERGRAFT PUTTY as a graft extender in a rabbit posterolateral fusion model. Spine. 2012;37(12):1017–1021.

[36] Zamet J, Darbar U, Griffiths G, Bulman J, Brägger U, Bürgin W, et al. Particulate bioglass® as a grafting material in the treatment of periodontal intrabony defects. Journal of clinical periodontology. 1997;24(6):410–418.

[37] Vrouwenvelder W, Groot C, De Groot K. Histological and biochemical evaluation of osteoblasts cultured on bioactive glass, hydroxylapatite, titanium alloy, and stainless steel. Journal of biomedical materials research. 1993;27(4):465–475.

[38] Epstein NE. An analysis of noninstrumented posterolateral lumbar fusions performed in predominantly geriatric patients using lamina autograft and beta tricalcium phosphate. The Spine Journal. 2008;8(6):882–887.

[39] Stryker. Vitoss Bone Graft Substitute;. Available from: `http://www.stryker.com/en-us/products/Orthobiologicals/BoneRepair/Vitoss/index.htm`.

[40] Theiss F, Apelt D, Brand B, Kutter A, Zlinszky K, Bohner M, et al. Biocompatibility and resorption of a brushite calcium phosphate cement. Biomaterials. 2005;26(21):4383–4394.

[41] O'Connell J, Wen H, Adams A, Thorne K, Akella R, Garrett R. CopiOs® Sponge Bone Void Filler: Engineering a Microenvironment Conducive for Bone Growth;.

[42] Bajada S, Harrison P, Ashton B, Cassar-Pullicino V, Ashammakhi N, Richardson J. Successful treatment of refractory tibial nonunion using calcium sulphate and bone marrow stromal cell implantation. Bone & Joint Journal. 2007;89(10):1382–1386.

[43] Hopgood P, Kumar R, Wood P. Ankle arthrodesis for failed total ankle replacement. Bone & Joint Journal. 2006;88(8):1032–1038.

[44] Wheeler DL, Jenis LG, Kovach ME, Marini J, Turner AS. Efficacy of silicated calcium phosphate graft in posterolateral lumbar fusion in sheep. The Spine Journal. 2007;7(3):308–317.

[45] Hing KA, Wilson LF, Buckland T. Comparative performance of three ceramic bone graft substitutes. The Spine Journal. 2007;7(4):475–490.

[46] Hing KA, Revell PA, Smith N, Buckland T. Effect of silicon level on rate, quality and progression of bone healing within silicate-substituted porous hydroxyapatite scaffolds. Biomaterials. 2006;27(29):5014–5026.

[47] Downing M, Johansson U, Carlsson L, Walliker J, Spraggs P, Dodson H, et al. A bone-anchored percutaneous connector system for neural prosthetic applications. Ear, nose, & throat journal. 1997;76(5):328–332.

[48] Schott. Transponder Glass;. Available from: `http://www.schott.com/epackaging/english/glass/transponder.html`.

[49] BonAlive Putty Product Brief;. Available from: `http://www.bonalive.com/media/uploads/documents/bonalive-putty_product-brief_trauma_spine.pdf`.

[50] BioSphere Properties;. Available from: `http://www.synergybiomedical.com/bioactive-glass-properties.html`.

[51] Zhao JH, Tsai CH, Chang YC. Management of radicular cysts using platelet-rich fibrin and bioactive glass: a report of two cases. Journal of the Formosan Medical Association. 2014;113(7):470–476.

[52] Kokubo T, Takadama H. How useful is SBF in predicting in vivo bone bioactivity? Biomaterials. 2006;27(15):2907–2915.

[53] Bohner M, Lemaitre J. Can bioactivity be tested in vitro with SBF solution? Biomaterials. 2009;30(12):2175–2179.

[54] Rohanová D, Boccaccini AR, Yunos DM, Horkavcová D, Březovská I, Helebrant A. TRIS buffer in simulated body fluid distorts the assessment of glass–ceramic scaffold bioactivity. Acta biomaterialia. 2011;7(6):2623–2630.

[55] Rohanová D, Boccaccini AR, Horkavcová D, Bozděchová P, Bezdička P, Častorálová M. Is non-buffered DMEM solution a suitable medium

for in vitro bioactivity tests? Journal of Materials Chemistry B. 2014;2(31):5068–5076.

[56] Pan H, Zhao X, Darvell BW, Lu WW. Apatite-formation ability–predictor of "bioactivity"? Acta biomaterialia. 2010;6(11):4181–4188.

[57] Maçon AL, Kim TB, Valliant EM, Goetschius K, Brow RK, Day DE, et al. A unified in vitro evaluation for apatite-forming ability of bioactive glasses and their variants. Journal of Materials Science: Materials in Medicine. 2015;26(2):1–10.

[58] Houmard M, Fu Q, Genet M, Saiz E, Tomsia AP. On the structural, mechanical, and biodegradation properties of HA/β-TCP robocast scaffolds. Journal of Biomedical Materials Research Part B: Applied Biomaterials. 2013;101(7):1233–1242.

[59] Wu C, Fan W, Zhou Y, Luo Y, Gelinsky M, Chang J, et al. 3D-printing of highly uniform CaSiO 3 ceramic scaffolds: preparation, characterization and in vivo osteogenesis. Journal of Materials Chemistry. 2012;22(24):12288–12295.

[60] Padmanabhan SK, Carrozzo M, Gervaso F, Scalera F, Sannino A, Licciulli A. Mechanical performance and in vitro studies of hydroxyapatite/wollastonite scaffold for bone tissue engineering. In: Key Engineering Materials. vol. 493. Trans Tech Publ; 2012. p. 855–860.

[61] Roohani-Esfahani S, Lu Z, Li J, Ellis-Behnke R, Kaplan D, Zreiqat H. Effect of self-assembled nanofibrous silk/polycaprolactone layer on the osteoconductivity and mechanical properties of biphasic calcium phosphate scaffolds. Acta biomaterialia. 2012;8(1):302–312.

[62] Liu FH, Shen YK, Lee JL. Selective laser sintering of a hydroxyapatite-silica scaffold on cultured MG63 osteoblasts in vitro. International Journal of Precision Engineering and Manufacturing. 2012;13(3):439–444.

[63] Li H, Yang L, Dong X, Gu Y, Lv G, Yan Y. Composite scaffolds of nano calcium deficient hydroxyapatite/multi-(amino acid) copolymer for bone tissue regeneration. Journal of Materials Science: Materials in Medicine. 2014;25(5):1257–1265.

[64] Alfotawi R, Naudi K, Dalby MJ, Tanner KE, McMahon JD, Ayoub A. Assessment of cellular viability on calcium sulphate/hydroxyapatite injectable scaffolds. Journal of tissue engineering. 2013;4:2041731413509645.

[65] Rajzer I, Menaszek E, Kwiatkowski R, Chrzanowski W. Bioactive nanocomposite PLDL/nano-hydroxyapatite electrospun membranes

for bone tissue engineering. Journal of Materials Science: Materials in Medicine. 2014;25(5):1239–1247.

[66] Rampersad SN. Multiple applications of Alamar Blue as an indicator of metabolic function and cellular health in cell viability bioassays. Sensors. 2012;12(9):12347–12360.

[67] Al-Nasiry S, Geusens N, Hanssens M, Luyten C, Pijnenborg R. The use of Alamar Blue assay for quantitative analysis of viability, migration and invasion of choriocarcinoma cells. Human reproduction. 2007;22(5):1304–1309.

[68] Freshney RI. Culture of animal cells, a manual of basic technique. John Wiley and Sons, inc;.

[69] Lowry OH, Rosebrough NJ, Farr AL, Randall RJ, et al. Protein measurement with the Folin phenol reagent. J biol Chem. 1951;193(1):265–275.

[70] Smith P, Krohn RI, Hermanson G, Mallia A, Gartner F, Provenzano M, et al. Measurement of protein using bicinchoninic acid. Analytical biochemistry. 1985;150(1):76–85.

[71] Hartree EF. Determination of protein: a modification of the Lowry method that gives a linear photometric response. Analytical biochemistry. 1972;48(2):422–427.

[72] Lee NK, Sowa H, Hinoi E, Ferron M, Ahn JD, Confavreux C, et al. Endocrine regulation of energy metabolism by the skeleton. Cell. 2007;130(3):456–469.

[73] Lee AJ, Hodges S, Eastell R, et al. Measurement of osteocalcin. Annals of clinical biochemistry. 2000;37(4):432–446.

[74] Reginster JY, Badurski J, Bellamy N, Bensen W, Chapurlat R, Chevalier X, et al. Efficacy and safety of strontium ranelate in the treatment of knee osteoarthritis: results of a double-blind, randomised placebo-controlled trial. Annals of the rheumatic diseases. 2012;p. annrheumdis–2012.

[75] Hesaraki S, Alizadeh M, Nazarian H, Sharifi D. Physico-chemical and in vitro biological evaluation of strontium/calcium silicophosphate glass. Journal of Materials Science: Materials in Medicine. 2010;21(2):695–705.

[76] Aina V, Bergandi L, Lusvardi G, Malavasi G, Imrie FE, Gibson IR, et al. Sr-containing hydroxyapatite: morphologies of HA crystals and

bioactivity on osteoblast cells. Materials Science and Engineering: C. 2013;33(3):1132–1142.

[77] Li Z, Lam W, Yang C, Xu B, Ni G, Abbah S, et al. Chemical composition, crystal size and lattice structural changes after incorporation of strontium into biomimetic apatite. Biomaterials. 2007;28(7):1452–1460.

[78] Hoppe A, Güldal NS, Boccaccini AR. A review of the biological response to ionic dissolution products from bioactive glasses and glass-ceramics. Biomaterials. 2011;32(11):2757–2774.

[79] Mohammadi MS, Ahmed I, Muja N, Almeida S, Rudd C, Bureau M, et al. Effect of Si and Fe doping on calcium phosphate glass fibre reinforced polycaprolactone bone analogous composites. Acta biomaterialia. 2012;8(4):1616–1626.

[80] Tampieri A, D'Alessandro T, Sandri M, Sprio S, Landi E, Bertinetti L, et al. Intrinsic magnetism and hyperthermia in bioactive Fe-doped hydroxyapatite. Acta biomaterialia. 2012;8(2):843–851.

[81] Fuleihan GEH. Strontium Ranelate-A Novel Therapy for Osteoporosis or a Permutation of the Same? New England Journal of Medicine. 2004;350(5):504–506.

[82] Meunier PJ, Roux C, Seeman E, Ortolani S, Badurski JE, Spector TD, et al. The effects of strontium ranelate on the risk of vertebral fracture in women with postmenopausal osteoporosis. New England Journal of Medicine. 2004;350(5):459–468.

[83] Oudadesse H, Dietrich E, Bui XV, Le Gal Y, Pellen P, Cathelineau G. Enhancement of cells proliferation and control of bioactivity of strontium doped glass. Applied Surface Science. 2011;257(20):8587–8593.

[84] O'donnell M, Hill R. Influence of strontium and the importance of glass chemistry and structure when designing bioactive glasses for bone regeneration. Acta Biomaterialia. 2010;6(7):2382–2385.

[85] Marie P, Ammann P, Boivin G, Rey C. Mechanisms of action and therapeutic potential of strontium in bone. Calcified tissue international. 2001;69(3):121–129.

[86] Zhang W, Shen Y, Pan H, Lin K, Liu X, Darvell BW, et al. Effects of strontium in modified biomaterials. Acta Biomaterialia. 2011;7(2):800–808.

[87] Capuccini C, Torricelli P, Sima F, Boanini E, Ristoscu C, Bracci B, et al. Strontium-substituted hydroxyapatite coatings synthesized by

pulsed-laser deposition: in vitro osteoblast and osteoclast response. Acta Biomaterialia. 2008;4(6):1885–1893.

[88] Saidak Z, Marie PJ. Strontium signaling: molecular mechanisms and therapeutic implications in osteoporosis. Pharmacology & therapeutics. 2012;136(2):216–226.

[89] Aina V, Lusvardi G, Annaz B, Gibson IR, Imrie FE, Malavasi G, et al. Magnesium-and strontium-co-substituted hydroxyapatite: the effects of doped-ions on the structure and chemico-physical properties. Journal of Materials Science: Materials in Medicine. 2012;23(12):2867–2879.

[90] Zreiqat H, Howlett C, Zannettino A, Evans P, Schulze-Tanzil G, Knabe C, et al. Mechanisms of magnesium-stimulated adhesion of osteoblastic cells to commonly used orthopaedic implants. Journal of biomedical materials research. 2002;62(2):175–184.

[91] Yamasaki Y, Yoshida Y, Okazaki M, Shimazu A, Uchida T, Kubo T, et al. Synthesis of functionally graded MgCO3 apatite accelerating osteoblast adhesion. Journal of biomedical materials research. 2002;62(1):99–105.

[92] Bodhak S, Kikuchi M, Oyane A, Sogo Y, Tsurushima H, Ito A. Influence of Ca2+ and Mg2+ Supplementation on In Vitro Biological Properties of Hydroxyapatite/Collagen Nanocomposite Membrane. In: Key Engineering Materials. vol. 493. Trans Tech Publ; 2012. p. 126–131.

[93] Campbell AA, LoRe M, Nancollas GH. The influence of carbonate and magnesium ions on the growth of hydroxyapatite, carbonated apatite and human powdered enamel. Colloids and surfaces. 1991;54:25–31.

[94] Cao X, Harris W. Carbonate and magnesium interactive effect on calcium phosphate precipitation. Environmental science & technology. 2007;42(2):436–442.

[95] Kannan S, Lemos I, Rocha J, Ferreira J. Synthesis and characterization of magnesium substituted biphasic mixtures of controlled hydroxyapatite/β-tricalcium phosphate ratios. Journal of Solid State Chemistry. 2005;178(10):3190–3196.

[96] Carlisle EM. Silicon: a requirement in bone formation independent of vitamin D1. Calcified tissue international. 1981;33(1):27–34.

[97] Reffitt D, Ogston N, Jugdaohsingh R, Cheung H, Evans BAJ, Thompson R, et al. Orthosilicic acid stimulates collagen type 1 synthesis

and osteoblastic differentiation in human osteoblast-like cells in vitro. Bone. 2003;32(2):127–135.

[98] Bohner M. Silicon-substituted calcium phosphates–a critical view. Biomaterials. 2009;30(32):6403–6406.

[99] Botelho C, Lopes M, Gibson I, Best S, Santos J. Structural analysis of Si-substituted hydroxyapatite: zeta potential and X-ray photoelectron spectroscopy. Journal of Materials Science: Materials in Medicine. 2002;13(12):1123–1127.

[100] Wu C, Chang J. A review of bioactive silicate ceramics. Biomedical materials. 2013;8(3):032001.

[101] Naghii M, Samman S. The role of boron in nutrition and metabolism. Progress in food & nutrition science. 1992;17(4):331–349.

[102] Nielsen FH, Hunt CD, Mullen LM, Hunt JR. Effect of dietary boron on mineral, estrogen, and testosterone metabolism in postmenopausal women. The FASEB journal. 1987;1(5):394–397.

[103] King N, Odom TW, Sampson HW, Yersin AG. The effect ofin ovo boron supplementation on bone mineralization of the vitamin D-deficient chicken embryo. Biological trace element research. 1991;31(3):223–233.

[104] Palacios C. The role of nutrients in bone health, from A to Z. Critical reviews in food science and nutrition. 2006;46(8):621–628.

[105] Wu C, Miron R, Sculean A, Kaskel S, Doert T, Schulze R, et al. Proliferation, differentiation and gene expression of osteoblasts in boron-containing associated with dexamethasone deliver from mesoporous bioactive glass scaffolds. Biomaterials. 2011;32(29):7068–7078.

[106] Brown RF, Rahaman MN, Dwilewicz AB, Huang W, Day DE, Li Y, et al. Effect of borate glass composition on its conversion to hydroxyapatite and on the proliferation of MC3T3-E1 cells. Journal of Biomedical Materials Research Part A. 2009;88(2):392–400.

[107] Hakki SS, Bozkurt BS, Hakki EE. Boron regulates mineralized tissue-associated proteins in osteoblasts (MC3T3-E1). Journal of Trace Elements in Medicine and Biology. 2010;24(4):243–250.

[108] Gorustovich AA, López JMP, Guglielmotti MB, Cabrini RL. Biological performance of boron-modified bioactive glass particles implanted in rat tibia bone marrow. Biomedical Materials. 2006;1(3):100.

[109] Ternane R, Cohen-Adad MT, Panczer G, Goutaudier C, Kbir-Ariguib N, Trabelsi-Ayedi M, et al. Introduction of boron in hydroxyapatite:

synthesis and structural characterization. Journal of alloys and compounds. 2002;333(1):62–71.

[110] Barheine S, Hayakawa S, Jäger C, Shirosaki Y, Osaka A. Effect of Disordered Structure of Boron-Containing Calcium Phosphates on their In Vitro Biodegradability. Journal of the American Ceramic Society. 2011;94(8):2656–2662.

[111] Yiannopoulos Y, Chryssikos GD, Kamitsos E. Structure and properties of alkaline earth borate glasses. Physics and chemistry of glasses. 2001;42(3):164–172.

[112] Kamitsos E, Patsis A, Karakassides M, Chryssikos GD. Infrared reflectance spectra of lithium borate glasses. Journal of Non-Crystalline Solids. 1990;126(1-2):52–67.

[113] Alderman NE. Sterile plaster of paris as an implant in the infrabony environment: a preliminary study. Journal of periodontology. 1969;40(1):11–13.

[114] Palmieri A, Pezzetti F, Brunelli G, Scapoli L, Muzio LL, Scarano A, et al. Calcium sulfate acts on the miRNA of MG63E osteoblast-like cells. Journal of Biomedical Materials Research Part B: Applied Biomaterials. 2008;84(2):369–374.

[115] Alshemary AZ, Goh YF, Akram M, Razali IR, Kadir MRA, Hussain R. Microwave assisted synthesis of nano sized sulphate doped hydroxyapatite. Materials Research Bulletin. 2013;48(6):2106–2110.

[116] Ahmad S, Latif MA, Taib H, Ismail AF. Short review: Ceramic foam fabrication techniques for wastewater treatment application. In: Advanced Materials Research. vol. 795. Trans Tech Publ; 2013. p. 5–8.

[117] Deville S. Freeze-casting of porous ceramics: a review of current achievements and issues. Advanced Engineering Materials. 2008;10(3):155–169.

[118] Studart AR, Gonzenbach UT, Tervoort E, Gauckler LJ. Processing routes to macroporous ceramics: a review. Journal of the American Ceramic Society. 2006;89(6):1771–1789.

[119] De Gennes PG, Brochard-Wyart F, Quéré D. Capillarity and wetting phenomena: drops, bubbles, pearls, waves. Springer Science & Business Media; 2013.

[120] Stafford RE, Fanni T, Dennis EA. Interfacial properties and critical micelle concentration of lysophospholipids. Biochemistry. 1989;28(12):5113–5120.

[121] Kunjappu JT. Ink chemistry;. Available from: `https://www.chemistryworld.com/news/ink-chemistry/1013163.article`.

[122] Hunter TN, Pugh RJ, Franks GV, Jameson GJ. The role of particles in stabilising foams and emulsions. Advances in Colloid and Interface Science. 2008;137(2):57–81.

[123] Bianco A, Cacciotti I, Lombardi M, Montanaro L. Si-substituted hydroxyapatite nanopowders: synthesis, thermal stability and sinterability. Materials Research Bulletin. 2009;44(2):345–354.

[124] Whyte J, Hadden D, Gibson IR, Skakle J. Synthesis and stability of potassium/carbonate co-substituted hydroxyapatites. In: Key Engineering Materials. vol. 361. Trans Tech Publ; 2008. p. 207–210.

[125] Stephen J, Pace C, Skakle J, Gibson IR. Comparison of Carbonate Hydroxyapatite with and without Sodium Co-substitution. In: Key Engineering Materials. vol. 330. Trans Tech Publ; 2007. p. 19–22.

[126] Gibson IR, Bonfield W. Novel synthesis and characterization of an AB-type carbonate-substituted hydroxyapatite. Journal of biomedical materials research. 2002;59(4):697–708.

[127] Gibson IR, Skakle JM, Hadden DJ, Buckland T. Biomedical materials. Google Patents; 2014. US Patent 8,758,500.

[128] Tadic D, Epple M. A thorough physicochemical characterisation of 14 calcium phosphate-based bone substitution materials in comparison to natural bone. Biomaterials. 2004;25(6):987–994.

[129] Filippov YY, Klimashina E, Ankudinov A, Putlayev V. Carbonate substituted hydroxyapatite (CHA) powder consolidated at 450 °C. In: Journal of Physics: Conference Series. vol. 291. IOP Publishing; 2011. p. 012036.

[130] Paul Barnes MV Simon Jacques. Sources of Peak Broadening;. Available from: `http://pd.chem.ucl.ac.uk/pdnn/peaks/broad.htm`.

[131] Liao CJ, Lin FH, Chen KS, Sun JS. Thermal decomposition and reconstitution of hydroxyapatite in air atmosphere. Biomaterials. 1999;20(19):1807–1813.

[132] Levitt SR, Crayton PH, Monroe EA, Condrate RA. Forming method for apatite prostheses. Journal of biomedical materials research. 1969;3(4):683–684.

[133] Ferraz M, Monteiro F, Manuel C. Hydroxyapatite nanoparticles: a review of preparation methodologies. Journal of Applied Biomaterials and Biomechanics. 2004;2(2):74–80.

[134] Cunniffe GM, O'Brien FJ, Partap S, Levingstone TJ, Stanton KT, Dickson GR. The synthesis and characterization of nanophase hydroxyapatite using a novel dispersant-aided precipitation method. Journal of Biomedical Materials Research Part A. 2010;95(4):1142–1149.

[135] Wang P, Li C, Gong H, Jiang X, Wang H, Li K. Effects of synthesis conditions on the morphology of hydroxyapatite nanoparticles produced by wet chemical process. Powder Technology. 2010;203(2):315–321.

[136] Bouyer E, Gitzhofer F, Boulos M. Morphological study of hydroxyapatite nanocrystal suspension. Journal of Materials Science: Materials in Medicine. 2000;11(8):523–531.

[137] Kothapalli C, Wei M, Vasiliev A, Shaw M. Influence of temperature and concentration on the sintering behavior and mechanical properties of hydroxyapatite. Acta Materialia. 2004;52(19):5655–5663.

[138] Niu JL. Hydrothermal synthesis of nano-crystalline hydroxyapatite. In: Key Engineering Materials. vol. 330. Trans Tech Publ; 2007. p. 247–250.

[139] Zhang Z, Brown S, Goodall JB, Weng X, Thompson K, Gong K, et al. Direct continuous hydrothermal synthesis of high surface area nanosized titania. Journal of Alloys and Compounds. 2009;476(1):451–456.

[140] Yoshimura M, Byrappa K. Hydrothermal processing of materials: past, present and future. Journal of Materials Science. 2008;43(7):2085–2103.

[141] Pramanik S, Agarwal AK, Rai K. Development of high strength hydroxyapatite for hard tissue replacement. Trends in Biomaterials and Artificial Organs. 2005;19(1):46–51.

[142] Ho WF, Hsu HC, Hsu SK, Hung CW, Wu SC. Calcium phosphate bioceramics synthesized from eggshell powders through a solid state reaction. Ceramics international. 2013;39(6):6467–6473.

[143] Tas AC. Combustion synthesis of calcium phosphate bioceramic powders. Journal of the European ceramic society. 2000;20(14):2389–2394.

[144] Sasikumar S, Vijayaraghavan R. Synthesis and characterization of bioceramic calcium phosphates by rapid combustion synthesis. Journal of Materials Science & Technology. 2010;26(12):1114–1118.

[145] Stark WJ, Pratsinis SE, Maciejewski M, Loher SF, Baiker A. Flame synthesis of metal salt nanoparticles, in particular calcium and phosphate comprising nanoparticles. Google Patents; 2011. US Patent 7,879,303.

[146] Manafi S, Yazdani B, Rahimiopour M, Sadrnezhaad S, Amin M, Razavi M. Synthesis of nano-hydroxyapatite under a sonochemical/hydrothermal condition. Biomedical Materials. 2008;3(2):025002.

[147] Guo X, Xiao P. Effects of solvents on properties of nanocrystalline hydroxyapatite produced from hydrothermal process. Journal of the European Ceramic Society. 2006;26(15):3383–3391.

[148] Wang YJ, Lai C, Wei K, Chen X, Ding Y, Wang ZL. Investigations on the formation mechanism of hydroxyapatite synthesized by the solvothermal method. Nanotechnology. 2006;17(17):4405.

[149] Zhang S, Lai C, Wei K, Wang Y. Kinetic studies on the synthesis of hydroxyapatite nanowires by solvothermal methods. Australian journal of chemistry. 2007;60(2):99–104.

[150] Ma MG, Zhu JF. Solvothermal synthesis and characterization of hierarchically nanostructured hydroxyapatite hollow spheres. European Journal of Inorganic Chemistry. 2009;2009(36):5522–5526.

[151] Yang C, Yang P, Wang W, Wang J, Zhang M, Lin J. Solvothermal synthesis and characterization of Ln (Eu 3+, Tb 3+) doped hydroxyapatite. Journal of colloid and interface science. 2008;328(1):203–210.

[152] Pramanik S, Agarwal AK, Rai K, Garg A. Development of high strength hydroxyapatite by solid-state-sintering process. Ceramics International. 2007;33(3):419–426.

[153] Rao RR, Kannan T. Synthesis and sintering of hydroxyapatite–zirconia composites. Materials Science and Engineering: C. 2002;20(1):187–193.

[154] Madsen IC, Scarlett NV, Cranswick LM, Lwin T. Outcomes of the International Union of Crystallography Commission on powder diffraction round robin on quantitative phase analysis: samples 1a to 1h. Journal of Applied Crystallography. 2001;34(4):409–426.

[155] Guinier A. Théorie et technique de la radiocristallographie: par A. Guinier,.. Dunod; 1956.

[156] Quantitative Phase Analysis (QPA);. Available from: `https://www.nist.gov/sites/default/files/documents/mml/6-1_NScarlett_APD_IV.pdf`.

[157] Bortolotti M, Lutterotti L, Lonardelli I. ReX: a computer program for structural analysis using powder diffraction data. Journal of applied crystallography. 2009;42(3):538–539.

[158] Scotchford C. Personal Communique;.

[159] Šupová M. Substituted hydroxyapatites for biomedical applications: a review. Ceramics International. 2015;41(8):9203–9231.

[160] Gibson I, Best S, Bonfield W. Chemical characterization of silicon-substituted hydroxyapatite. Journal of biomedical materials research. 1999;44(4):422–428.

[161] Duncan J, MacDonald JF, Hanna JV, Shirosaki Y, Hayakawa S, Osaka A, et al. The role of the chemical composition of monetite on the synthesis and properties of α-tricalcium phosphate. Materials Science and Engineering: C. 2014;34:123–129.

[162] Dorozhkin SV. Amorphous calcium (ortho) phosphates. Acta Biomaterialia. 2010;6(12):4457–4475.

[163] Destainville A, Champion E, Bernache-Assollant D, Laborde E. Synthesis, characterization and thermal behavior of apatitic tricalcium phosphate. Materials Chemistry and Physics. 2003;80(1):269–277.

[164] Itatani K, Tsuchiya K, Sakka Y, Davies IJ, Koda S. Fabrication of Highly-Densified Hydroxyapatite Ceramic with Boron Oxide Addition and Its Superplastic Deformation. In: IOP Conference Series: Materials Science and Engineering. vol. 18. IOP Publishing; 2011. p. 022020.

[165] Ciftci E, Köse S, Korkusuz P, Timuçin M, Korkusuz F. Boron Containing Nano Hydroxyapatites (Bn-HAp) Stimulate Mesenchymal Stem Cell Adhesion, Proliferation and Differentiation. Key Engineering Materials. 2014;631.

[166] Moreno EC, Gregory TM, Brown WE. Solubility of CaHP04· 2H20 a, nd Formation of Ion Pairs in the System Ca (OH) 2-H3 P04-H20 at 37.5 C;.

[167] Carrodeguas RG, De Aza S. α-Tricalcium phosphate: synthesis, properties and biomedical applications. Acta biomaterialia. 2011;7(10):3536–3546.

[168] Moseke C, Gbureck U. Tetracalcium phosphate: Synthesis, properties and biomedical applications. Acta Biomaterialia. 2010;6(10):3815–3823.

[169] Mantec. Bullers Pyrometric Rings;. Available from: `http://www.mantectechnicalceramics.com/sites/default/files/bullers_rings_brochure.pdf`.

[170] Ebrahimpour A, Johnsson M, Richardson CF, Nancollas GH. The characterization of hydroxyapatite preparations. Journal of colloid and interface science. 1993;159(1):158–163.

[171] Martins MA, Santos C, Almeida MM, Costa MEV. Hydroxyapatite micro-and nanoparticles: nucleation and growth mechanisms in the presence of citrate species. Journal of colloid and interface science. 2008;318(2):210–216.

[172] Espanol M, Portillo J, Manero JM, Ginebra MP. Investigation of the hydroxyapatite obtained as hydrolysis product of α-tricalcium phosphate by transmission electron microscopy. CrystEngComm. 2010;12(10):3318–3326.

[173] Rehman I, Bonfield W. Characterization of hydroxyapatite and carbonated apatite by photo acoustic FTIR spectroscopy. Journal of Materials Science: Materials in Medicine. 1997;8(1):1–4.

[174] Panda R, Hsieh M, Chung R, Chin T. FTIR, XRD, SEM and solid state NMR investigations of carbonate-containing hydroxyapatite nanoparticles synthesized by hydroxide-gel technique. Journal of Physics and Chemistry of Solids. 2003;64(2):193–199.

[175] Heimann RB, Lehmann HD. Bioceramic Coatings for Medical Implants: Trends and Techniques. John Wiley & Sons; 2015.

[176] Gross K, Berndt C, Stephens P, Dinnebier R. Oxyapatite in hydroxyapatite coatings. Journal of materials science. 1998;33(15):3985–3991.

[177] Morgan H, Wilson R, Elliott J, Dowker S, Anderson P. Preparation and characterisation of monoclinic hydroxyapatite and its precipitated carbonate apatite intermediate. Biomaterials. 2000;21(6):617–627.

[178] Barralet J, Knowles J, Best S, Bonfield W. Thermal decomposition of synthesised carbonate hydroxyapatite. Journal of Materials Science: Materials in Medicine. 2002;13(6):529–533.

[179] Dagang G, Kewei X, Yong H. Thermal Stability of Stoichiometric Strontium-Incorporated Hydroxyapatite. Rare Metal Materials and Engineering. 2006;35(3):379.

[180] Tonsuaadu K, Gross KA, Plūduma L, Veiderma M. A review on the thermal stability of calcium apatites. Journal of thermal analysis and calorimetry. 2011;110(2):647–659.

[181] Gu Y, Khor K, Cheang P. Bone-like apatite layer formation on hydroxyapatite prepared by spark plasma sintering (SPS). Biomaterials. 2004;25(18):4127–4134.

[182] Muralithran G, Ramesh S. The effects of sintering temperature on the properties of hydroxyapatite. Ceramics International. 2000;26(2):221–230.

[183] German RM. Computer modeling of sintering processes. International Journal of Powder Metallurgy. 2002;38(2):48–66.

[184] Bose S, Saha SK. Synthesis and characterization of hydroxyapatite nanopowders by emulsion technique. Chemistry of materials. 2003;15(23):4464–4469.

[185] Gibson IR, Best SM, Bonfield W. Effect of silicon substitution on the sintering and microstructure of hydroxyapatite. Journal of the American Ceramic Society. 2002;85(11):2771–2777.

[186] Kim S, Lee J, Kim Y, Riu DH, Jung S, Lee Y, et al. Synthesis of Si, Mg substituted hydroxyapatites and their sintering behaviors. Biomaterials. 2003;24(8):1389–1398.

[187] Weast R. CRC handbook of chemistry and physics : a ready-reference book of chemical and physical data. Cleveland: CRC Press; 1974.

[188] Gasqueres G, Bonhomme C, Maquet J, Babonneau F, Hayakawa S, Kanaya T, et al. Revisiting silicate substituted hydroxyapatite by solid-state NMR. Magnetic Resonance in Chemistry. 2008;46(4):342–346.

[189] Gomes S, Renaudin G, Mesbah A, Jallot E, Bonhomme C, Babonneau F, et al. Thorough analysis of silicon substitution in biphasic calcium phosphate bioceramics: A multi-technique study. Acta Biomaterialia. 2010;6(8):3264–3274.

[190] Palard M, Champion E, Foucaud S. Synthesis of silicated hydroxyapatite Ca 10 (PO 4) 6- x (SiO 4) x (OH) 2- x. Journal of Solid State Chemistry. 2008;181(8):1950–1960.

[191] Gomes S, Nedelec JM, Jallot E, Sheptyakov D, Renaudin G. Silicon location in silicate-substituted calcium phosphate ceramics determined by neutron diffraction. Crystal growth & design. 2011;11(9):4017–4026.

[192] Ohgaki M, Kizuki T, Katsura M, Yamashita K. Manipulation of selective cell adhesion and growth by surface charges of electrically polarized hydroxyapatite. Journal of biomedical materials research. 2001;57(3):366–373.

[193] Zhou J, Zhang X, Chen J, Zeng S, De Groot K. High temperature characteristics of synthetic hydroxyapatite. Journal of materials science: materials in medicine. 1993;4(1):83–85.

[194] Rāutiu R, White D, Adeleye S, Adkins L. The use of zeta potential measurements in inorganic ion exchange studies. Hydrometallurgy. 1994;35(3):361–374.

[195] Gilman JW, VanderHart DL, Kashiwagi T. Thermal decomposition chemistry of poly (vinyl alcohol). ACS Sym Ser. 1994;599:161–185.

[196] Scalera F, Gervaso F, Sanosh K, Sannino A, Licciulli A. Influence of the calcination temperature on morphological and mechanical properties of highly porous hydroxyapatite scaffolds. Ceramics International. 2013;39(5):4839–4846.

[197] Munar ML, UDOH Ki, Ishikawa K, Matsuya S, Nakagawa M. Effects of sintering temperature over 1,300 C on the physical and compositional properties of porous hydroxyapatite foam. Dental materials journal. 2006;25(1):51–58.

[198] Pamula E, Bacakova L, Filova E, Buczynska J, Dobrzynski P, Noskova L, et al. The influence of pore size on colonization of poly (L-lactide-glycolide) scaffolds with human osteoblast-like MG 63 cells in vitro. Journal of Materials Science: Materials in Medicine. 2008;19(1):425–435.

[199] PAUTKE C, SCHIEKER M, TISCHER T, KOLK A, NETH P, MUTSCHLER W, et al. Characterization of osteosarcoma cell lines MG-63, Saos-2 and U-2 OS in comparison to human osteoblasts. Anticancer research. 2004;24(6):3743–3748.

[200] Bharadwaj S, Naidu A, Betageri G, Prasadarao N, Naidu A. Milk ribonuclease-enriched lactoferrin induces positive effects on bone turnover markers in postmenopausal women. Osteoporosis international. 2009;20(9):1603–1611.